RAMAN STUDIES OF THE NANOSTRUCTURE OF SOL-GEL MATERIALS

by

Calvin James Doss

Dissertation submitted to the Faculty of
the Virginia Polytechnic Institute and State University
in partial fulfillment of the requirements for the degree
of
DOCTOR OF PHILOSOPHY
in
PHYSICS

APPROVED:

Richard Zallen, Chairman

A. L. Ritter

J. R. Heflin

T. C. Ward

G. V. Gibbs

March, 1994

Blacksburg, Virginia

RAMAN STUDIES OF THE NANOSTRUCTURE OF SOL-GEL MATERIALS

by

Calvin James Doss

(Abstract)

Four sol-gel systems (alumina, aluminum hydroxide, zirconia, and magnesia) were investigated, primarily by laser spectroscopy, on several series of materials prepared by systematically varying the synthesis procedures. Key material phases analyzed were: (1) nanocrystalline boehmite [AlO(OH)]; (2) bayerite, nordstrandite, and gibbsite [$Al(OH)_3$ polymorphs]; (3) amorphous zirconia [a-ZrO_2]; and (4) magnesite [$MgCO_3$], hydromagnesite [$4MgCO_3 \cdot Mg(OH)_2 \cdot 5H_2O$], and magnesia [MgO]. Crystal nucleation and crystal growth kinetics were studied in several cases, with x-ray experiments carried out to calibrate the Raman-scattering technique I developed for monitoring crystallite size.

Nanocrystalline boehmite, γ-AlO(OH), was found to be the principal component in the sol-gel alumina system. Materials were prepared by the hot-water hydrolysis/condensation of $Al(OC_4H_9)_3$, the Yoldas process, as a function of process variables such as the time spent in the sol phase. Small but systematic changes, as a function of sol aging time, were discovered in the lineshape and position of the dominant boehmite Raman band observed in the alumina hydrogels. These spectral changes were interpreted in terms of nanocrystallinity-induced finite-size effects associated with the slow growth of AlO(OH) nanocrystals in the sol. X-ray diffraction experiments were used to determine nanocrystal sizes (as small as 3 nm for gels prepared from fresh sols) and to estimate growth kinetics from the Raman-lineshape results. These results appear to be among the first available for crystallite growth kinetics (ripening) in the near-atomic-scale

nanocrystal regime. The Raman peak-position shift is proportional to $L^{-\alpha}$, where L is the average nanocrystal size and α is a Raman-versus-size scaling exponent. For AlO(OH), I determined α to be 1.0, close to the scaling-exponent values reported for graphite and BN and different from the values (about 1.5) that describe the reported behavior of Si, Ge, and GaAs.

The trihydroxide polymorph system is closely related to the sol-gel alumina system. The processing temperature and the method of hydrolysis were varied, in order to determine their effect on the trihydroxide phase mix. The trihydroxide phase mix does not change with time; it depends only on the initial hydrolysis conditions. Bayerite is the primary phase present for materials processed at 25 C, while nordstrandite is the primary phase present for materials processed at 60 C. It is shown that the trihydroxide crystal nucleation kinetics are responsible for the $Al(OH)_3$ phase mix. Hydroxide/oxyhydroxide phase-mix kinetics were also studied; this ratio increases with time. The associated rate constant decreases with increasing temperature.

Sol-gel zirconia was prepared by using atmospheric water to hydrolyze a mixture of zirconium propoxide, acetic acid, and n-propanol. This produces a clear gel. Hydrogen peroxide was found to chemically react with the gels. Clean Raman spectra reveal a broad-band structure (the full width at half maximum is 150 cm^{-1}) centered at about 460 cm^{-1}. This band is interpreted as the signature of an amorphous phase of zirconia.

Raman and luminescent spectra (both obtained on the Raman spectrometer) were used to monitor the conversion of magnesium-carbonate-based materials to magnesium oxide, as a function of temperature. This new phase-determination technique utilizes the krypton 674.1 nm laser line so that the carbonate symmetric-stretch band and the $MgO:Cr^{+++}$ luminescence band are readily observable on the same spectrum.

Acknowledgments

I am grateful for the guidance and support of my advisor, Prof. Richard Zallen. I have enjoyed working with him.

I thank Philip Morris, USA for financially supporting a significant portion of my research. I sincerely appreciate the efforts of Dr. Cliff Lilly in this regard.

I would like to thank my dissertation committee members Prof. G. V. Gibbs, Prof. A. L. Ritter, Prof. J. R. Heflin, and Prof. T. C. Ward, for their enthusiasm and advice. I will always remember the late Prof. Diane Hoffman, an original committee member, for her humor and wit.

Outstanding technical support was provided for by Dale Schutt, Roger Link, and Grayson Wright, of the electronics shop, and Bob Ross, Melvin Shaver, and Dave Miller, of the machine shop.

I have enjoyed many interesting and suggestive conversations with my fellow graduate students Jeff Feng, Alf Siochi, Reinaldo Gonzalez, Scott Massie, Dan Korwan, Bing Shen, Charles Moller, Saikat Joardar ....

Chris Thomas and Prof. Clayton Williams have encouraged and supported me from the earliest parts of my graduate career.

This work is dedicated to my wife, Jaye Slater Doss,
and to my son, Nathan James Doss.

TABLE OF CONTENTS

CHAPTER ONE

INTRODUCTION

1.1 Introductory Remarks

Sol-gel technology is a method or process for making ultrafine-particle (nanometer to micron diameter) metal oxides (ceramics), in solution (sol) or gelatinous (gel) form. Primary concerns in this process are the control of the size, chemical, and structural composition of the ultrafine particles. In this dissertation, I have researched ways of characterizing sol-gel materials, primarily by Raman scattering, that address some of these concerns.

The processes used to make sol-gel materials are very complicated, and sol-gel solids comprise a very large class of ceramic materials. Classical sol-gel precursors, and the ones used in this dissertation, are liquids called metal alkoxides,[1] water, and sometimes additives such as acid. The transition from liquid precursors to particles in solution must traverse several important size and kinetic domains, for which a clear understanding is necessary for reproducibility. Besides the hope for novel and better materials, sol-gel technology strives for reproducibility, and this is the driving force behind much of the scientific investigation into these materials.

Sol-gel materials are scientifically interesting in their own right. Besides the unique structures that can be made with these materials, like xerogels and aerogels that have very high surface area densities and porosities,[2] the ultrafine particles can have unique properties simply by virtue of the sizes of the particles themselves.[3] Structural features, crystalline or amorphous,[4] are also of scientific

interest, as they give considerable insight into the earliest structural units in the processing of these materials.

Raman scattering was the primary analytical technique used here for studying the sol-gel materials. Advantages for its use are that it can characterize or identify molecular, amorphous, and crystalline materials, it can differentiate between crystal phases, and it also can reveal finite-size (nanocrystalline) effects. Also, the presence of water in these systems limits the capability of infrared techniques. Unfortunately, many of the Raman spectral features are not readily assigned without a complex calculation of vibrational modes and frequencies, in molecules or crystals. The key to successfully characterizing these complex materials is a systematic study. In this dissertation, time, temperature, acid type, and acid concentration, were systematically varied in order to understand their effects on the system, as well as the system itself.

The sol-gel materials studied in this dissertation are oxides (and, in some cases, hydroxides, peroxides, acetates, and carbonates) of aluminum, zirconium, and magnesium. The specific sol-gel procedures used to synthesize each of these three systems are described in detail in chapter two, with overall aspects briefly repeated in the later chapters on the individual systems (so that these chapters are reasonably self-contained).

1.2 Sol-Gel Chemistry

The sol-gel process involves two fundamental reactions, hydrolysis and condensation. The kinetics of these two reactions, and the molecular structures they produce, are the largest factors determining the nature of the final particulate solids. Therefore much of sol-gel technology and science either alters (in order to produce new or better materials), or seeks to understand, these two processes.

The hydrolysis and condensation reactions are schematically shown in Figure 1.1. The letters M and R stand for a metal cation (Al, Si, Zr, ...) and an alkyl group (methyl, ethyl, propyl, ...), respectively. The letters O and H represent oxygen and hydrogen, and the short lines indicate chemical bonds. The O-R combination is an alkoxy group, and the $M(OR)_4$ molecule is referred to as an alkoxide. The choice of fourfold coordination number here is arbitrary; the actual coordination depends on the metal. The hydrolysis reaction, in the upper half of the figure, proceeds by a nucleophilic addition-substitution reaction, in which alkoxy groups are replaced by hydroxide units supplied by the water. Alcohol is a byproduct of this reaction. The condensation reaction, shown in the lower half of the figure, occurs when two hydrolyzed units react to form an oxygen bridge.

The hydrolysis and condensation reactions are not necessarily sequential. That is, the condensation reaction may proceed without complete hydrolysis (all alkoxy groups replaced by hydroxyl groups). While a water-rich solution may follow the complete hydrolysis scheme outlined in Fig. 1.1, in a water-poor solution, condensation reactions may have to occur before further hydrolysis can take place. This is because the water may be completely consumed by the hydrolysis reaction, but it can then be re-supplied as a byproduct of the condensation reaction.

The rates of the hydrolysis and condensation reactions are not fixed. These rates can strongly depend on factors such as the alkoxy group, the degree of hydrolysis, the water:alkoxide ratio, and the presence of various additives and catalysts (especially those that can alter the pH). Also, the condensation reaction may proceed by additional mechanisms. For example, an unhydrolyzed molecule

with alkoxy groups may react with a completely hydrolyzed molecule with hydroxyl groups to form an oxygen bridge and alcohol.

The condensation process begins with monomers to form dimers. As it progresses, dimers may condense with monomers, other dimers, trimers, ... The product of the hydrolysis and condensation reactions are highly dispersed particles in solution, referred to as a colloidal suspension or a sol. Therefore, at some point, the net condensation of the system must stop, or else particle growth will reach a stage where a precipitate will form. Particles in solution are not as stable as a precipitate, because of their additional solid-liquid interfacial surface energy . Therefore, in order to prevent precipitation, a potential barrier must be set up between the particles.

Acid "peptization", or acid addition, is a means of producing a potential barrier between the colloidal particles. In this process, the particles are charged so that they repel each other. The charge can also bring about some additional surface passivation beyond the electrostatic effect.

Gelation occurs when the potential barrier between the particles is overcome. Depending on the system, several techniques may be used to accomplish this. Gelation may be induced by solvent boiloff (which increases the volume fraction occupied by the particles), changes in temperature and/or pH, or by the addition of an additive. If the potential barrier is not too large, gelation may proceed slowly over time.

1.3 Ostwald Ripening

Ostwald ripening, also referred to as coalescence, coarsening, or, simply, ripening,[5,6] is an aging phenomenon whereby larger particles grow at the expense of smaller particles. It occurs in systems that are composed of particles with

diameters less than about 10 nm. The driving force behind Ostwald ripening is the large surface energy of these systems, caused by their large surface area, that can be in the $500\,m^2 \cdot g^{-1}$ range.[7] Another way of looking at this phenomenon is to recognize that smaller particles have a higher solubility than larger particles. This produces a solute concentration gradient and therefore a transport of material from smaller particles to larger ones. The rate of solute transport is usually either diffusion or surface limited.

The Ostwald-Freundlich equation is given by

$$S = S_\infty \exp\left(\frac{2\gamma_{SL} V_m}{R_g T r}\right) \tag{1.1}$$

where S_∞ is the solubility (concentration), at the surface, of a particle of infinite radius (i.e. a flat plate), γ_{SL} is the solid-liquid surface energy density, V_m is the molar volume of the solid phase, R_g is the ideal gas constant, T is the temperature, and r is the radius of curvature of the object at the point of interest. This equation is not only applicable for solid particles with radius r, whose radius of curvature is r, but it also applies to holes of depressions that correspond to a negative radius of curvature, i.e. $r = -\|r\|$. Figure 1.2, which is a graphical representation of the Ostwald-Freundlich equation for the silica system, shows how the solubility, S, decreases as the particle size increases. This equation applies to equilibrium systems; for non-equilibrium systems, S is interpreted as the concentration of the solute at the surface of the particle.

1.4 Raman Scattering: The Finite-Size Effect

Raman scattering is an inelastic light-scattering process. Here we are concerned with the inelastic scattering of incident laser light by phonons (vibrations of the crystal lattice). In an infinite crystal, phonons are plane waves.

In a real crystal, the phonons are confined to a finite region of space, so that the standard plane-wave assumption becomes an approximation. For crystal dimensions down to 10^{-7} m (100 nm), this approximation remains a superb one; deviations from its predictions are difficult to discern. In the work described in this dissertation, we encounter crystal sizes well below 100 nm, down to dimensions as small as 3 nm (for AlO(OH), described in chapter three). For these "nanocrystal" dimensions, deviations from the infinite-crystal plane-wave-approximation predictions become quite significant. (A "nanocrystal" is a crystallite having dimensions of a few nanometers.) For example, as discussed below, the $q = 0$ optical selection rule breaks down in nanocrystals. For Raman scattering, these "finite-size effects" (also known as "phonon-confinement effects") are well treated by a theoretical model developed by Richter, Wang, and Ley.[8] In their theory, each nanocrystal (which typically contains a few thousand unit cells) is assumed to be identical in structure with a piece of the infinite crystal. The phonon dispersion curve is assumed to be the same as in the infinite crystal. The finite size of the nanocrystal is introduced by an envelope function modifying the phonon wavefunction.

In the theory of the finite-size effect proposed by Richter et. al., the phonon wavefunction is modified in the following way. Let $\psi_\infty(q_o, r)$ be the wavefunction of the infinite crystal (i.e., a plane wave), with wavevector q_o and position r. Then the phonon wavefunction of a nanocrystal is written as

$$\psi_n(q_o, r) = C(r, r_o, l)\psi_\infty(q_o, r), \tag{1.2}$$

where

$$C(r, r_o, l) \propto \exp\left(-2|r - r_o|^2 / l^2\right) \tag{1.3}$$

is a Gaussian confinement function, centered at r_o and with a width (two times the standard deviation of the Gaussian) of l . In the model, l and r_o correspond to the diameter and center of the nanocrystal respectively.

Let $\phi_n(q,q_o)$ be the Fourier transform of $\psi_n(q_o,r)$, i.e., the momentum space representation of the phonon, $\psi_n(q_o,r)$. This gives

$$\phi_n(q,q_o) \propto l \cdot \exp\left(-l^2|q-q_o|^2/8\right), \tag{1.4}$$

which is a Gaussian, centered at q_o and with a width of $4/l$. Therefore, the smaller is the crystal size in real space, the larger is the spread of the phonon wavefunction in momentum space.

Equations (1.3) and (1.4), taken together, can be seen to constitute a statement of the Heisenberg uncertainty principle in the following way. Equation (1.3) gives $\Delta x = l/\sqrt{8}$, and eqn. (1.4) gives $\Delta p = \hbar\sqrt{2}/l$ (since $\Delta p = \hbar\Delta q$, and $\Delta q = \sqrt{2}/l$). Therefore,

$$\Delta x \Delta p = \frac{l}{\sqrt{8}} \cdot \frac{\hbar\sqrt{2}}{l} = \frac{\hbar}{2}.$$ (Heisenberg uncertainty relation for Gaussians, the optimum wavefunction shape)

The most important relationship that we need to recognize is that

$$\Delta q \propto \frac{1}{l}, \tag{1.5}$$

where l is the crystal size. This result, and its effect on the Raman spectrum, is a consequence of the Heisenberg uncertainty principle.

Figure 1.3 is a schematic of how eqn. (1.5) effects the Raman spectrum. In the righthand side of the figure is a phonon dispersion curve, which plots phonon frequency (energy) versus wavevector (crystal momentum). The solid black dots represent specific phonon modes of the bulk crystal. In a bulk crystal, only

phonon modes at $q = 0$ are Raman allowed because of the wavevector selection rule (which is a consequence of crystal momentum conservation). The Raman signal of the bulk crystal is shown on the graph at the lefthand side of the figure. On this graph, the Raman signal is plotted horizontally, increasing to the left, and frequency is plotted vertically, increasing towards the top of the page. The Raman signal shows up as a sharp peak because only one mode (the mode at zone center), and hence only one frequency, is allowed to interact with the incident laser light, as a consequence of the wavevector selection rule.

The wavevector selection rule for a nanocrystal is relaxed, in the following way. In a bulk crystal, the horizontal width (in wavevector) of each black dot (on the righthand side of Fig. 1.3) is infinitesimally small. In a nanocrystal, each black dot acquires a width which, according to eqn. (1.5), is proportional to $1/l$. Therefore, phonon modes not $q = 0$ (the center of the Brillouin zone) have zone-center character. The result is that modes that are within $\Delta q = \frac{1}{l}$ of the zone center become Raman active.

The phonon dispersion curve in Fig. 1.3 shows the range $(0 \le q \le \Delta q)$ of Raman-active modes for a nanocrystal of size l. These modes span a range of frequencies. All of these frequencies show up in the Raman spectrum, producing the asymmetrically broadened Raman band at the left side of the figure. The broad band exhibited by the nanocrystal is also downshifted from the sharp line exhibited by the bulk crystal, as a consequence of the downward curvature of the phonon dispersion curve, and the increasing density of phonon modes with wavevector in three dimensional systems.

The frequency dependence of the Raman scattering intensity for nanocrystals, as given by this theory, is obtained by integrating over wavevector space:

$$\int \exp\left(-q^2 l^2 / 4\right) \frac{d^3 q}{\left[\omega - \omega(q)\right]^2 + \left[\Gamma_0 / 4\right]^2} \quad . \tag{1.6}$$

Here Γ_o is the full-width-at-half-maximum (FWHM) of the bulk crystal Raman band, and $\omega(q)$ is the phonon dispersion relation. In a bulk crystal, the exponential is replaced by $\delta(q)$.

By examining the Raman band lineshape parameters (peak position, full-width-at-half-maximum, and asymmetry), the nanocrystal size may be determined with the use of eqn. (1.6). Unfortunately, the phonon dispersion curve, $\omega(q)$,is unknown for most crystals. The phonon dispersion curve is known for the well-understood semiconductor crystals Si, Ge, and GaAs, and for these materials, the theory agrees very well with the experimental results.[9,10,11]

1.5 Dissertation Outline

Chapter two is detail oriented. Here specifics of the materials synthesis procedures are covered. In addition, aspects of the Raman spectroscopy are clarified. This chapter is not a prerequisite for reading the rest of the chapters in the dissertation. It is primarily intended to be helpful to researchers desiring to reproduce some of these results.

Chapter three presents the results of a systematic Raman scattering and x-ray diffraction investigation of sol-gel alumina, for a wide range of synthesis conditions. Nanocrystalline boehmite, γ-AlO(OH), is the principal component of these materials. Clear finite-size effects have been observed, and these have been

used to establish a method of monitoring the nanocrystal growth kinetics in the sol phase. The results contained in this chapter have been published as an article in the Physical Review.[12]

Chapter four shows the effects of altering the synthesis procedures of chapter three to a regime in which gels do not form. Three distinct aluminum hydoxide, $Al(OH)_3$, phases are formed when an acid peptization step is eliminated and the processing temperature is lowered. Structure and kinetics of the aluminum hydroxide phases are analyzed.

Chapter five contains the results on two separate sol-gel materials systems. In the first system, an amorphous form of zirconia (ZrO_2) is produced and characterized. In the second system, the conversion of magnesite and hydromagnesite to magnesia (MgO) is monitored as a function of temperature; this is done by using Raman and luminescent signatures of these materials.

Chapter six briefly summarizes the results and provides suggestions for further study.

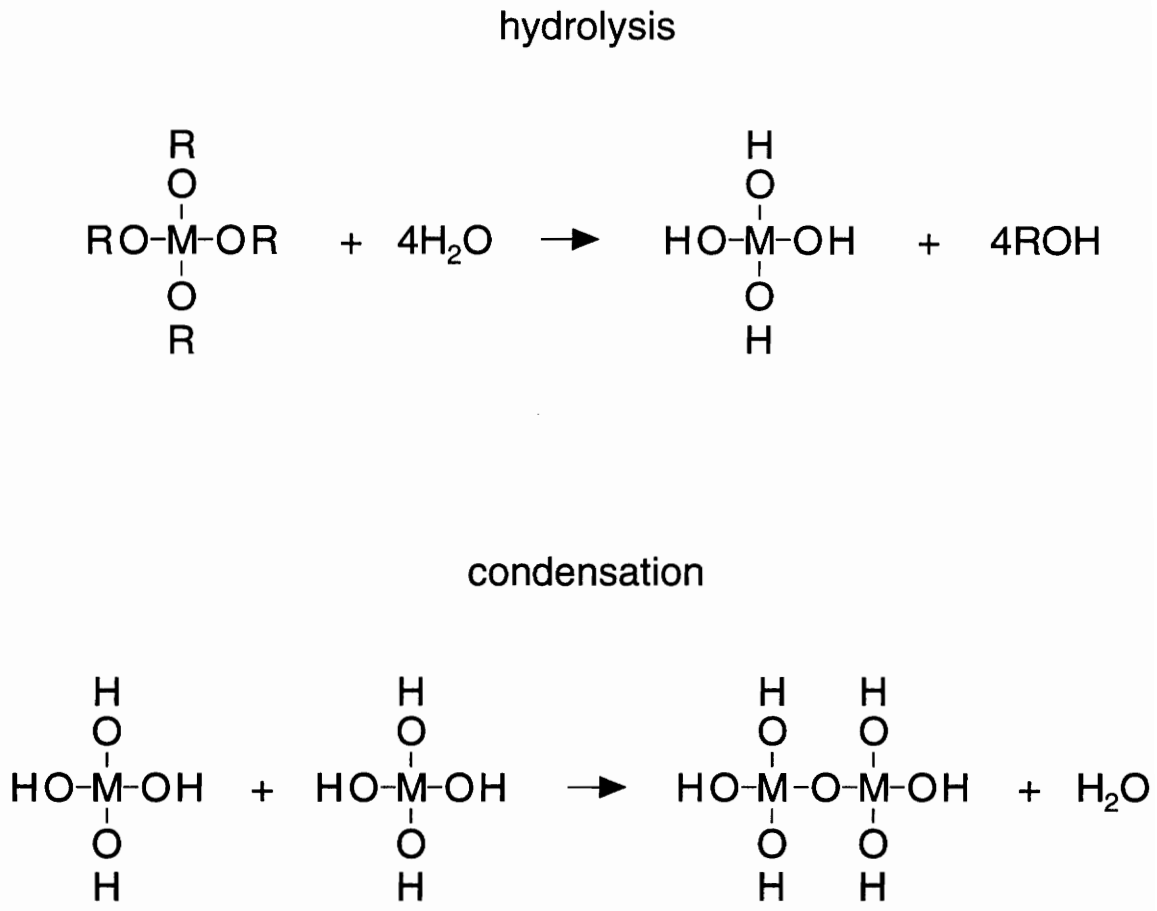

Fig. 1.1: The chemistry of sol-gel materials synthesis consists of two fundamental reactions, hydrolysis and condensation. Here, M, O, and R represent a metal atom (Si, Al, Zr, ...), an oxygen atom, and an alkyl group (methyl, ethyl, propyl, ... group), respectively. The $M(OR)_4$ unit shown at the top of the figure is a metal alkoxide molecule. Hydrolysis of metal alkoxides produce metal hydroxides. Condensation of the metal hydroxides produce metal hydroxide oligomers (here shown as the product of the condensation reaction), and eventually metal oxides.

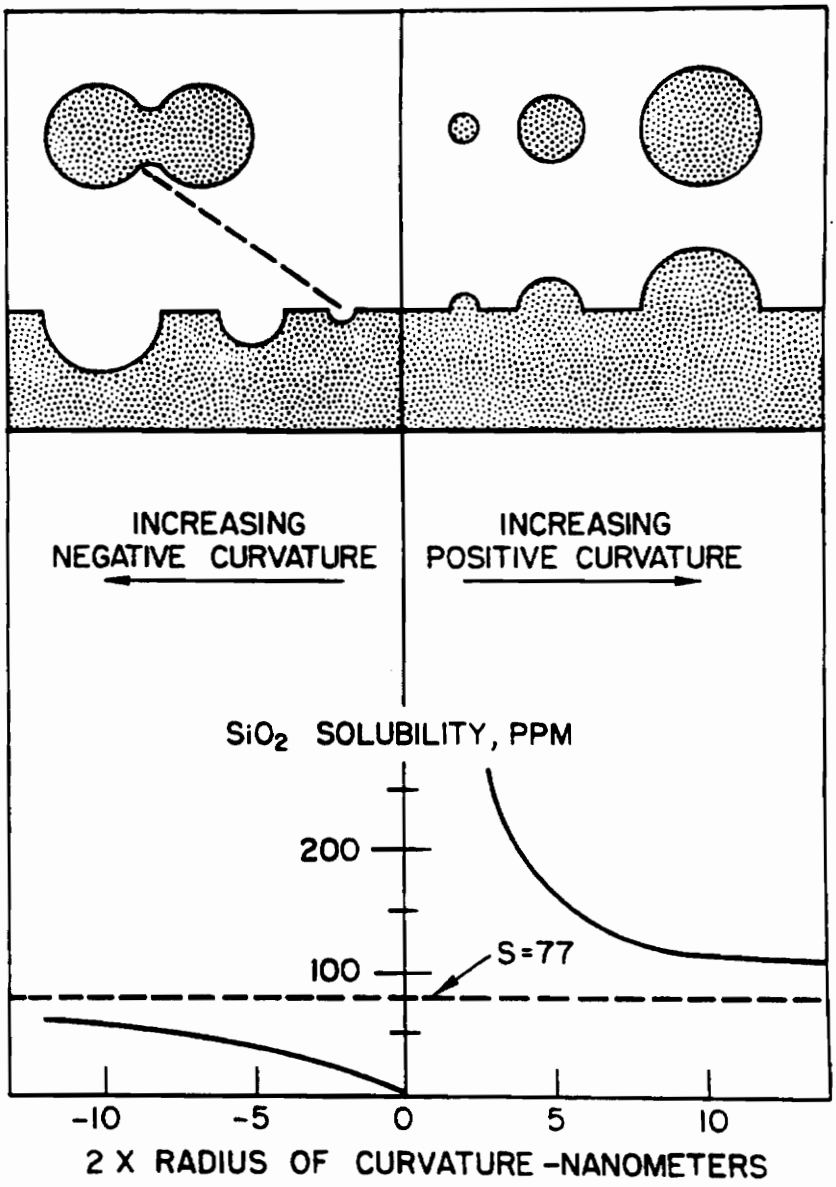

Fig. 1.2: The solubility of silica particles/depressions as a function of their radius of curvature. Particles and projections on surfaces have positive curvature. Surface depressions have negative curvature. From R. K. Iler.[13]

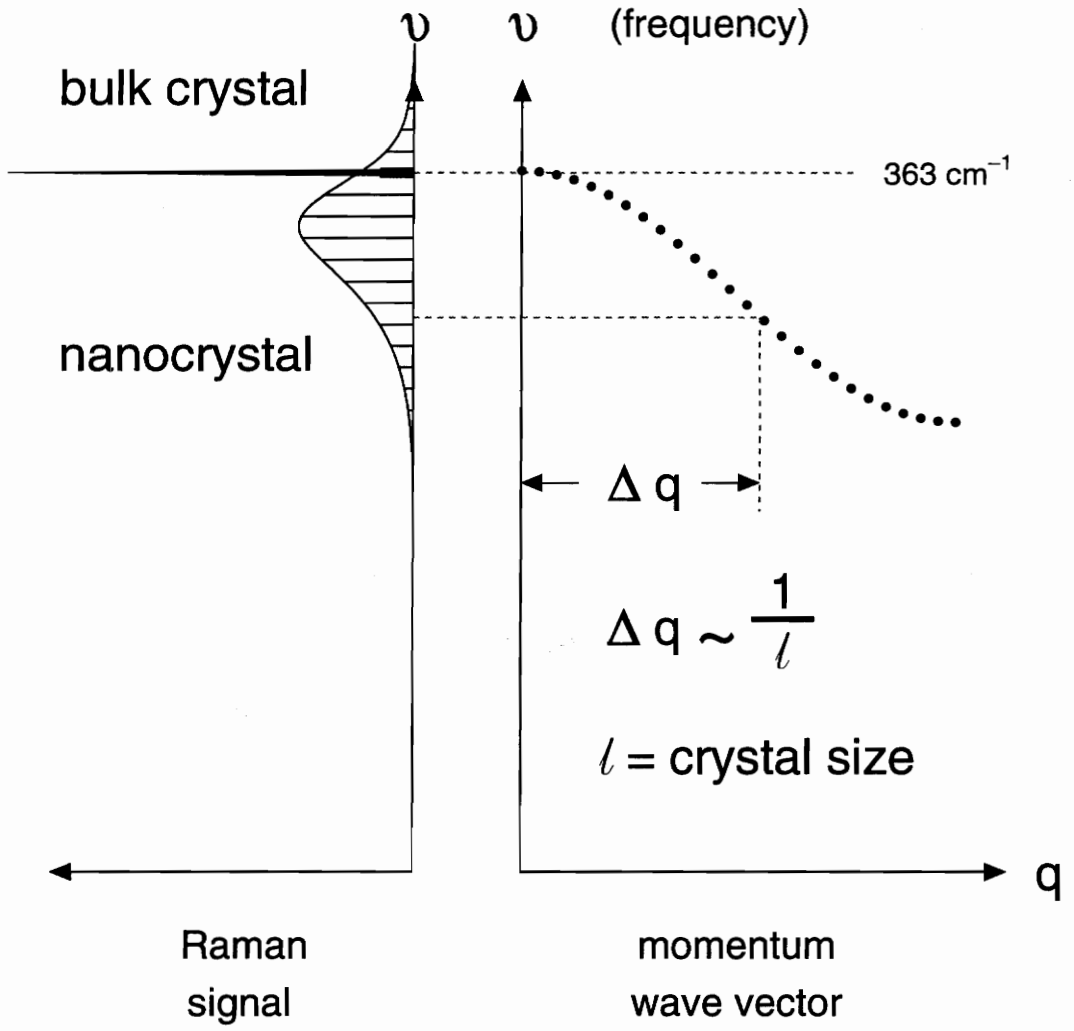

Fig. 1.3: Schematic of how phonon confinement effects the Raman spectrum. The righthand side of the figure is a phonon dispersion curve. The solid black dots represent specific phonon modes of the bulk crystal. The Raman signal of the bulk crystal is shown at the left. Here, the Raman signal is plotted horizontally, increasing to the left, and frequency is plotted vertically, increasing towards the top of the page. In a bulk crystal, the horizontal width (in wavevector) of each black dot is infinitesimally small. In a nanocrystal, each black dot acquires a width which, according to eqn. (1.5), is proportional to $1/l$. Therefore, phonon modes not $q = 0$ (the center of the Brillouin zone) have zone-center character. The result is that modes that are within $\Delta q = 1/l$ of the zone center become Raman active, which leads to the nanocrystal Raman spectrum shown.

[1]D. C. Bradley, R. C. Mehrotra, and D. P. Gaur, Metal Alkoxides (Academic Press, New York, 1978).

[2]L. C. Klein, Sol-Gel Technology for Thin Films, Fibers, Preforms, Electronics and Specialty Shapes, edited by L. C. Klein (Noyes Publications, New Jersey, 1988), p. 382.

[3]J. Jortner, Physics and Chemistry of Finite Systems: From Clusters to Crystals, edited by P. Jenna, S. N. Khanna, and B. K. Rao (Kluwer, Dordrecht, 1992), p. 1.

[4]R. Zallen, The Physics of Amorphous Solids (John Wiley & Sons, New York, 1983).

[5]I. M. Lifshitz and V. V. Slyozov, J. Phys. Chem. Solids, **19**, 35 (1959).

[6]C. Wagner, Z. Elektrochem., **65**, 581 (1961).

[7]T. Lombardi and L. C. Klein, Adv. Ceram Mat. **3,** 167 (1988).

[8]H. Richter, Z. P. Wang, and L. Ley, Solid State Commun. **39**, 625 (1981).

[9]H. Richter, Z. P. Wang, and L. Ley, Solid State Commun. **39**, 625 (1981).

[10]T. Kanata, H. Murai, and K. Kubota, J. Appl. Phys. **61**, 969 (1987).

[11]K. K. Tiong, P. M. Amirtharaj, F. H. Pollak, and D. E. Aspnes, Appl. Phys. Lett. **44**, 122 (1984).

[12]C. J. Doss and R. Zallen, Phys. Rev. B **48**, 15626 (1993).

[13]R. K. Iler, The Chemistry of Silica (Wiley, New York, 1979) p. 50.

CHAPTER TWO

EXPERIMENTAL: MATERIALS AND METHODS

2.1 Introduction

The details of the materials synthesis and the methods of analysis are discussed in this chapter. It is not necessary to read this chapter in order to understand the following chapters. However, this chapter should prove helpful to anyone interested in reproducing any of these experiments, or anyone attempting to carry out similar experiments. Section 2.2 details the process for making "sol-gel alumina", and the related materials that will be analyzed in chapter 3. Section 2.3 details the process for synthesizing the materials of chapter 4; these are referred to as the "$Al(OH)_3$ materials", since various $Al(OH)_3$ crystalline polymorphs are produced in this process. Section 2.4 describes the synthesis procedure for making the "sol-gel zirconia" materials of chapter 5; and section 2.5 describes the magnesium carbonate materials, also of chapter 5. Finally, section 2.6 discusses some of the experimental methods used to obtain the Raman spectra of the synthesized materials.

2.2 Synthesis of Sol-Gel Alumina and Related Materials

The Yoldas process for making clear alumina gels, as indicated in Fig. 2.1, consists of three main steps:

(i) hydrolysis and condensation of an aluminum alkoxide to form an AlO(OH) precipitate;

(ii) re-suspension and dissolution of the precipitate by acid peptization to form a clear, colloidal, sol;

(iii) concentration of the sol by solvent boiloff, resulting in the formation of a gel.

Specific details follow:

(1) Aluminum secondary butoxide (ASB), $Al(OC_4H_9)_3$, was doubly distilled and stored in an inert-atmosphere chamber. ASB is a clear viscous liquid at room temperature, although undistilled commercial sources usually have a yellow tint, which is a sign of impurities. A portion of the ASB (typically 25 g, or about 0.1 mole) was heated, to reduce its viscosity, and drawn into a syringe via a 12 gauge needle. Water (typically 200 ml, or about 11 moles) was added to the reaction vessel and maintained at 80 C, the initial hydrolysis temperature. The H_2O:ASB molar ratio was kept at 110:1. A temperature controller was used to sustain the appropriate processing temperature in all phases of the materials making process, to within about ± 2 C.

(2) A continuous stream of ASB was added, via the 12 gauge syringe, to the 80 C water, under vigorous stirring conditions. This step induces immediate hydrolysis and condensation reactions, and yields an AlO(OH) precipitate in the water. From now on I will refer to the contents of the reaction vessel as the sol. This completes step (i) of the Yoldas process.

(3) Immediately following step 2, the temperature controller was set to 95 C, and was not changed from this setting for the remainder of the materials-making process. The initial hydrolysis and condensation reactions raised the sol temperature a few degrees due to their exothermic nature. An initial hydrolysis temperature of 80 C, versus 95 C, was used because the boiling was too violent with an initial water temperature of 95 C (Yoldas typically used initial water temperatures of 75 C). It took about 20 minutes for the sol to reach 95 C; this was

partially due to the fact that the sol boiled off secondary butanol (a by-product of the hydrolysis reaction) as the temperature was increased. The reaction vessel was open to the atmosphere during this time.

(4) Twenty minutes after the initial hydrolysis and condensation step, a 0.1 normal inorganic acid (HCl or HNO_3) was added to the reaction vessel, with two different molar ratios [acid:ASB molar ratios (R) of 7:100 or 14:100, which will be referred to as by R=0.07 or R=0.14 respectively]. Peptization serves to disperse the AlO(OH) precipitate and send it into solution in the form of a clear, stable, colloidal, sol. The rate at which the sol is peptized or dispersed depends upon the acid:ASB molar ratio R, although many other factors may also be important. Generally, the higher the acid concentration, the faster the peptization or dispersion of the precipitate. The peptization or dispersion process can take several hours or several days. The acid-addition peptization step was carried out 20 minutes after the initial hydrolysis step; this particular timing (which was not varied) stems from Yoldas' early work on this system. He observed that the later sols peptized or dispersed faster if peptization occurred twenty minutes after the initial hydrolysis, versus immediate peptization. Step (ii) of the Yoldas process is now complete, with the understanding that the sols are not completely peptized, or dispersed into a clear colloidal sol, until later processing times.

(5) Immediately following the peptization step, the reaction vessel was sealed (except for a small hole made by a syringe needle) to prevent water evaporation. The sol remains in this state (stirring, sealed, 95 C) for the rest of the materials making process.

(6) At selected time intervals, a sample of the sol was removed from the reaction vessel. This sample was then boiled (for about 10 minutes) in a small

open beaker to remove excess water and concentrate the sol. Upon sufficient removal of water, about 50% of the initial solution, the sol becomes quite viscous and nears the gel point. The viscous sol was then transferred to a 1 dram glass vial and sealed to prevent further solvent removal. The viscous sol was then allowed to cool to room temperature, where gelation took place. The time it took, for the sol to gel, depended largely on how much solvent had been removed in the initial concentration step. In most cases it took place in less than a minute (experimentally the gel point is difficult to define). Cooling the viscous sol appears to increase the rate of gelation. The final products are the room-temperature gels. About six gel samples are produced from each reaction vessel. This completes step (iii) in the Yoldas procedure. These gels are also referred to as hydrogels, because they are approximately 90% water by weight. The early gels (gels made from sols that were processed in the sol phase for only a few hours) are cloudy; later gels become progressively clearer (with increasing time spent in the sol phase). At room temperature, cloudy gels remain cloudy, i.e., peptization stops. Furthermore, microcrystalline boehmite (the dominant solid phase) ceases its crystallite growth. Gel structure thus remains stable at room temperature. The gels will be referred to by the acid type and concentration used in peptization and, especially, by the length of time spent in the earlier sol phase [e.g., HNO_3, R=.07, 24 hours, hydrogel].

The procedure for making the unpeptized boehmite precipitates is similar to the procedure for making the hydrogels, with the differences indicated below (according to the step-by-step numbering system used for the hydrogels). The first three steps are the same.

(4) The sol was never peptized. Therefore the sols remain as aqueous

precipitates, and never form gels.

(6) At selected time intervals, a sample of the sol was removed from the reaction vessel. The sol was then centrifuged to separate the majority of the water from the precipitate. About 75% of the water was removed in this step. The product (a white mush) was then transferred to an oven and dried at 110 C for at least 24 hours. The precipitate is almost completely dry after about 2 hours in the oven. During this time, the microcrystalline boehmite may still be growing (this is very likely although not monitored). Once the material is dry, microcrystalline boehmite stops growing. The results of these steps are hard, opaque, white chunks. We shall refer to these samples as dried precipitates.

In addition to the hydrogels and the precipitates, a few other samples were investigated. Portions of some of the hydrogels were subjected to a 110 C oven drying step (like that used for the precipitates), removing their water content and yielding xerogels in the form of transparent chunks. An unpeptized precipitate (referred to as a 130 C precipitate) powder sample was made by adding ASB to H_2O (ASB:H_2O was 110) and processing the sol in a pressure vessel at 130 C for about five days. The sol was then dried in an oven at 110 C. The product of this process was a white powder. A sample of crystalline boehmite powder (composed of micron-size crystals), prepared by autoclaving aluminum metal in excess water, was provided by Alcoa laboratories. X-ray diffraction confirmed that the material was well-crystallized boehmite.

2.3 Synthesis of the $Al(OH)_3$ Materials

The $Al(OH)_3$ materials were made by a process similar to that used for the alumina precipitates (section 2.2), with key differences relating to the processing temperature and the method of hydrolysis. The results of chapter 4 show that these

differences have striking consequences.

Figure 2.2 is a schematic of the procedure. Doubly distilled aluminum secondary butoxide (ASB) was mixed with water, with an ASB:H_2O molar ratio of 110. Three different processing temperatures (25, 40, and 60 C) were used to yield an $AlO(OH)\cdot xH_20$ precipitate. Initial water temperatures were approximately five degrees lower than the indicated temperature, to compensate for the exothermic nature of the hydrolysis reaction. Shortly after the initial hydrolysis reaction, the reaction vessel was closed off, except for a hole produced by a small syringe needle. The sols, or aqueous precipitates, were aged for up to 17 days. At selected time intervals, samples were obtained from the reaction vessel. The sample was then centrifuged to separate the majority of the water from the precipitate. About 75% of the water was removed in this step, which produces a white mush. The mush was then transferred to an oven and dried at 110 C for at least 24 hours. The wet mush is dry after about 2 hours in the oven. Once the material is dry, all crystal growth stops. The results of these steps are hard white chunks.

Two methods of hydrolysis were used. The first method utilized a 12 gauge syringe needle to inject a steady stream of ASB into the water of the reaction vessel. The second method first placed the ASB into the reaction vessel, by a distillation procedure. Water was then added to the reaction vessel from a beaker.

2.4 Preparation of the Zirconia Materials

Zirconia gels were prepared by the following method. Zirconium n-propoxide, as $Zr(OC_3H_7)_4 \cdot 2.8C_3H_7OH$ (stoichiometry as received from manufacturer), a liquid at room temperature, was mixed with a larger quantity of n-propanol, C_3H_7OH. The recipe was 10 ml of zirconium n-propoxide mixed

with 100 ml of n-propanol. To this mixture was added approximately 1 ml of glacial acetic acid. The reaction vessel was then covered with aluminum foil perforated with several small holes; the purpose of the small holes in the foil was to allow atmospheric water to slowly hydrolyze the sol. A gel formed on the order of days. If, however, there were no holes in the aluminum foil, gelation did not occur. The relative humidity of the room air is therefore an important parameter. Various zirconia materials, based upon this method of preparation, are discussed in the text.

2.5 The Magnesium Carbonate Materials.

The magnesite, hydromagnesite, and magnesia samples were obtained from commercial sources. Magnesite is $MgCO_3$, hydromagnesite is $4MgCO_3 \cdot Mg(OH)_2 \cdot 5H_2O$, and magnesia is MgO. Heat treatments were carried out in the following way. Samples were placed in a furnace (Lindberg box furnace model 51542, with a Platinel II thermocouple and model 59344 control console) and ramped to the "treatment temperature" at a rate of 5 C per minute. They remained at the treatment temperature for two hours before being ramped back down to room temperature.

2.6 Raman Scattering Measurements

Raman spectra (Stokes spectra) were obtained at room temperature, using a SPEX 1403 Raman spectrometer, with a GaAs photomultiplier and photon-counting electronics. A CW argon ion laser operating at 488.0 nm or 514.5 nm, and a CW krypton ion laser operating at 647.1 nm or 676.4 nm were the excitation sources. We used an instrumental bandwidth of 4.0 cm^{-1} and a 2.0 cm^{-1} step size, unless otherwise indicated. Spectra were obtained in the 90° scattering configuration, collecting both polarizations of scattered light.

2.6.1 Bandwidth and temperature effects on the Raman spectrometer

The main features of the Raman spectrometer are described by Holtz.[1] This section will elaborate on a few experimental details of the Raman spectrometer that will hopefully give some perspective on commonly misunderstood (instrumental bandwidth) or poorly documented (temperature) effects. First, a brief introduction to the Raman spectrometer.

Figure 2.3 is a schematic of the Raman-scattering experiment. A monochromatic beam of laser light , with incident frequency $\overline{\nu}_i$ ($\overline{\nu}_i$ is defined as λ_i^{-1}, where λ_i is the wavelength of the incident light, and is the frequency expressed in wavenumber units), is focused on the sample. Inelastically scattered light from the sample is collected by a series of optics and sent into the Raman spectrometer, which is a double grating monochromator, via slit S_1. The gratings G_1 and G_2, in conjunction with slits S_1, S_2, S_3, and S_4, allow one frequency to pass through the spectrometer, and to the photomultiplier tube (PMT). The PMT measures the selected light intensity. The gratings are rotated in tandem to select, one frequency at a time, a whole spectrum of frequencies. The output, a "Raman spectrum", is a plot of frequency versus intensity.

The poorly understood concept of instrumental bandwidth will now be discussed. For the time being, think of the Raman spectrometer as a black box. The input to the Raman spectrometer is an intensity spectrum, call it $I_o(\overline{\nu})$. The question is, what is actually measured or observed by the spectrometer? Ideally the measured spectrum, lets call it $I_m(\overline{\nu})$, would equal the incident spectrum $I_o(\overline{\nu})$. The instrumental interaction with the incident intensity spectrum however produces a significant perturbation which can be quantitatively described in the

[1]M. Holtz, Ph.D. Dissertation, Virginia Tech, (1987).

following way: $$I_m(\bar{\nu}) = \int_{-\infty}^{+\infty} T(\bar{\nu}-\xi) I_o(\xi) d\xi, \qquad (2.1)$$

where T is the instrumental transfer function in the convolution integral.

Suppose $$T(\xi - \bar{\nu}) = \delta(\xi - \bar{\nu}), \qquad (2.2)$$

then $$I_m(\bar{\nu}) = I_o(\bar{\nu}),$$

which is the desired result. But a delta-function transfer function is experimentally impossible to obtain [it would correspond to slit widths S_1 and S_4 being zero (Fig. 2.3) and will be discussed further in a moment]. Now suppose that

$$I_o(\xi) = \delta(\xi), \qquad (2.3)$$

then $$I_m(\bar{\nu}) = T(\bar{\nu}).$$

Therefore, if we could find a source that is monochromatic, then we would be able to experimentally measure the transfer function T. Of course, a laser source works well for this purpose. Ion gas laser sources have a Gaussian frequency spread (fwhm) of 10 gigahertz, or about $0.3\ \mathrm{cm}^{-1}$. This is small compared to the instrumental spectral slit widths or actual phonon features, which are both usually $3.0\ \mathrm{cm}^{-1}$ or larger.

Figure 2.4 shows a "Raman" intensity profile obtained by scanning over the laser line. That is, this is an experimental determination of the transfer function T of eqn. (2.3). The black dots are the actual data points and the solid curve is a Gaussian fit to the dots. The laser peak position should reside at $0.0\ \mathrm{cm}^{-1}$. Here it is located at $0.6\ \mathrm{cm}^{-1}$, because of a systematic offset of the gratings. The Gaussian curve (solid line) is a reasonable parameterization of the transfer

function, although a simple triangle function would also fit well in this case. The crucial instrumental quantity, the instrumental bandwidth, is defined as the full width at half maximum (fwhm) of the transfer function T.

A method of estimating the actual linewidth (fwhm) of an observed phonon band in the Raman spectrum, taking into account the additional broadening caused by the instrumental bandwidth, is as follows. Knowing the instrumental bandwidth (B) and the fwhm of the measured intensity profile $I_m(\overline{\nu})$ (fwhm_{obs}), we may infer the fwhm of the actual (true) intensity profile $I_o(\overline{\nu})$ ($\text{fwhm}_{\text{actual}}$), by the following logic. Assume that the transfer function and the true incident intensity profile are both Gaussian. This is justified for the transfer function by the previous paragraph and Fig. 2.4. A Gaussian profile for the $I_o(\overline{\nu})$ is not a bad assumption in many cases either, although in most theoretical descriptions it is lorentzian. If T and $I_o(\overline{\nu})$ are both Gaussians, then the convolution integral of eqn. (2.1) will also yield a Gaussian profile. The relationship between the fwhm of the three Gaussian profiles, using the notation of this paragraph, is as follows.

$$(\text{fwhm}_{\text{obs}})^2=(\text{fwhm}_{\text{actual}})^2+B^2. \qquad (2.4)$$

Equation 2.4 is used extensively in chapter 3. More refined (and much more complicated) deconvolution procedures exist, but they almost always yield results indistinguishable from those obtained with (2.4).

Temperature has a very strong effect on the alignment, calibration, and coordination of the gratings of the Raman spectrometer. Referring back to the schematic of the Raman spectrometer (Fig. 2.3), the gratings G_1 and G_2 rotate as a function of temperature, and this can produce unwanted peak shifting and broadening in the Raman spectrum. In order to understand this effect, a way of determining the position of each grating is needed. This is accomplished for

grating G_1 in the following way: (1) first set the slit widths of S_1 and S_2 to be 10 μ and the slit widths of S_3 and S_4 to be 500 μ; (2) scan over the laser line and compare the known laser peak position with the grating counter. The position for grating G_2 can be determined in a similar manner, by interchanging the slit-width settings.

Figure 2.5 is a plot of the grating positions versus temperature and shows a very significant effect. The positions are recorded with respect to the expected laser peak position. Notice that not only are the grating calibrations changing with temperature, but they are also changing with respect to each other. The laboratory temperature is now controlled to within ± 1.0 C.

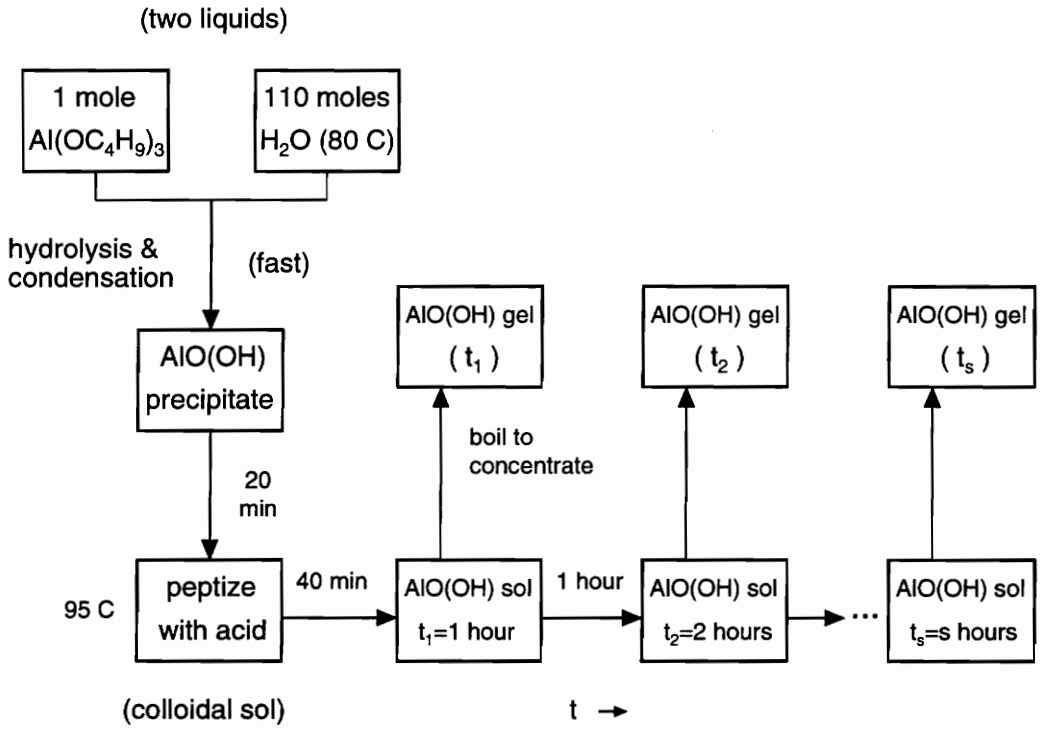

Fig. 2.1: Schematic of our implementation of the Yoldas process for synthesizing sol-gel alumina. After time t_S in the sol phase at 95 C, gelation was brought on by boiloff-induced concentration. Raman studies were done on hydrogels prepared using various sol aging times (t_S), and the effect of varying the acid peptization step in the synthesis was also studied.

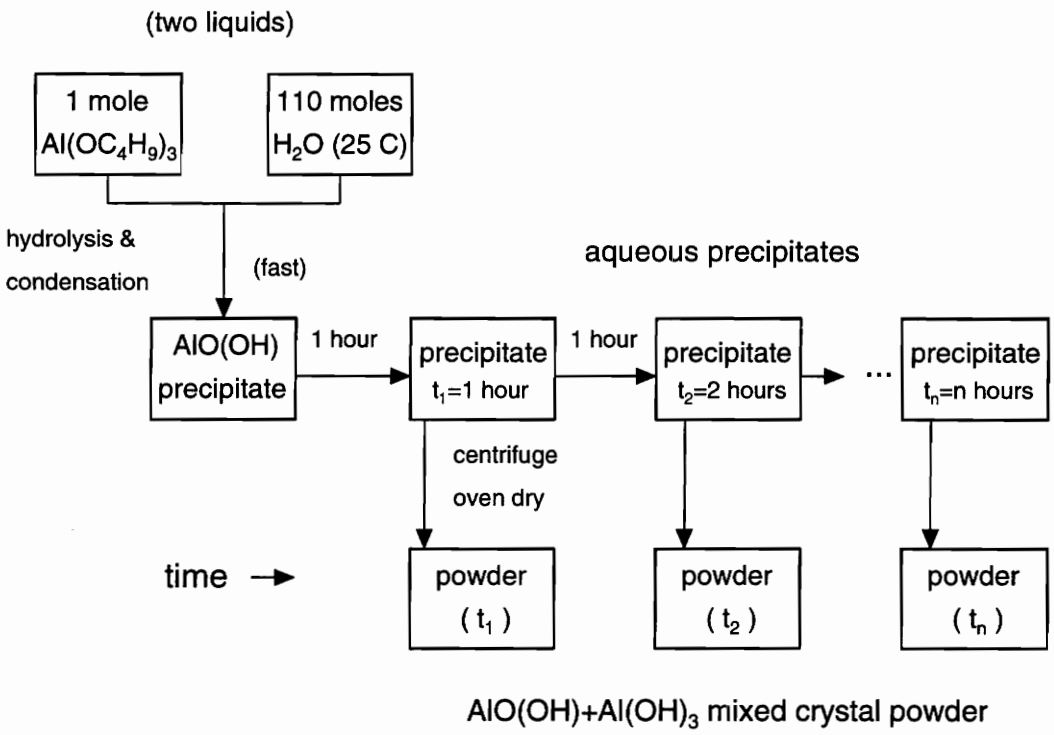

Fig. 2.2: Schematic of the materials synthesis procedure. Aluminum sec-butoxide is hydrolyzed to produce an aqueous precipitate, with an AlO(OH) stoichiometry. The solution is allowed to age. At selected time intervals, a sample is removed from the reaction vessel, centrifuged, and oven dried (110 C). Raman, infrared, and x-ray studies were done on solids prepared by using various, aging times (t_n), temperatures (25, 40, and 60 C), and hydrolysis methods.

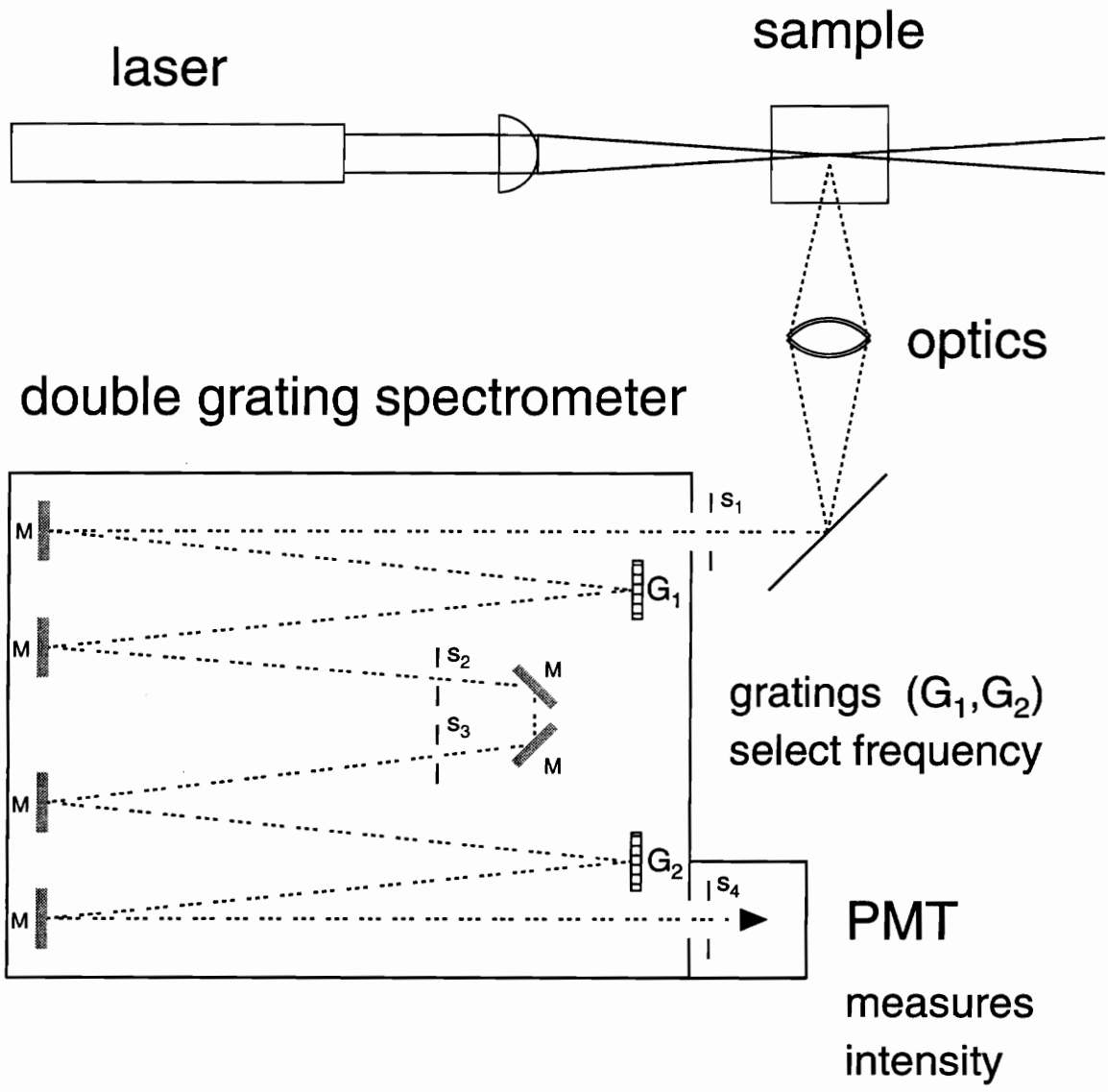

Fig. 2.3 Schematic of a Raman spectrometer, a double grating monochromator. A monochromatic beam of laser light, with incident frequency $\bar{\nu}_i$ ($\bar{\nu}_i$ is equal to λ_i^{-1}, where λ_i is the wavelength of the incident light), is focused on the sample. Inelastically scattered light from the sample is collected by a series of optics, and sent into the Raman spectrometer via slit S_1. The gratings G_1 and G_2, in conjunction with the slits S_1, S_2, S_3, and S_4, allow one frequency to pass through the spectrometer, and to the photomultiplier tube (PMT). The PMT measures the selected light intensity. The gratings are rotated in tandem to select, one frequency at a time, a whole spectrum of frequencies. The output, a "Raman spectrum", is a plot of frequency versus intensity.

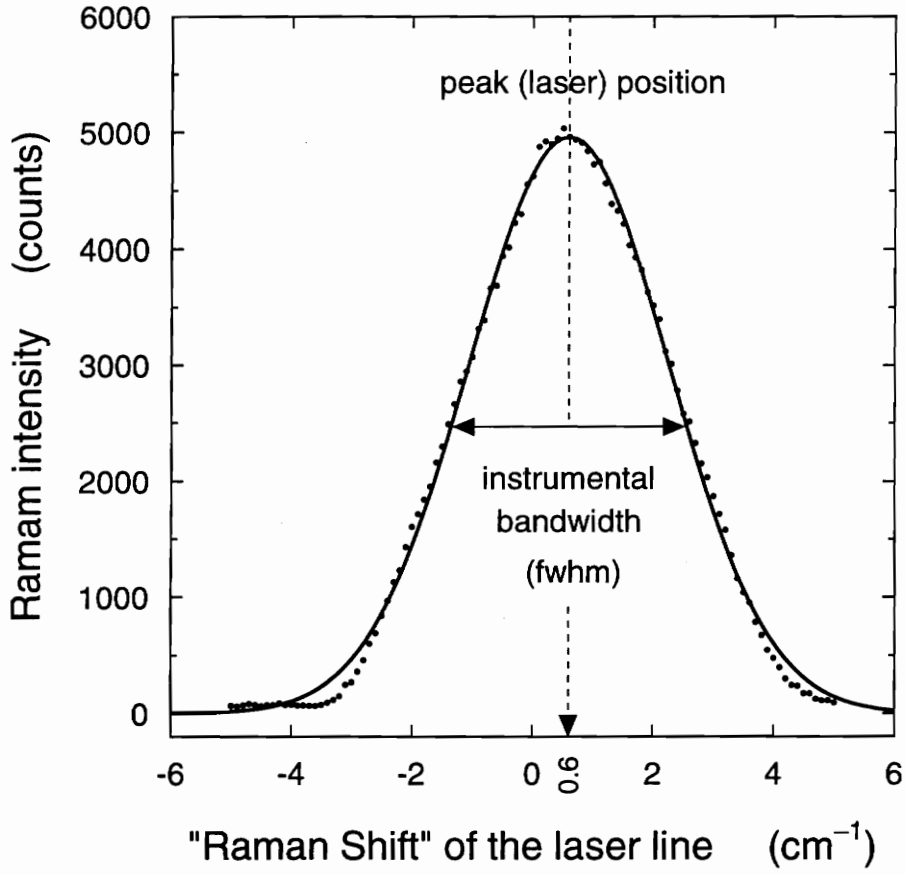

Fig. 2.4: A "Raman" spectrum obtained by scanning over the laser line. The black dots are actual data points. The solid line is a Gaussian fit to those points. This spectrum represents the transfer function, T, of eqn. (2.1). The instrumental bandwidth (B) is defined as the full width at half maximum (fwhm) of the transfer function. The laser peak position should reside at 0.0 cm^{-1}. Here, it is located at 0.6 cm^{-1}. This will lead to systematic offsets in the Raman data (offsets in the peak position of the phonon bands), that are easily taken into account (if the offset is known). Calibration of the Raman spectrometer means that you know what the offset is.

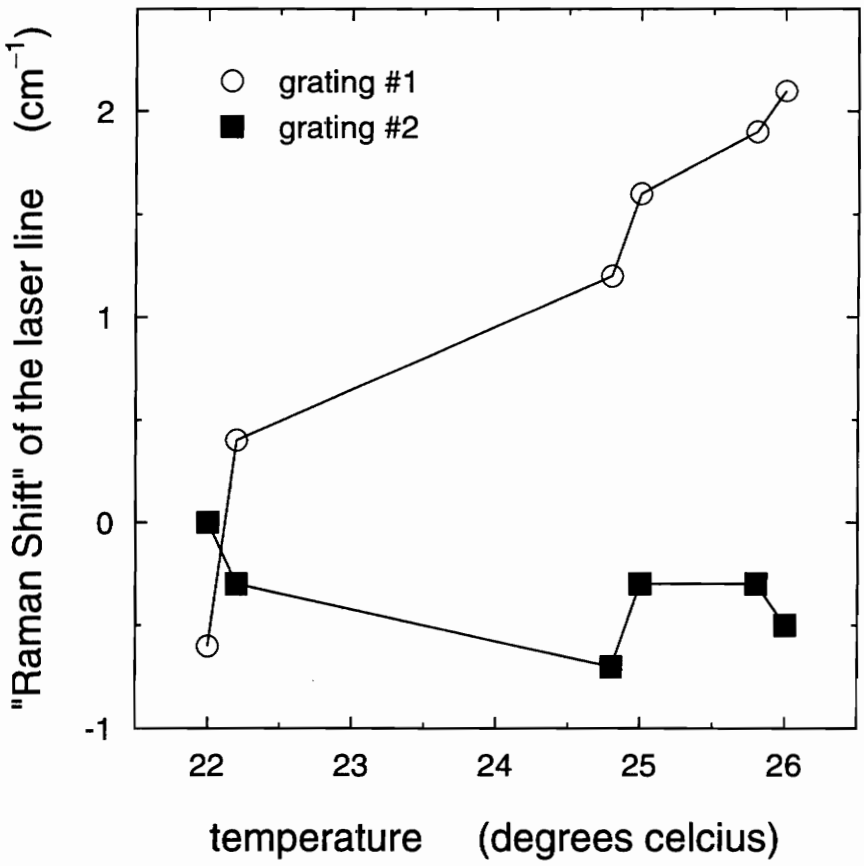

Fig. 2.5: The effect of temperature on the Raman spectrum. Each grating of the Raman spectrometer (Fig. 2.3) has an offset (Fig. 2.4). The open circle represents the offset of grating #1, and the solid square represents the offset of grating #2. Temperature effects the offset of each grating differently. Coordination of the gratings requires control of temperature swings in the Raman lab.

CHAPTER THREE

RAMAN STUDIES OF SOL-GEL ALUMINA: FINITE-SIZE EFFECTS IN NANOCRYSTALLINE AlO(OH)

3.1 Introduction

A sol-gel route to porous transparent alumina was established by Yoldas in 1975 in a series of widely cited papers.[1,2,3,4] "Sol-gel alumina " prepared by the Yoldas process is the prototypical example of a crystalline (meaning microcrystalline or nanocrystalline) gel.[5] Figure 3.1 presents a schematic of the synthesis procedure, as implemented in the present study. Since our study addresses the sol-gel aspects and the structure of the resulting gels, we omit the subsequent thermal treatments used to convert the gels to porous-yet-transparent alumina monoliths.[1]

The Yoldas process for sol-gel alumina includes three main steps:

(1) hydrolysis and condensation of an aluminum alkoxide in excess water to form an AlO(OH) precipitate;

(2) re-suspension and dissolution of the precipitate by acid peptization to form a clear, colloidal, sol;

(3) concentration of the sol by solvent boiloff, resulting in the formation of a gel.

The initial hydrolysis step is done with hot water, and the peptized sol is kept hot, in order to form AlO(OH) sols and gels rather than precipitates of $Al(OH)_3$ phases.[4,6] Alumina gels are mainly water and should properly be referred to as alumina hydrogels. Throughout this paper, whenever the term gel appears without

a modifier, alumina hydrogel is meant. Dried gels will be specifically referred to as xerogels.

In this chapter, we report the results of a systematic Raman-scattering investigation of sol-gel alumina materials as a function of process parameters, particularly the sol aging time (t_S in Fig. 3.1). Nanocrystalline boehmite, γ-AlO(OH), is shown (by Raman and x-ray measurements) to be the principal nonaqueous component and we have found small but systematic changes, as a function of t_S, in the lineshape and position of the dominant boehmite Raman band. These spectral changes have been interpreted in terms of nanocrystallinity-induced finite-size effects associated with the slow growth of AlO(OH) nanocrystals in the sol phase, and we have used them to determine estimates of characteristic nanocrystal sizes and growth kinetics in this system. This interpretation is supported by x-ray diffraction experiments (which provide the nanocrystal-size calibration for the Raman changes) and is consistent with crystal growth models.

Section 3.2 describes the experimental techniques used in the synthesis of, and measurements on, the sol-gel alumina materials. The Raman spectrum of crystalline boehmite is described in Sec. 3.3, as a necessary prelude to the measurements on the gels. Raman scattering from alumina gels, and the observation of systematic changes accompanying sol-gel processing, are described in Sec. 3.4. The interpretation in terms of nanocrystallinity and finite-size effects is given in Sec. 3.5. X-ray diffraction determination of nanocrystal sizes is described in Sec. 3.6, and results for the kinetics of nanocrystal growth are given in Sec. 3.7. Section 3.8 is a summary of our principal findings.

3.2 Experimental

A. Preparation of Alumina Gels

The Yoldas process for making clear alumina gels, as indicated in Fig. 3.1, consists of the three main steps listed in the introduction. The alkoxide we used, aluminum secondary butoxide (ASB), $Al(OC_4H_9)_3$, was doubly distilled and stored in an inert atmosphere chamber. ASB is a clear viscous liquid at room temperature. It was heated to reduce its viscosity, drawn into a hypodermic syringe, and added by syringe to the open reaction vessel containing water at 80 C under vigorous stirring conditions. The H_2O:ASB molar ratio was 110. ASB addition induces immediate hydrolysis and condensation reactions in the water-rich mixture[3,4,7] and yields an AlO(OH) precipitate.

The initial hydrolysis temperature of 80 C was chosen because it is the highest temperature compatible with avoiding violent boiling caused by the exothermic hydrolysis/condensation reactions. Following the ASB addition, the temperature controller was set to 95 C. It took about 20 minutes for the liquid to reach 95 C, partly because of the boiloff of the alcohol (secondary butanol) formed as a by-product of the hydrolysis reaction. Twenty minutes after hydrolysis/condensation, acid was added to cause peptization, the dispersion of the precipitate to form a clear, stable, colloidal sol. Two different acids (0.1 normal HNO_3 and 0.1 normal HCl) and two different acid concentrations (R=0.07 and R=0.14, where R is the acid/ASB mole ratio) were used in variations of the peptization procedure.

Following acid addition, the reaction vessel was closed (except for a very small syringe-needle hole to equalize pressure) to prevent solvent evaporation. The sol was then maintained, with continual stirring, at 95 C. At selected times, a

sol sample was removed by pipette from the reaction vessel, and boiled (for about ten minutes) in a small open beaker to remove water and concentrate. With sufficient water removal, the sol becomes viscous and approaches the gel point. The viscous sol was then transferred to a glass vial, sealed to retain the remaining water, and allowed to cool to room temperature. It then gelled within a few minutes.

These hydrogels are about 90% water, by weight[3]. Early gels (gels made from sols aged for only a few hours) are slightly cloudy; later gels (made from sols aged for many hours) are clear. The cloudiness is attributed to incomplete peptization for short sol aging times. Once a gel is formed, its degree of cloudiness or clarity does not change, nor does its Raman spectrum. As described in Sec. 3.4, Raman studies reveal structural differences, in the gels, which depend on the amount of time spent by the parent sol in the reaction vessel.

B. Preparation of Related Materials

A series of samples were prepared with a procedure similar to that of Fig. 3.1, with the key difference of omitting the acid-addition peptization step. These materials remain as precipitates, in contact with the hot, stirred, aqueous bath in the form of a cloudy suspension. At selected times, a sample of the suspension was removed and centrifuged to remove most (about 75%) of the water. The resulting white mush was then oven dried at 110 C for 24 hours, yielding brittle white chunks. Raman studies of these dried precipitates (Sec. 3.4) reveal that their structure, like that of the gels, also depends on history, the time spent in the reaction bath.

In addition to the hydrogels and the precipitates, a few other samples were investigated. Portions of some of the hydrogels were subjected to a 110 C oven

drying step (like that used for the precipitates), removing their water content and yielding xerogels in the form of transparent chunks. An unpeptized precipitate (referred to as a 130 C precipitate) powder sample was made by adding ASB to H_2O (ASB:H_2O was 110) and processing the sol in a pressure vessel at 130 C for about five days. The sol was then dried in an oven at 110 C. The product of this process was a white powder. A sample of crystalline boehmite powder (composed of micron-size crystals), prepared by autoclaving aluminum metal in excess water, was provided by Alcoa laboratories. X-ray diffraction confirmed that the material was well-crystallized boehmite.

C. Raman Scattering Experiments

Raman spectra (Stokes spectra) were obtained at room temperature, using a SPEX 1403 Raman spectrometer with a GaAs-photocathode photomultiplier and photon-counting electronics. A CW argon ion laser, operating at 488.0 nm or 514.5 nm, was the excitation source. The laser power at the sample was approximately 80 mW. We used an instrumental bandwidth of 3.8 cm^{-1} and a 0.5 cm^{-1} grating step size. Spectra were obtained in the 90° scattering configuration, collecting both polarizations of scattered light. For the hydrogels, spectra were taken with the gel held in its vial, laser light entering from the bottom and scattered light collected through the side (each sample was scanned for a total of 40 minutes). The beam focus was inside the gel; no spectral features attributable to the glass vial were observed. Xerogels and precipitates were measured in air, glued onto a capillary tube. The crystalline boehmite powder and the 130 C precipitate powder were held in capillary tubes for Raman measurements.

The experimental Raman linewidth is a convolution of the actual linewidth

Γ and the instrumental bandwidth Γ_{inst}, via $\Gamma_{expt} = (\Gamma^2+\Gamma^2_{inst})^{1/2}$. In the analysis presented,[8] we use the (deconvoluted) results for the estimated actual linewidth Γ.

D. X-ray Diffraction Experiments

X-ray diffraction traces were obtained at room temperature, using a Scintag XDS-2000 powder diffractometer and CuKα radiation with a wavelength of 1.54 Å. The x-ray measurements were carried out on powder samples (prepared by gentle grinding of the dried precipitate or hydrogel) placed on an oriented quartz substrate. Diffraction done directly on hydrogel films cast on the substrate missed several boehmite peaks because of drying-induced preferred orientation,[9] so powder samples were prepared by room-temperature drying of the hydrogels, followed by gentle grinding.

Crystallite sizes were determined by the Scherrer equation[10],

$$B(2\theta) = \frac{0.94\lambda}{L\cos\theta}, \qquad (3.1)$$

where L is the microcrystallite size, θ is the peak position, and $B(2\theta)$ is the linewidth. Linewidth corrections for x-ray instrumental broadening were performed in the same manner as they were for the Raman linewidths[10].

3.3 Raman Spectrum of Boehmite [AlO(OH)]

Boehmite, γ-AlO(OH), is the predominant phase present in the alumina gels formed by the Yoldas process of Fig. 3.1. It is therefore necessary to consider first the Raman spectrum of this crystal form. The crystal structure of boehmite is shown in Fig. 3.2.[11,12] The structure is orthorhombic, space group Cmcm (D_{2h}^{17}), with two AlO(OH) formula units per primitive cell. The symmetric unit cell shown in Fig. 3.2 contains two primitive cells. The structure is based on

extended layers that run perpendicular to the b-axis; parts of two layers are shown in Fig. 3.2. There is ionic/covalent bonding within each layer, but only hydrogen bonding between layers. Within each multilevel, strong-bonding, layer there are two planes of aluminum atoms and four planes of oxygen atoms. Each aluminum is bonded to six oxygens in a distorted octahedron. The interior oxygens (those on the two inner oxygen planes) are each bonded to four aluminums in a highly distorted tetrahedron. The outer oxygens (actually hydroxyls, since each carries a hydrogen) are each bonded to only two aluminums.

An appropriate reference for comparison is α-Al_2O_3 (corundum, also called sapphire or alumina). In the 3d-network structure of α-Al_2O_3, each aluminum is coordinated to six oxygens and each oxygen to four aluminums. The average coordination is 4.8, compared to an average Al-O coordination of 4.0 within a boehmite layer. For α-alumina, Raman[13] and infrared[14] studies place the optical phonons in the range from 380 to 750 cm^{-1}. For boehmite, the lower coordination is expected to extend the Al-O optical-phonon regime to lower frequencies, and we find this to be the case.

The strongest Raman line we observe in γ-AlO(OH) occurs at 363 cm^{-1}. Its strength, as well as the observation (discussed below) that its depolarization ratio is zero, marks it as a fully symmetric mode (A_g; there are three of this symmetry), in which all aluminums and oxygens move parallel to the b-axis. The six vertical arrows in Fig. 3.2 show one possible A_g-symmetry vibrational eigenvector (we can treat each hydroxyl as a rigid entity, for a low-frequency mode, so only six arrows are needed) which has intralayer-shear bond-bending character, but a definitive assignment awaits a more detailed force-field analysis.

TABLE 3.1. Raman peak positions for crystalline boehmite, AlO(OH).

Frequency (cm^{-1})	Linewidth[a] (cm^{-1})	Relative Intensity
230	3.2	weak
259	2.6	weak
270	2.4	weak
341	3.2	medium
363.3	3.0	very strong
454	7.3	medium
496	6.3	strong
638	10.9	weak
677	12.4	medium
733	9.5	weak
3079	47	medium
3219	37	medium

[a]The linewidth means full-width-at-half-maximum (fwhm), and is corrected for the instrumental broadening via $(\text{fwhm})^2_{\text{observed}} = (\text{fwhm})^2_{\text{actual linewidth}} + (\text{instrumental spectral slit width})^2$.

Figure 3.3 presents Raman-scattering results obtained from boehmite powder composed of micron-scale crystallites.[15] At these relatively large particle sizes, the observed spectrum should be indistinguishable from that of the bulk crystal. This is supported by the sharpness of the Raman lines in Fig. 3.3. (An x-ray diffraction spectrum for this sample, displaying sharp lines, is shown in section 3.6.)

The spectral region shown in Fig. 3.3 contains the lattice-mode regime, i.e., the modes are predominantly Al-O vibrations. Table 1 lists the peak positions, linewidths, and relative intensities of the Raman lines of boehmite. The linewidth given is the full width at half maximum (fwhm), after correcting for the instrumental broadening. The sharp, intense line at 363 cm^{-1} is the dominant spectral signature of boehmite. The lineshape variations of this feature, as observed for the gel samples, will play an important role in our analysis.

Figure 3.4 shows the polarization dependence of the 363 cm^{-1} line. (For this nanocrystalline sample, the line is downshifted to 359 cm^{-1}.) These spectra are for a hydrogel, peptized with HNO_3 (R=0.07), and aged in the sol phase for 48 hours. These clear hydrogels are convenient for depolarization studies because of their low scattering background and the random orientation of the crystallites. The clean diagonal polarization exhibited in Fig. 3.4 supports the fully symmetric A_g-symmetry interpretation for the 363 cm^{-1} Raman band.

In comparing our results to earlier reports on boehmite[16,17,18], we have discovered that considerable confusion has existed in terms of Raman lines attributed to boehmite and boehmite gels. Specifically, we have found that several high-frequency lines, which have masqueraded in the literature as boehmite modes, are actually internal modes of the NO_3^- nitrate ion. Figure 3.5

compares spectra that we have observed for boehmite crystals (lower panel), an alumina hydrogel or "boehmite gel" (middle panel), and nitric acid (upper panel). The gel was prepared as in Fig. 3.1, using HNO_3 as the peptizing acid. Note the four Raman bands indicated by the vertical lines (at 720, 1049, 1348, and 1414 cm^{-1}), especially the strong, sharp line at 1049 cm^{-1}. All of these are present in both the HNO_3 and the gel spectra, and all are absent in the spectrum of boehmite. These four bands correspond to NO_3^- vibrations.[19,20] The symmetric-stretch nitrate line at 1049 cm^{-1} has been erroneously assigned to boehmite, and the asymmetric stretching line at 720 cm^{-1} has been erroneously assigned to boehmite gels. Also, the 1348 and 1414 cm^{-1} lines have been misassigned as organic features in the boehmite gels. All boehmite-gel spectra that have been reported to exhibit these lines were obtained on samples that were either peptized with HNO_3 or involved $Al(NO_3)_3$ in their synthesis. The attribution of extraneous lines to the Raman spectrum of boehmite has prevented a correct group-theoretical interpretation of the zone-center vibrations in this crystal; we plan to rectify this in a future paper.

A comparison of the spectra in the lower two panels of Fig. 3.5 confirms that boehmite AlO(OH) is indeed the primary component (other than water) in the hydrogel. The 363 cm^{-1} signature of the crystal is prominent in the gel, but, as we shall see, this line is actually broadened and shifted with respect to the crystal line.

3.4 Raman Scattering from Alumina Gels:

Systematic Changes during Sol-Gel Processing

In the synthesis procedure for sol-gel alumina that is outlined in Fig. 3.1, the primary processing variable of interest in this study is the sol aging time t_S.

Secondarily, we have also studied the effect of varying (or omitting) the acid peptization step. Although gel samples produced after different times t_s all exhibit Raman spectra which, in overall appearance, resemble that shown in Fig. 3.5b, we have observed definite systematic changes as t_s is varied. As noted in Sec. 3.2, after gelation is achieved by concentrating and cooling the aged sol, no further structural changes are observed.

The gel Raman features that we have followed, as a function of sol aging time, are the position, linewidth, and asymmetry of the prominent boehmite band near 360 cm^{-1}. Figure 3.6 shows a detailed view of this band, observed for a sample corresponding to t_s = 24 hours. The experimental linewidth Γ_{expt} (Γ_{expt} = lw + rw) is the observed full width at half maximum. The asymmetry is defined as lw/rw. The experimental linewidth is a convolution of the actual linewidth Γ and the instrumental broadening Γ_{inst}, $\Gamma_{expt} = (\Gamma^2+\Gamma_{inst}^2)^{1/2}$; in the following analysis we present the (deconvoluted) results for the estimated actual linewidth Γ.

Figure 3.7 shows the 360 cm^{-1} band for a series of samples with t_s values varying from 1 to 72 hours. In panels a through d, the experimental data are shown as solid dots, while the lines are fitted curves useful for comparing and analyzing the data. (The curves are eight-parameter fits, using two Gaussians and a linear baseline. The fitted curves were used to determine the peak positions and linewidths.) Panel e of Fig. 3.7 shows a superposition of the curves; like panels a-d, it demonstrates that the band upshifts and narrows with increasing sol aging time at 95 C.

Figure 3.8, which represents our principal findings for the influence of preparation procedure on the boehmite-band position and lineshape in the sol-gel alumina materials, summarizes results obtained from about seventy samples, via

spectra such as those in Fig. 3.7. Figure 3.8 presents the observed correlation between peak position and linewidth. The main family of materials, represented in Fig. 3.8 by the solid triangles, are the hydrogels prepared by the process of Fig. 3.1, with the peptization step carried out with nitric or hydrochloric acid (with acid/ASB ratios of 0.07 and 0.14). In addition, several other types of samples were investigated and have been included in Fig. 3.8. Boehmite itself (via more detailed data than shown in Fig. 3.5c) is included as the solid square labeled "bulk crystal" at the lower left of Fig. 3.8. This corresponds to the smallest linewidth and highest peak position for the 360 cm^{-1} band; it represents the limiting values.

The central result displayed by the extensive data contained in Fig. 3.8 is the position-versus-linewidth correlation represented by the solid straight line. This line is a fit to the gel data (the solid triangles, about fifty samples) in the upper part of the figure; the bulk-crystal point at the lower left (not included in the fit) lies close to the extrapolation of this line. Within this hydrogel data set, the gels represented by points furthest to the upper right correspond to the shortest sol aging times. With increasing gel-sample t_S, the points track down and to the left, systematically heading in the direction of the bulk-crystal point.

A second result is indicated by the dashed line in Fig. 3.8. This is a linear fit to the data set (the open squares) corresponding to the unpeptized precipitates prepared by omitting the acid-addition step in Fig. 3.1. This family of materials also exhibits an approximately linear position/linewidth correlation, but one that is slightly shifted with respect to the line describing the correlation for the gel samples.

Results for a few other types of sol-gel alumina samples are included in Fig. 3.8. The xerogels (represented by the open triangles) were made by drying

selected hydrogel samples (indicated by the tie lines) at 110 C. The 130 C powder precipitate was an unpeptized sample held at 130 C for five days in a closed vessel. For all of these samples, the position/linewidth parameters define points which lie in or near the narrow band marked by the two lines in Fig. 3.8. Interpretation of the correlations revealed by these data is discussed in the next section.

3.5 Nanocrystalline Boehmite

The points at the top right of Fig. 3.8, for which the boehmite-like band is substantially broadened and downshifted relative to the bulk-crystal band, correspond to alumina gels prepared using the shortest sol times (t_1, t_2, ...) in the procedure of Fig. 3.1. For longer reaction times, the band exhibited by the resulting gels is seen to narrow and upshift; the spectral parameters tend toward those of the bulk crystal. This systematic variation in the Raman spectrum evidently probes a systematic variation in the structure and/or the composition of the gel, as a function of sol aging time.

The main candidate for a stoichiometric explanation of the observed Raman changes involves the possible incorporation of excess water within the boehmite phase. Intercalation of water into the interlayer (hydrogen bonding) regions in boehmite has been suggested in the literature,[21] but clear evidence for this has not been presented. We consider a variation in interlayer water content to be an unlikely explanation of the results of Fig. 3.8. The bulk crystal is the endpoint corresponding to very long aging times, which seems inconsistent with an excess-water explanation.

It has also been suggested that bond-length and bond-angle variations might account for the increased linewidth in the gel. This idea implicitly appeals to an

analogy with silica gel, which is closely related to amorphous SiO_2 -- a covalently bonded, low coordination number, continuous random network, bulk glass that is characterized by a broad distribution of Si-O-Si bond angles[22]. But the analogy between alumina gel and silica gel is wrong for many reasons. The alumina system is primarily ionic, not covalent. There is no bulk alumina glass analogous to silica glass. Coordination numbers in crystalline Al_2O_3 are significantly higher than in SiO_2: 6 for Al and 4 for O in Al_2O_3 versus 4 for Si and 2 for O in SiO_2. Silica glass is a classic Zachariasen structure constructed of corner-sharing SiO_4 tetrahedra; the bridging oxygens provide the flexibility needed to form the random network. Al_2O_3, AlO(OH), and $Al(OH)_3$ are all based on edge-sharing AlO_6 octahedra (nearby aluminums are joined by two oxygens); the geometrical constraints enforce crystalline structures. Thus alumina gel is predominantly microcrystalline or nanocrystalline rather than amorphous, and there is little scope for bond-length or bond-angle variation.

The observed correlation between Raman linewidth and peak position, exhibited in Fig. 3.8 for the boehmite-like signature characteristic of the family of materials known as sol-gel alumina, bears a strong resemblance to a well-documented phenomenon observed in nanocrystalline semiconductors: the finite-size effect of nanocrystallinity (microcrystal dimensions of order 10 nm) on Raman position and lineshape.[24,25,26,27,28,29,30] The gist of the mechanism is as follows. For a nanocrystal of size L, the strict "infinite-crystal" k-space selection rule is replaced by a relaxed version characterized by a k-space uncertainty of order (1/L). Here, k is the phonon wavevector. Instead of only the k=0 mode of a phonon branch being Raman-active (for a Raman-allowed mode symmetry), now all modes of the phonon branch within a range of k values

[roughly from k=0 up to k=(1/L)] are Raman-active. Because the phonon dispersion curve $\nu(k)$ is not flat, the observed Raman band shifts and broadens. The smaller is L, the larger is the shift and broadening of the Raman band. The x-ray results of the following section show, in fact, that in our materials, L decreases in the decreasing-time direction (the direction of increasing shift and increasing broadening) in Fig. 3.8. The L scale along the right side of Fig. 3.8 is based on the x-ray-derived average crystallite sizes discussed in Sec. 3.6.

Both the clear correlation in Fig. 3.8 between peak position downshift and linewidth broadening, as well as the magnitude of the measured changes in these quantities, are similar to what is observed in nanocrystalline semiconductors. A second conspicuous feature of Fig. 3.8 is the small but real offset of the line representing the precipitate samples relative to the line representing the main family of samples, the hydrogels. Before discussing this interesting effect, we first present, in Fig. 3.9, additional sets of results for the lineshape changes.

Figure 3.9 shows the correlation between linewidth and lineshape asymmetry (upper panel of the figure) and between peak position and asymmetry (lower panel). Here the lineshape asymmetry information is contained in the ratio (lw/rw), where lw and rw are the left and right halfwidths illustrated in Fig. 3.6. For a symmetric band, this ratio is unity; this is close to the case observed for bulk boehmite. The most asymmetric lineshapes are observed for the short-time gels, for which the observed ratio is about 1.3. The asymmetry is small and thus the scatter is substantial, but Fig. 3.9 does show that linewidth, peak position, and asymmetry are mutually correlated.

In Fig. 3.8, there is an offset between the lines describing the two large populations of samples: hydrogels and precipitates. In Fig. 3.9a, data from both

populations overlap and no such separation or offset is evident. But in Fig. 3.9b, we can again see a definite separation, as in Fig. 3.8. Our interpretation of these observations, in terms of nanocrystal-size arguments, is given below.

For a single nanocrystal diameter L, the finite-size model yields a single value for each of the three Raman-band characteristics: peak position, linewidth, and lineshape asymmetry. For a distribution of nanocrystal sizes having a peak at L and a spread schematically denoted by δL, the Raman peak position is determined by L but the linewidth and asymmetry are increased over the single-L ("monodisperse") value by contributions arising from the particle-size spread δL. We interpret the hydrogel/precipitate Raman-band offset, discernible in Figs. 3.8 and 3.9b but absent in 3.9a, as evidence that δL is larger for the nanocrystal distribution in the precipitates than for the nanocrystal distribution in the hydrogels. In other words, the precipitates exhibit more inhomogeneous broadening than the hydrogels. A comparison of hydrogel and precipitate spectra, for bands with similar peak positions, reveals that the main difference is that the left halfwidth (lw of Fig. 3.6) is larger for the precipitates. This accounts for the offset between the two populations seen in Figs. 3.8 and 3.9b, as well as the absence of an offset in Fig. 3.9a (since an increase in lw increases both linewidth and asymmetry, approximately preserving the linewidth/asymmetry correlation).

An increased low-frequency wing (larger lw) for the Raman band of the precipitates implies a larger spread in the particle-size distribution on the small-particle side. A possible explanation for an increase in the number of small nanocrystals is the 110 C drying step experienced by the precipitates (but not, of course, the hydrogels). During this step, the concentration of aluminum-containing solute species increases drastically, and at some point it exceeds the

critical supersaturation for nucleation. The resulting additional burst of nucleation gives rise to a population of small nanocrystals, which is responsible for the increased dispersion on the small-L side of the particle-size distribution.

To test this idea, we subjected three of the hydrogels to the same 110 C drying step experienced by the precipitates. The results are included in Fig. 3.8 as the three pairs of triangles connected by tie lines. For each pair of points, the filled triangle corresponds to the initial hydrogel and the open triangle corresponds to the xerogel produced by drying that hydrogel at 110 C. All three tie lines move the initial point to the right, to larger linewidth. Two of the xerogel points are seen to lie near the line describing the precipitates, while the smallest-L case has moved part way in the same general direction. These results are consistent with the picture of increased small-particle dispersion caused by a late, drying-induced, burst of nucleation.

The open circle in Fig. 3.8 is for a precipitate which, directly after formation by hydrolysis/condensation in the 1:110 ASB/water liquid, was transferred (precipitate plus liquid) to a closed pressure vessel and held at 130 C for five days. It was then removed and dried at 110 C, leaving a white powder. This sample can be viewed as an exercise in boehmite crystal growth. In Fig. 3.8, its position is the closest one to the bulk crystal point. It is also worth noting that it lies near the main line rather than the offset line, showing that the offset is not associated with the absence of acid (since this sample was acid-free).

The nanocrystal particles in contact with the sol (the nanocrystals in the colloidal sol, for the liquids that precede the hydrogels, and the nanocrystals forming the precipitate for the unpeptized stirred suspensions) are presumed to grow in size by the dissolution and re-precipitation of an amorphous Al-containing

component, or possibly an assembly of clusters, that is formed in the initial hydrolysis/condensation reactions between ASB and water. Such a source of alumina can account for the growth of the boehmite signal that we see. In the case of the 130 C precipitate discussed above, it appears that the source has been depleted during the five-day period of crystal growth, since we see no spectral evidence of a final burst of nucleation caused by the drying step.

The crystalline character of all of these sol-gel materials (hydrogels, xerogels, precipitates) is attested to by the unambiguous signature of crystalline boehmite in the Raman spectra. The six strongest lines of the crystal (all those listed as medium or stronger in Table 1, except for the 733 cm^{-1} line) all appear in the gel spectra. In addition, transmission electron diffraction on gel films (prepared by allowing an aged sol to dry by evaporation on a sample grid) exhibited many sharp diffraction rings. X-ray diffraction data, described in the next section, confirm the crystallinity and provide a valuable calibration of microcrystallite size.

3.6 X-ray Diffraction Determination of Nanocrystal Sizes

X-ray diffraction experiments were performed on several of the materials for which Raman results were given in Fig. 3.8. Measurements were done on samples in powder form, as described in Sec. 3.2D. The x-ray linewidth results were used to estimate average crystallite sizes by means of the Scherrer equation, Eqn. 3.1.

Figure 3.10 shows the x-ray diffraction data. The peak assignments are given with respect to the γ-AlO(OH) orthorhombic Cmcm crystal structure[11,31]. At the bottom (trace a) is the result obtained for a powder composed of micron-size crystals; this trace exhibits very narrow linewidths (about 0.1°) and is the

pattern expected for bulk crystalline boehmite. The traces b through g show progressively broader linewidths (up to a few degrees), indicating progressively smaller crystallite sizes. The low-angle (020) band becomes asymmetric and shifts to higher d values as the linewidths increase, while the (021) and (131) bands remain symmetric and do not shift with linewidth broadening. The (021) and (131) peaks were used for crystallite size determination by the Scherrer method. They gave consistently similar results, as seen in Fig. 3.11.

Figure 3.11 presents the correlation between the crystallite size, as determined by x-ray diffraction, and the Raman peak position and linewidth (of the 360 cm^{-1} band) observed for the same sample. The symbols used in this figure correspond to the same convention used in Fig. 3.8. For each Raman determination (vertical location) there are two x-ray determinations (horizontal locations), corresponding to the (021) and (131) diffraction peaks The range of crystallite sizes is seen to extend down to about 3 nm (justifying our use of the terms nanocrystal and nanocrystallinity).

The top x-axis scale in Fig. 3.11 gives the crystallite size L; the bottom x-axis scale gives L^{-1}. The scale along the upper right side gives the downshift $\Delta\bar{\nu}$ of the Raman peak position, relative to the peak position for the infinite crystal. The two straight lines are least-squares linear-in-L^{-1} fits to the data:

$$\Delta\bar{\nu} = k_1 \frac{1}{L} \tag{3.2}$$

and

$$\Gamma = k_2 \frac{1}{L} + \Gamma_0 \tag{3.3}$$

where Γ is the linewidth, and k_1, k_2, and Γ_0 (21.5 cm^{-1}•nm, 39.2 cm^{-1}•nm and 2.7 cm^{-1} respectively) are determined from the fit. These calibration relations,

connecting Raman peak-position and linewidth with crystallite size, were used to obtain the right hand scale in Fig. 3.8. They are also used in the next section, to determine $L(t_S)$ growth kinetics.

A linear relationship between Raman peak-position and $L^{-\alpha}$, with α=1.0, has also been seen in graphite[29] and boron nitride.[30] It is noteworthy that boehmite, like graphite and BN, possesses a layered structure (as discussed in Sec. 3.3). In terms of α, which is an empirical Raman-versus-size scaling exponent, these layered materials behave differently than the covalent-network semiconductors silicon [23,32] and gallium arsenide.[24,33] Our analysis of the reported Raman results[23,24,32,33] for the network semiconductors yields, for those materials, a scaling exponent α of about 1.5.[34]

3.7 Kinetics of Nanocrystal Growth

Figure 3.12 displays the results of individual sample-preparation runs, showing the dependence of the boehmite-signature Raman-band peak position of the hydrogel on the sol aging time (t_S in Fig. 3.1). Results are shown for both of the acids used in the peptization step, HCl and HNO_3, and for both acid concentrations used, R=0.07 and R=0.14 (R is [H]/[Al], the acid/ASB mole ratio). Also included (panel c) are results for the precipitates obtained in an acid-free run. All of the runs were well represented by fits of the form

$$\bar{\nu}(t)-\bar{\nu}(0) = r\cdot t^{1/2} \quad . \tag{3.4}$$

The curves shown in Fig. 3.12 correspond to Eqn. 3.4, with the best-fit parameters, $\bar{\nu}(0)$ and r, listed in Table 2. The precipitate behavior clearly differs from the rest in its larger $\bar{\nu}(0)$. For the gels, $\bar{\nu}(0)$ is smaller for the higher acid concentration, but there is no discernible difference between the use of HCl and HNO_3 as peptizing agent. The rate constant r increases with increasing acid concentration.

Table 3.2. Parameters obtained from the rate-equation fits [equations (4), (5), and (6) in the text] to the data of Figs. 3.12 and 3.13.

panel in Fig. 12	Acid	Acid Conc. ([H]/[Al])	$\nu(0)$ (cm^{-1})	r ($cm^{-1} \cdot hour^{-1/2}$)	$L_2(0)$ (nm)	s_2 ($nm^2 \cdot hour^{-1}$)	$L_3(0)$ (nm)	s_3 ($nm^3 \cdot hour^{-1}$)
a	HCl	R=0.07	356.4	0.32	3.3	0.22	3.3	1.3
b	HCl	R=0.07	356.3	0.31	3.2	0.19	3.2	1.1
c	-----	R=0.0	358.1	0.33	4.5	0.70	4.4[a]	6.3[a]
d	HCl	R=0.14	355.7	0.44	3.0	0.27	3.0	1.5
e	HCl	R=0.14	355.9	0.39	3.1	0.24	3.0[a]	1.5[a]
f	HNO_3	R=0.14	355.8	0.38	3.0	0.21	3.0	1.2
g	HNO_3	R=0.07	356.1	0.30	3.1	0.18	3.1	1.0
h	HNO_3	R=0.07	356.2	0.25	3.2	0.14	3.1	0.7
i	HNO_3	R=0.07	356.1	0.33	3.2	0.20	3.1	1.1

[a]The curves that correspond to these parameters are shown in Fig. 3.13.

As the characteristic microcrystallite size increases, the finite-size-induced downshift of the Raman peak position is reduced, and the peak moves upward toward its bulk crystal value of 363 cm^{-1}. Using the results of the last section, we can make this interpretation quantitative by invoking the $\Delta\bar{\nu}(L)$ scaling relation of Eqn. 3.2, which connects the left and right scales of Fig. 3.8. Each set of $\bar{\nu}(t)$ data, corresponding to the set of points contained in a panel of Fig. 3.12, is thus transformed to a set of L(t) data, with L the crystallite size. The results obtained for panels c and e of Fig. 3.12 are presented in Fig. 3.13.

All of the hydrogels represented in Fig. 3.12 yield L(t) results similar to the HCl R=0.14 data (panel e of Fig. 3.12, lower part of Fig. 3.13) shown in the lower part of Fig. 3.13. The precipitate run (panel c of Fig. 3.12, upper part of Fig. 3.13) is distinctly different. The curves shown in Fig. 3.13 are fits of the form

$$\left[L_3(t)\right]^3 - \left[L_3(0)\right]^3 = S_3 \cdot t \qquad (3.5),$$

where $L_3(0)$ and S_3 are the fit parameters. This form was found to adequately describe all of the L(t) results; the values obtained for $L_3(0)$ and S_3 are given in the last two columns of Table 2. Also included in Table 2 are results to fits of the form

$$\left[L_2(t)\right]^2 - \left[L_2(0)\right]^2 = S_2 \cdot t \qquad (3.6),$$

that also describes the experimental results, within the statistical error bars shown.

The time dependence exhibited by $L_{2,3}(t)$ is similar to that found in various theories of crystal growth,[35,36] which come under the general heading of Ostwald ripening. Ostwald ripening (coarsening, coalescence, or just ripening) is basically a zero-sum game in which larger particles grow at the expense of smaller particles; for our purposes, the larger particles are nanocrystalline boehmite, and the smaller particles are amorphous or incompletely crystallized AlO(OH). Our results are

quite consistent with the often-invoked cubic-law behavior (Eqn. 3.5) corresponding to the fitted curves in Fig. 3.13, but our data are not accurate enough to rule out parabolic-law behavior (Eqn. 3.6).

The unpeptized precipitate sample included in Figs 3.12 and 3.13 and Table 2 is characterized by a larger "initial" crystallite size [L(0)] and by a faster growth rate (s) than the peptized sols. Acid peptization limits early crystal growth. Overall, both acids used for preparation of the sols yield quite similar results. No difference is observed between HCl and HNO_3 in terms of the L(0) values obtained, but increasing the acid concentration from R=0.07 to R=0.14 does reduce L(0) slightly, an effect which may reflect faster peptization (and reduced opportunity for early growth) at the higher concentration. The subsequent growth rate seems to be slightly larger with HCl than with HNO_3 and, for both acids, growth occurs somewhat more quickly at the higher acid concentration. But in all cases the growth is very slow, so that the gelation step yields hydrogels of nanocrystalline boehmite.

3.8 Summary

A systematic Raman-scattering investigation has been carried out on sol-gel alumina prepared by the Yoldas process of Fig. 3.1, primarily as a function of the sol aging time, but also secondarily as a function of the acid peptization step (including its omission). The predominant aluminum-containing component of the alumina hydrogels and precipitates is nanocrystalline boehmite, γ-AlO(OH), and in the course of this work we have clarified certain aspects of the boehmite Raman spectrum.

A careful study was made of small but systematic changes observed, as a function of the process parameters, in the lineshape and position of the dominant

boehmite band near 360 cm^{-1}. The position/linewidth correlation established by the data in Fig. 3.8, as well as the more subtle lineshape asymmetry correlations of Fig. 3.9, have been interpreted in terms of nanocrystallinity-induced finite-size effects associated with the slow growth of the γ-AlO(OH) nanocrystals during the sol phase. X-ray diffraction experiments were used to determine nanocrystal sizes (as small as 3 nm for gels prepared from fresh sols) and to estimate growth kinetics from the Raman-lineshape results. The Raman peak-position shift is proportional to $L^{-\alpha}$, where L is the average nanocrystal size and α is a Raman-versus-size scaling exponent. For AlO(OH) we find α to be 1.0, close to scaling-exponent values reported for graphite and BN and different from the value of 1.5 which describes the reported behavior of Si and GaAs.

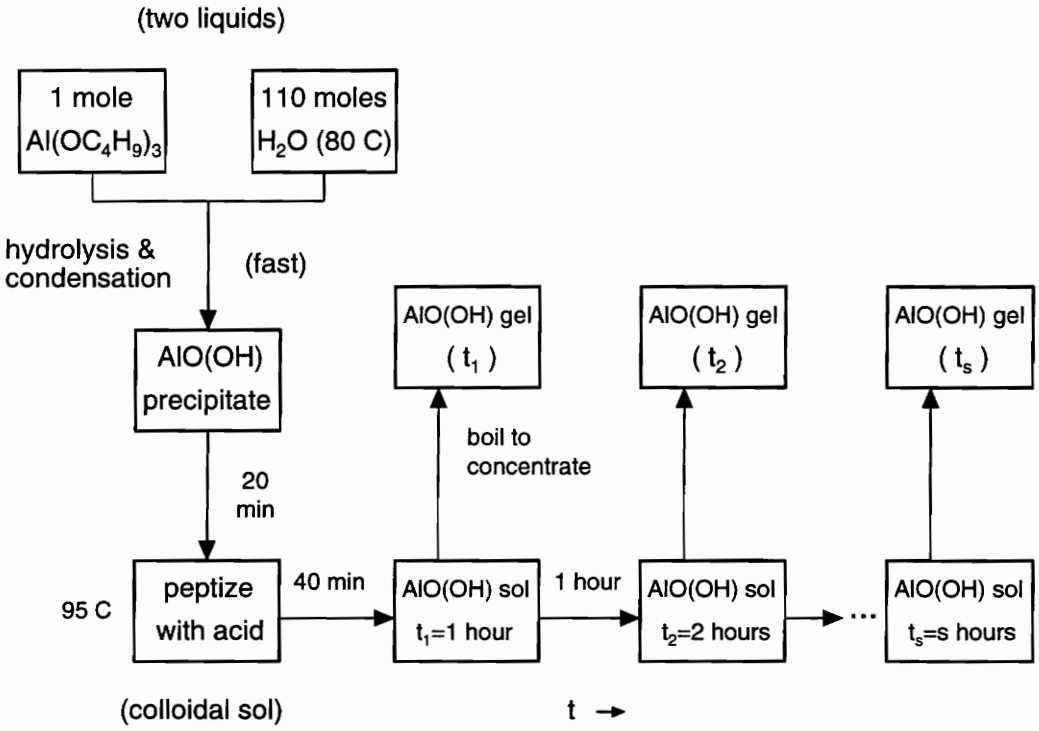

Fig. 3.1: Schematic of our implementation of the Yoldas process for synthesizing sol-gel alumina. After time t_S in the sol phase at 95 C, gelation was brought on by boiloff-induced concentration. Raman studies were done on hydrogels prepared using various sol aging times (t_S), and the effect of varying the acid peptization step in the synthesis was also studied.

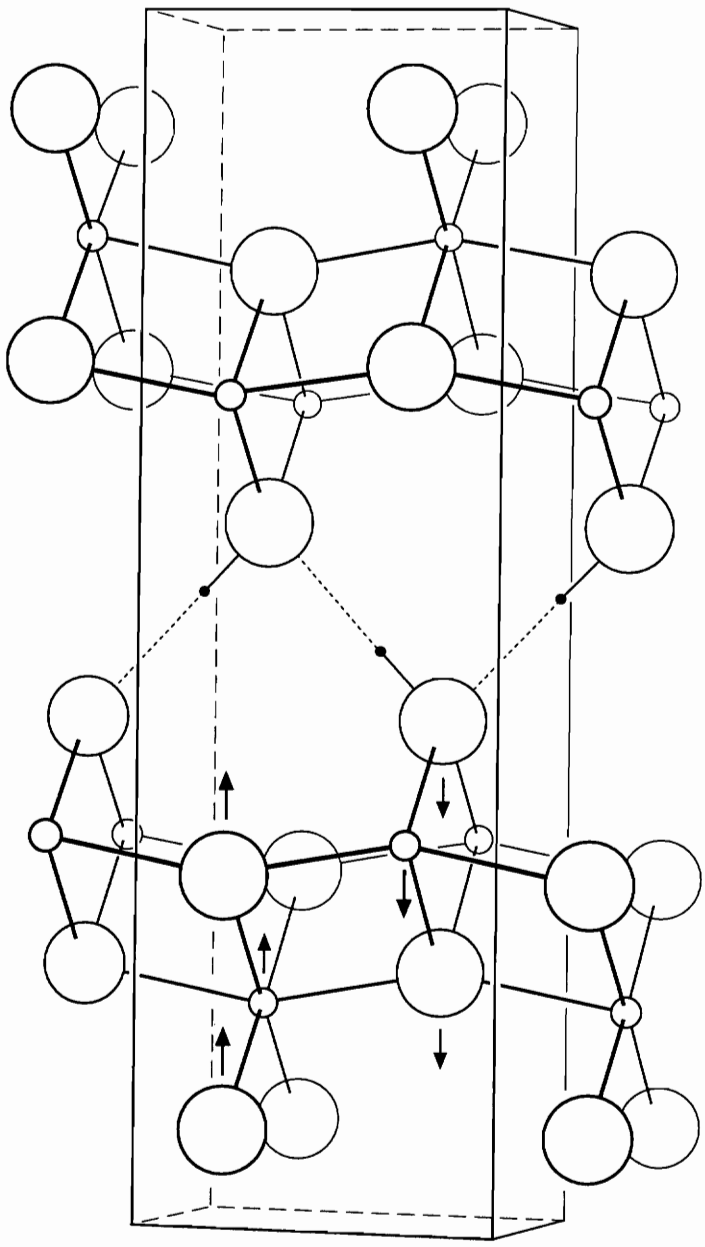

Fig. 3.2: The crystal structure of boehmite, γ-AlO(OH). This is a perspective view from a distance of 50 Å, looking along a direction 15° off the a-axis in the ac plane (see Ref. 3.12). The cell shown is a symmetric unit cell, which contains two primitive cells. Oxygens are represented by the large spheres, aluminums by the small spheres, and hydrogens by the solid dots. The six arrows, attached to the aluminums and oxygens within one primitive cell, represent a vibrational eigenvector having the full crystal symmetry.

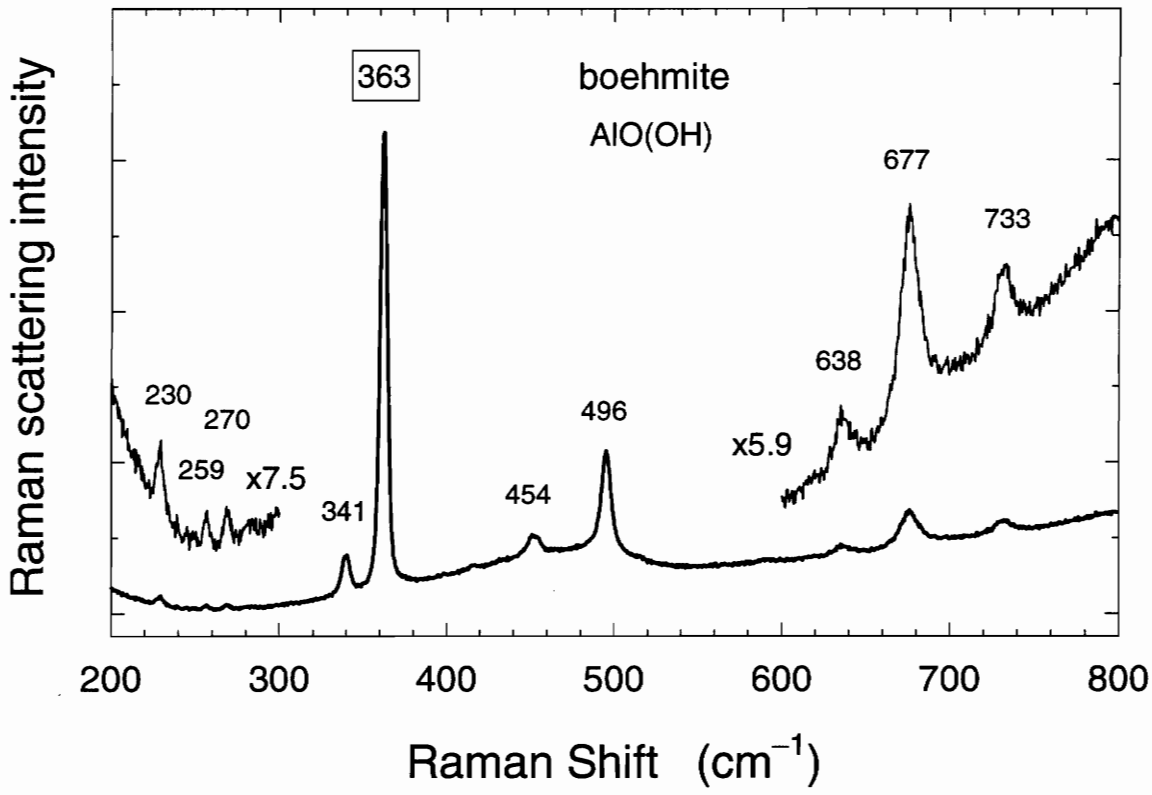

Fig. 3.3: The Raman spectrum of crystalline boehmite in the Al-O regime. Scattered light intensity is shown plotted against photon-energy downshift, in wavenumber units, relative to the laser line (the 488.0 nm line, for this case).

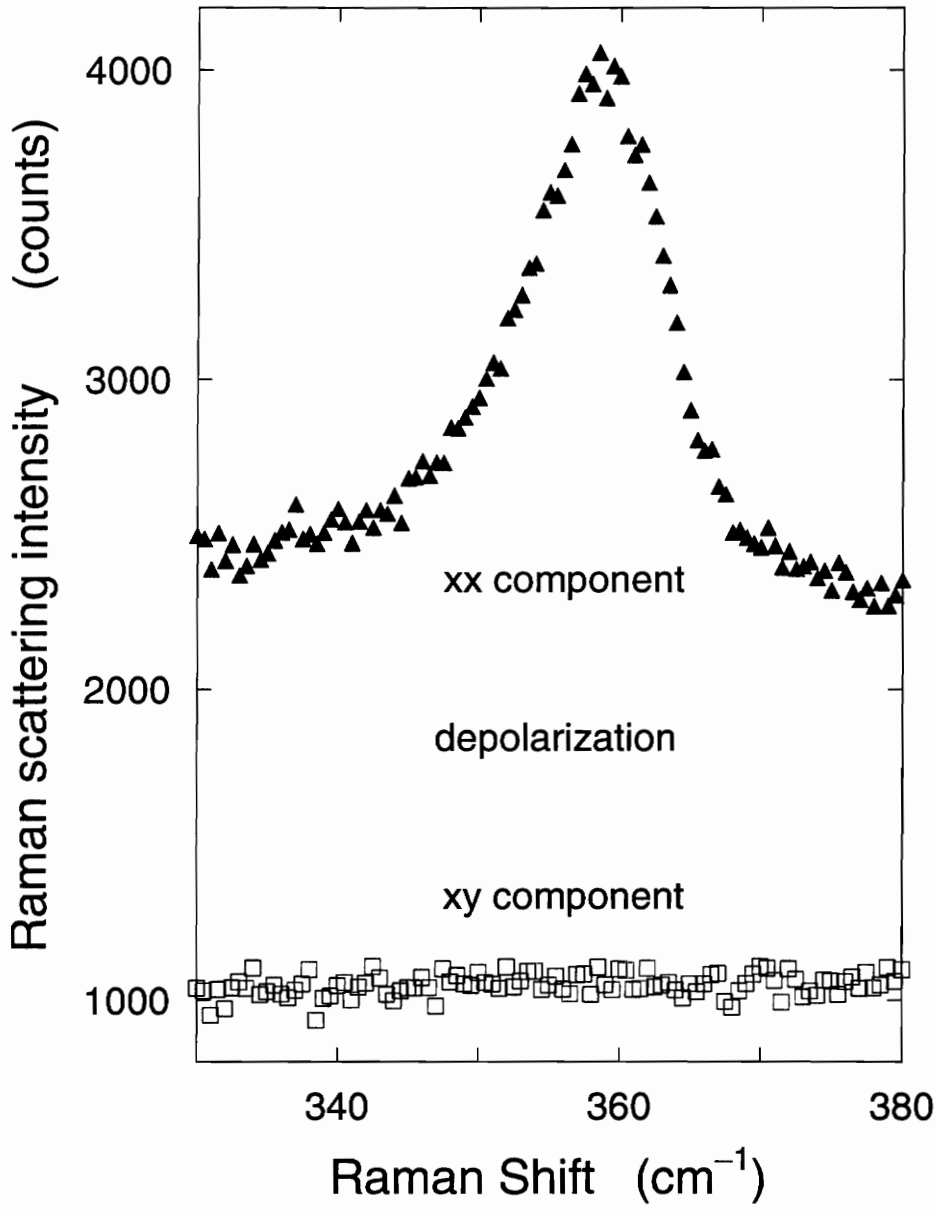

Fig. 3.4: The polarization dependence of the 363 cm^{-1} line for boehmite. (For this nanocrystalline sample, the line is downshifted to 359 cm^{-1}.) These spectra (obtained with 514.5 nm excitation) are for a hydrogel, peptized with HNO_3 (R=0.07) and aged in the sol phase for 48 hours. This clean depolarization behavior supports the fully symmetric A_g assignment for this band.

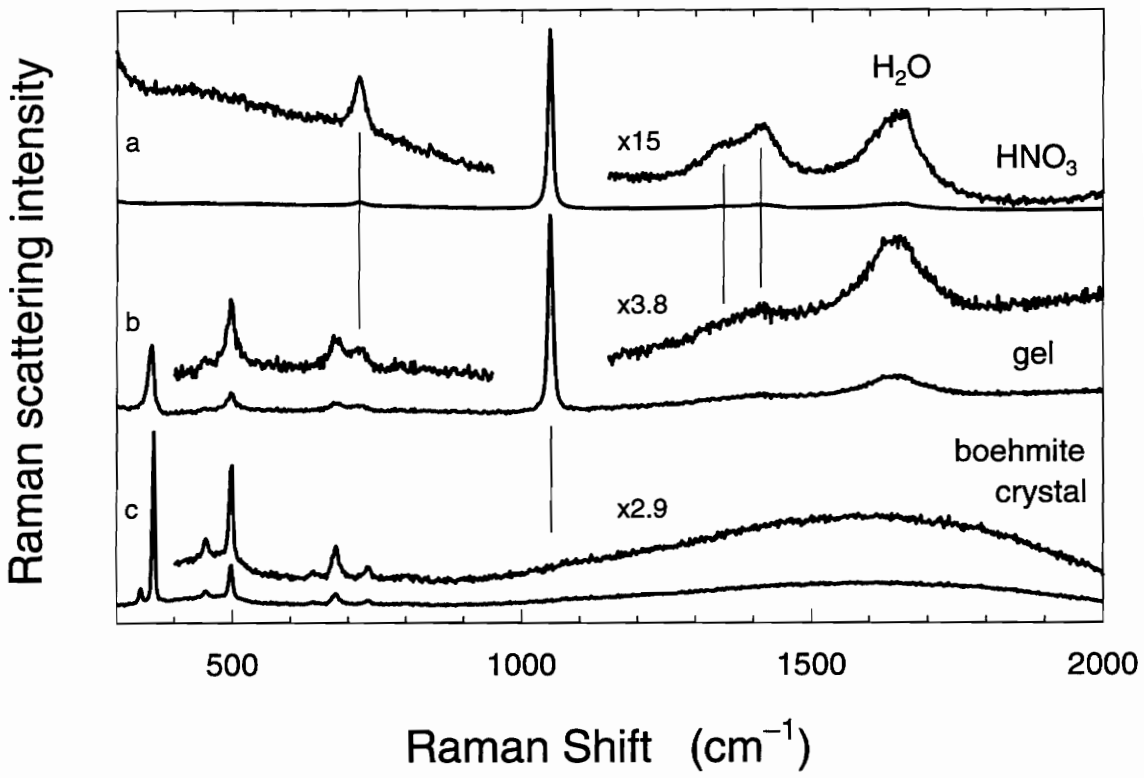

Fig. 3.5: Comparison of the Raman spectra of (a) nitric acid, (b) an alumina hydrogel, and (c) crystalline boehmite. (These spectra, as well as those shown in the following figures, were obtained with 514.5 nm excitation.) The spectrum shown in (a) was obtained for a 0.1 N solution of HNO_3. The spectrum shown in (b) was obtained for a gel prepared using nitric acid in the peptization step (at an HNO_3:ASB molar ratio R of 0.14) and a sol aging time of 48 hours. The four NO_3^- bands marked by vertical lines are seen to be present in the gel spectrum; these nitrate-ion lines have been misinterpreted (as boehmite lines, or as lines due to organic impurities) in some previous studies of sol-gel alumina.

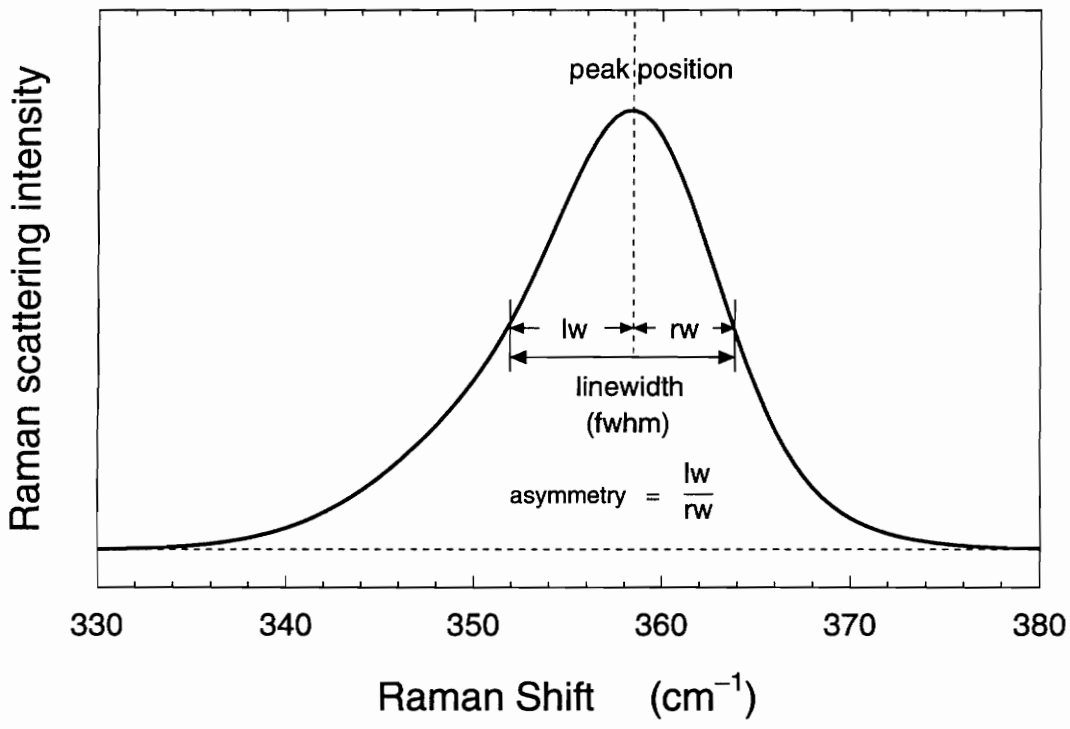

Fig. 3.6: Detailed view of the boehmite-like band in an alumina hydrogel, illustrating the lineshape parameters used in our analysis. The curve is a fit to data obtained for a gel synthesized using HCl peptization (acid:ASB molar ratio R of 0.07) and a t_S of 24 hours. The linewidth indicated here is the experimental linewidth; it is a convolution of the actual linewidth and the instrumental spectral slit width. The linewidth values plotted in Figs. 3.8 and 3.9 correspond to the (deconvoluted) actual linewidth.

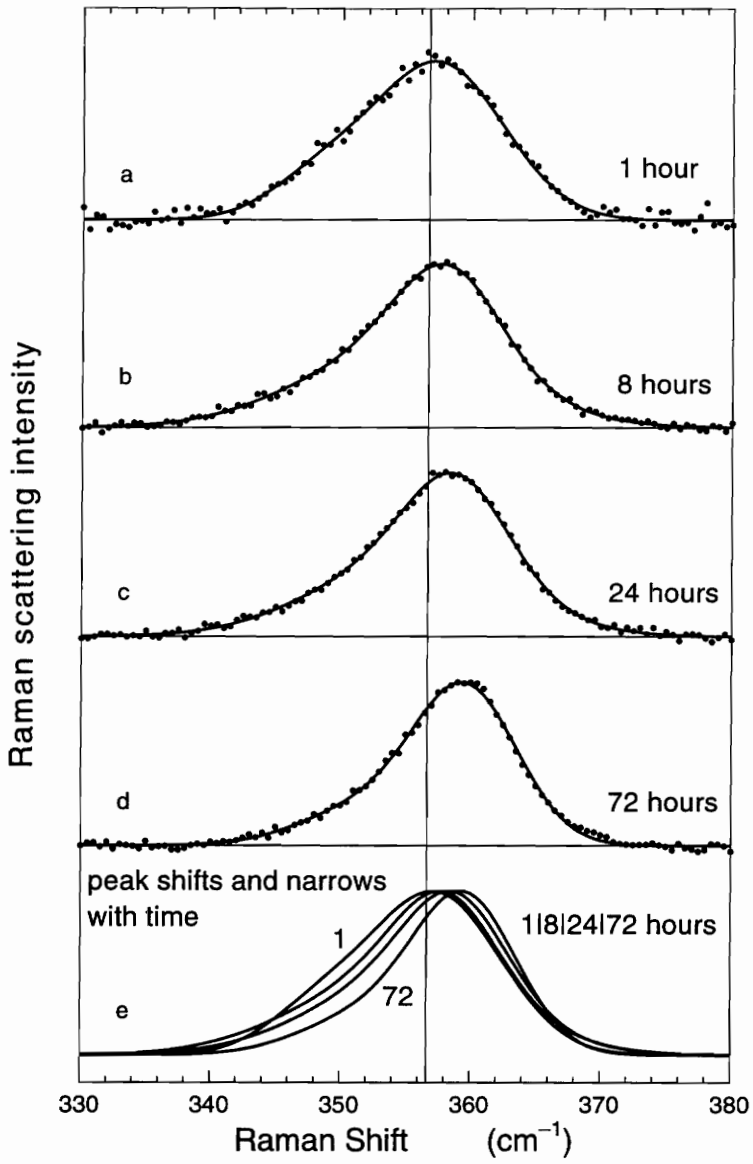

Fig. 3.7: The influence of sol aging time on the position and lineshape of the boehmitelike band seen in the resulting hydrogels. The solid dots in panels a through d are the experimental data; the curves are fits. Panel e shows a superposition of the fitted curves of the top four panels, for t_S values of 1, 8, 24, and 72 hours, in order to more clearly reveal the narrowing and upshifting with increasing t_S. This series of hydrogels was prepared from a sol that had been peptized with HCl (with R=0.07).

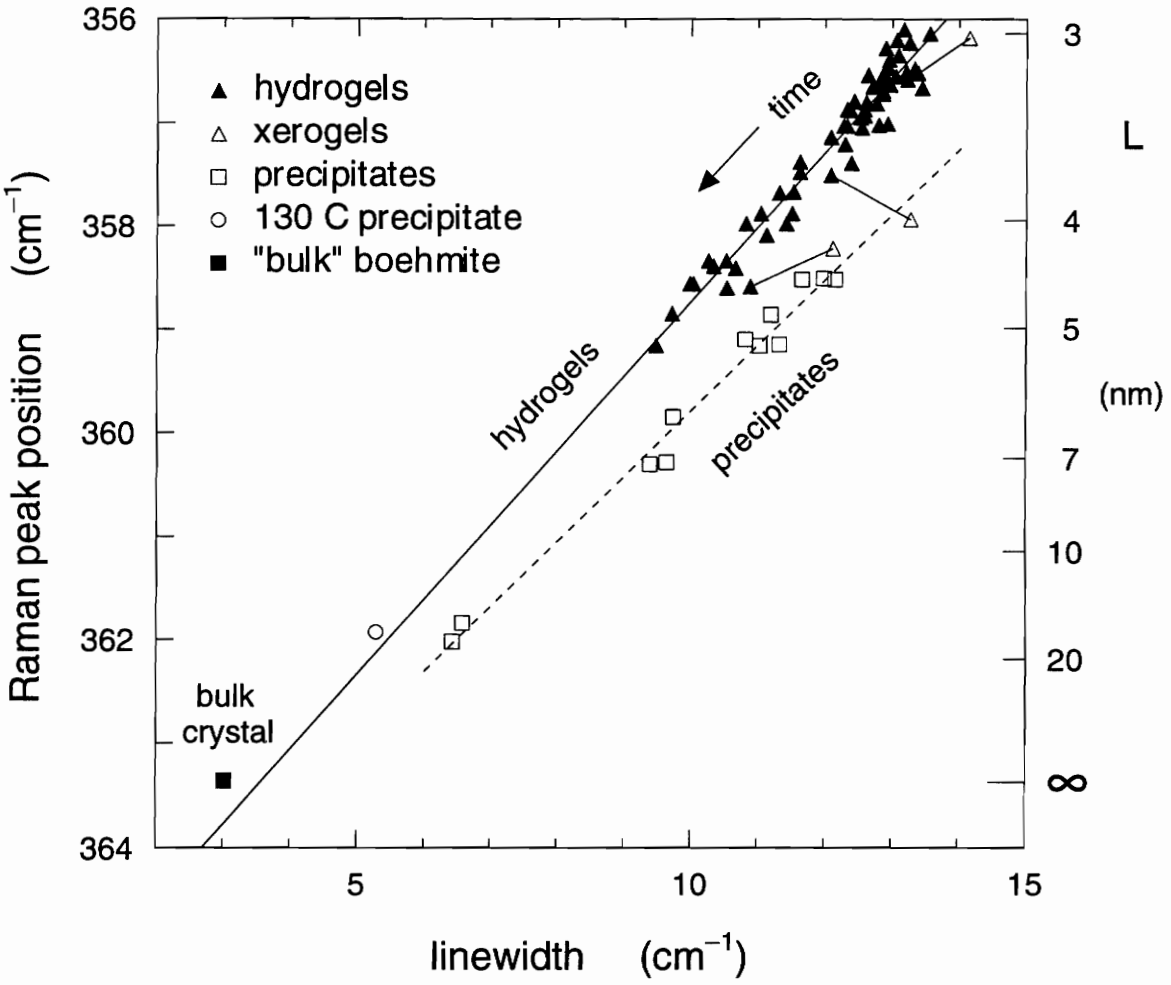

Fig. 3.8: The correlation between peak position and linewidth for the boehmitelike Raman band observed in sol-gel-alumina materials. Seventy samples are represented in this figure, over fifty of these being Yoldas-process hydrogels synthesized using a range of sol aging times. The other samples are described in the text.

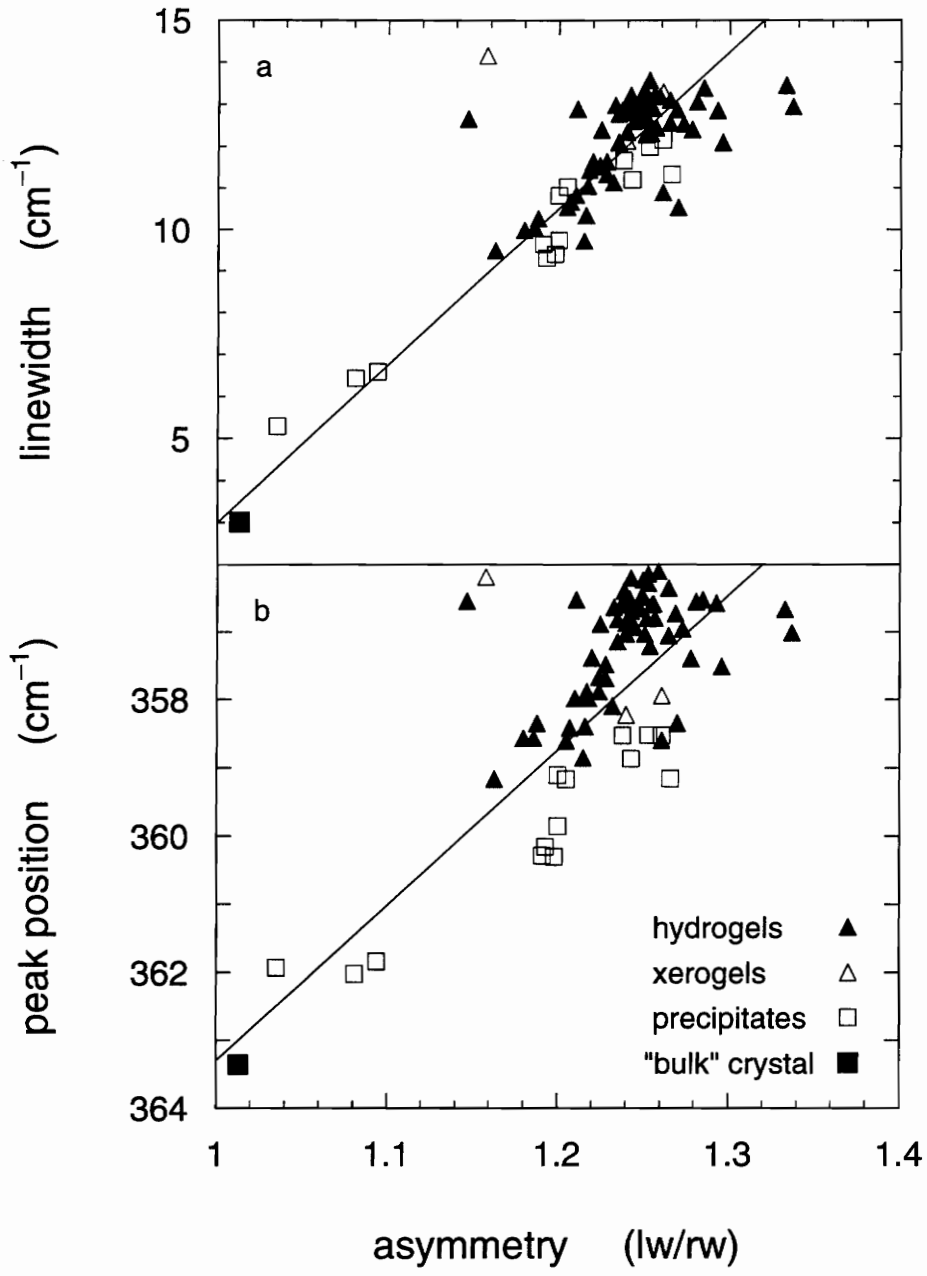

Fig. 3.9: Correlations between the asymmetry of the boehmitelike band lineshape and the position and linewidth of the band, for the samples of Fig. 3.8.

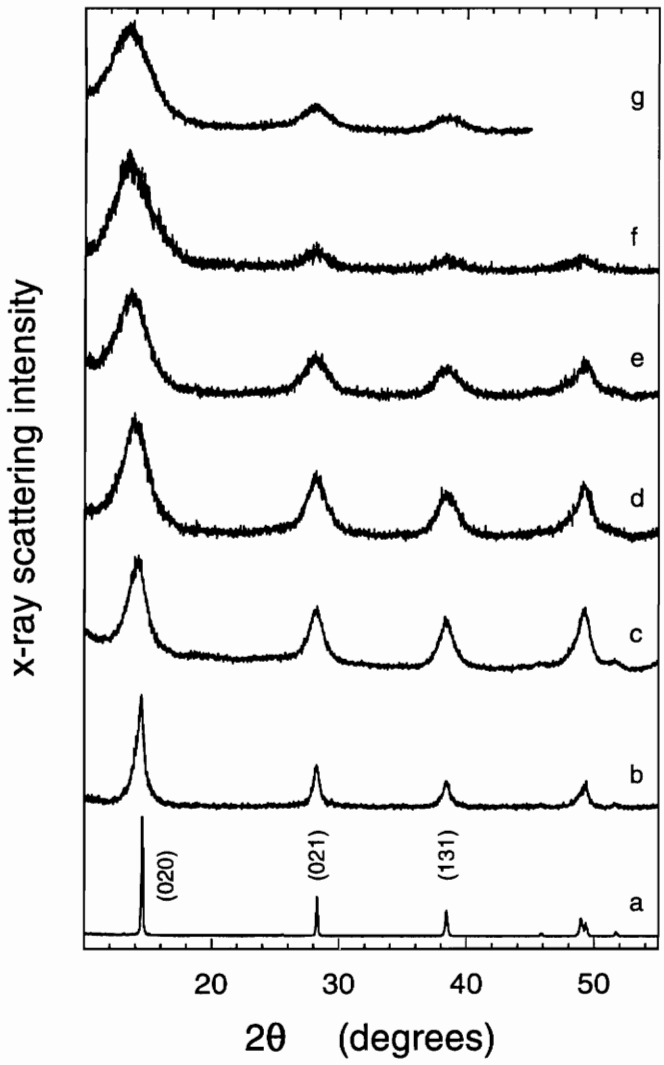

Fig. 3.10: X-ray diffraction data taken on powder samples, using CuKα radiation (1.54 Å wavelength). The very sharp peaks in trace a, obtained with micron-size crystals, are consistent with the calculated diffraction spectrum of bulk crystalline boehmite. The peaks in traces b-g show progressively broader linewidths, indicating progressively smaller crystallite sizes. Crystallite sizes were calculated, using the Scherrer formula (eqn. 1), from the widths of the (021) and (131) peaks. The "bulk crystal" sample corresponding to trace a is represented by a solid square in the Raman data of Figs. 3.8, 3.9, and 3.11. Trace b is the 130 C precipitate described in the text and is represented by an open circle in Figs. 3.8 and 3.11. Traces c-e are 48-hour, 8-hour, and 1-hour precipitates respectively (open squares in Figs. 3.8, 3.9, and 3.11). Trace f is for a 48-hour gel peptized with nitric acid at R=0.07 (solid triangle in Figs 3.8, 3.9, and 3.11). Trace g is for a 1-hour xerogel (open triangle in the upper right hand corner of Figs. 3.8 and 3.11).

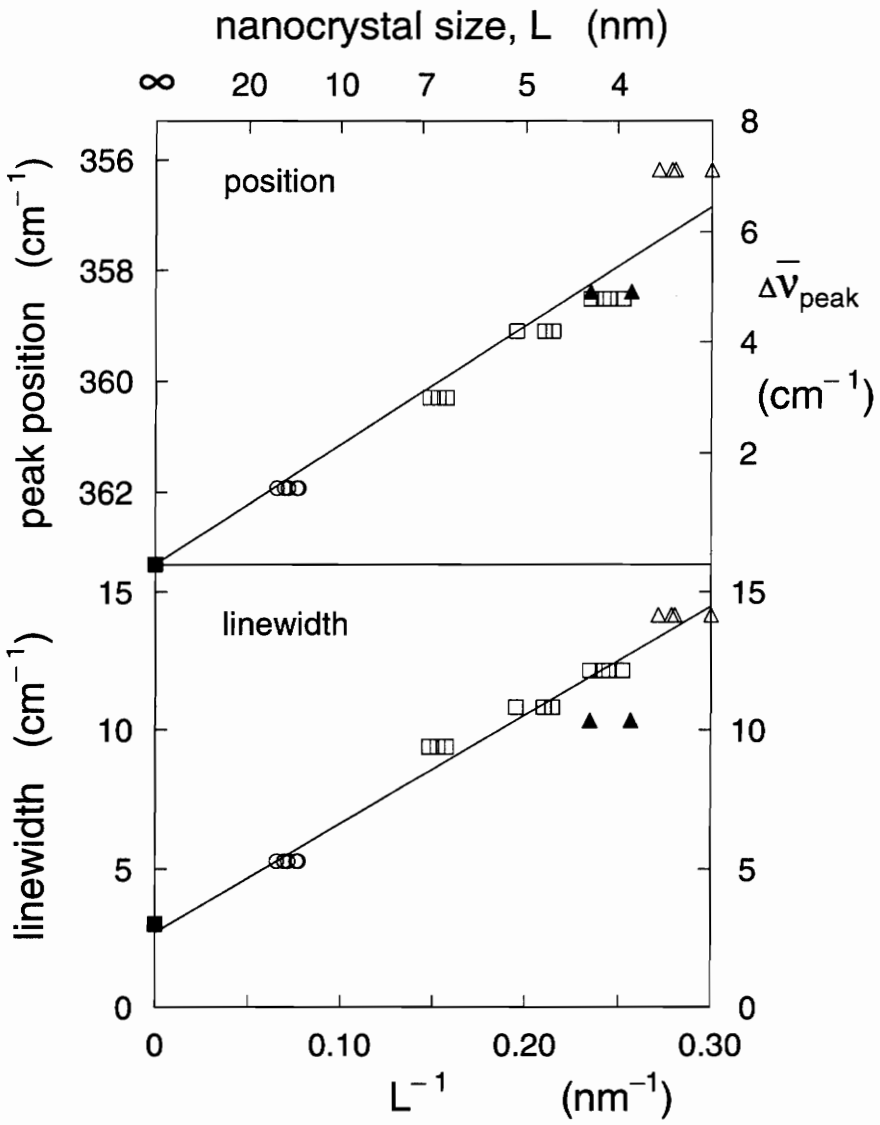

Fig. 3.11: The correlation between the crystallite size (L), as determined by x-ray diffraction for a particular sample, and the Raman peak position and linewidth (of the 360 cm^{-1} band) observed for the same sample. The samples and their corresponding symbols have been described in the caption of Fig. 3.10.

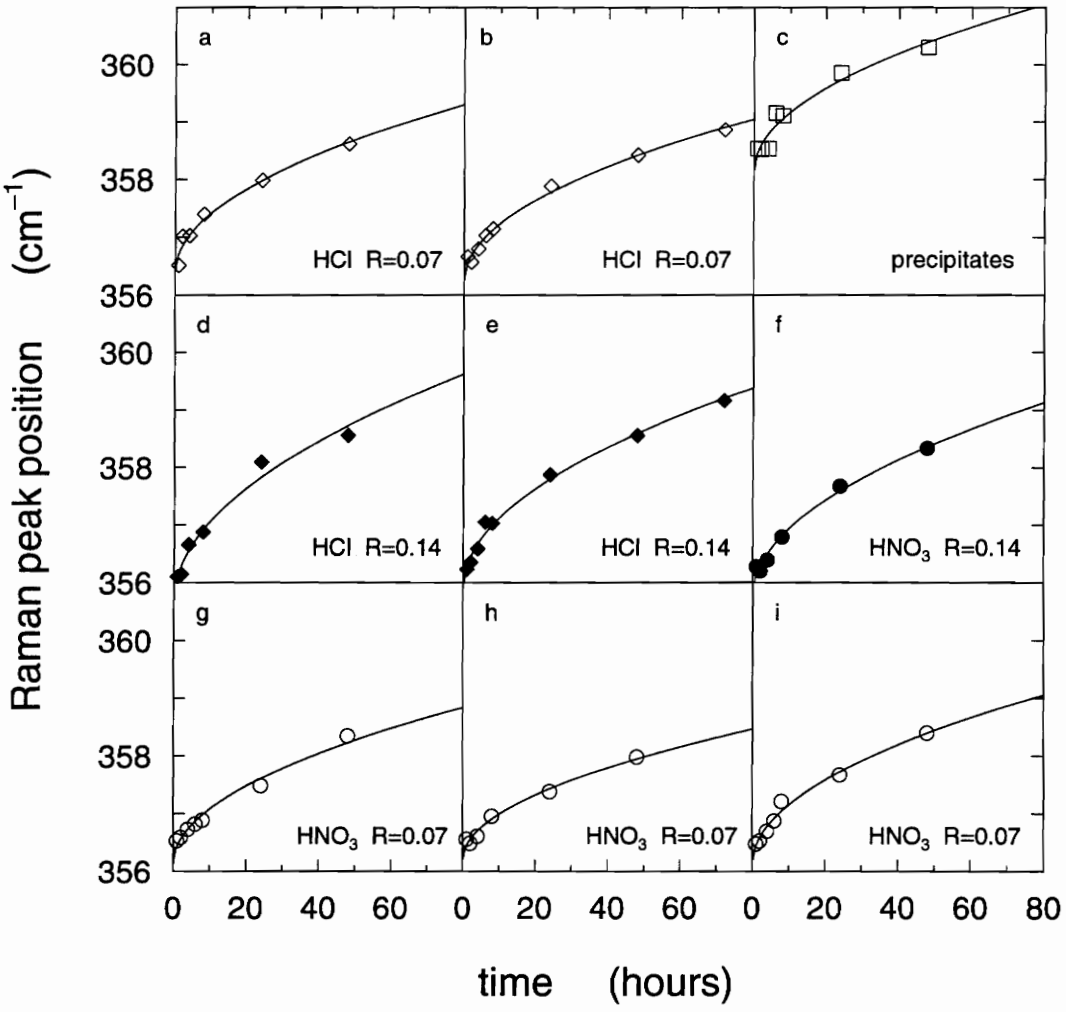

Fig. 3.12: The results of individual runs on the influence of the sol aging time on the Raman peak position of the boehmitelike band in the hydrogel. The acid used in the sol peptization step is indicated in each case, as well as the acid:ASB molar ratio R. One unpeptized example (R=0) is included, in panel c, for comparison. The peak-position scale in this figure is reversed with respect to the scales used in Figs. 3.8 and 3.9b.

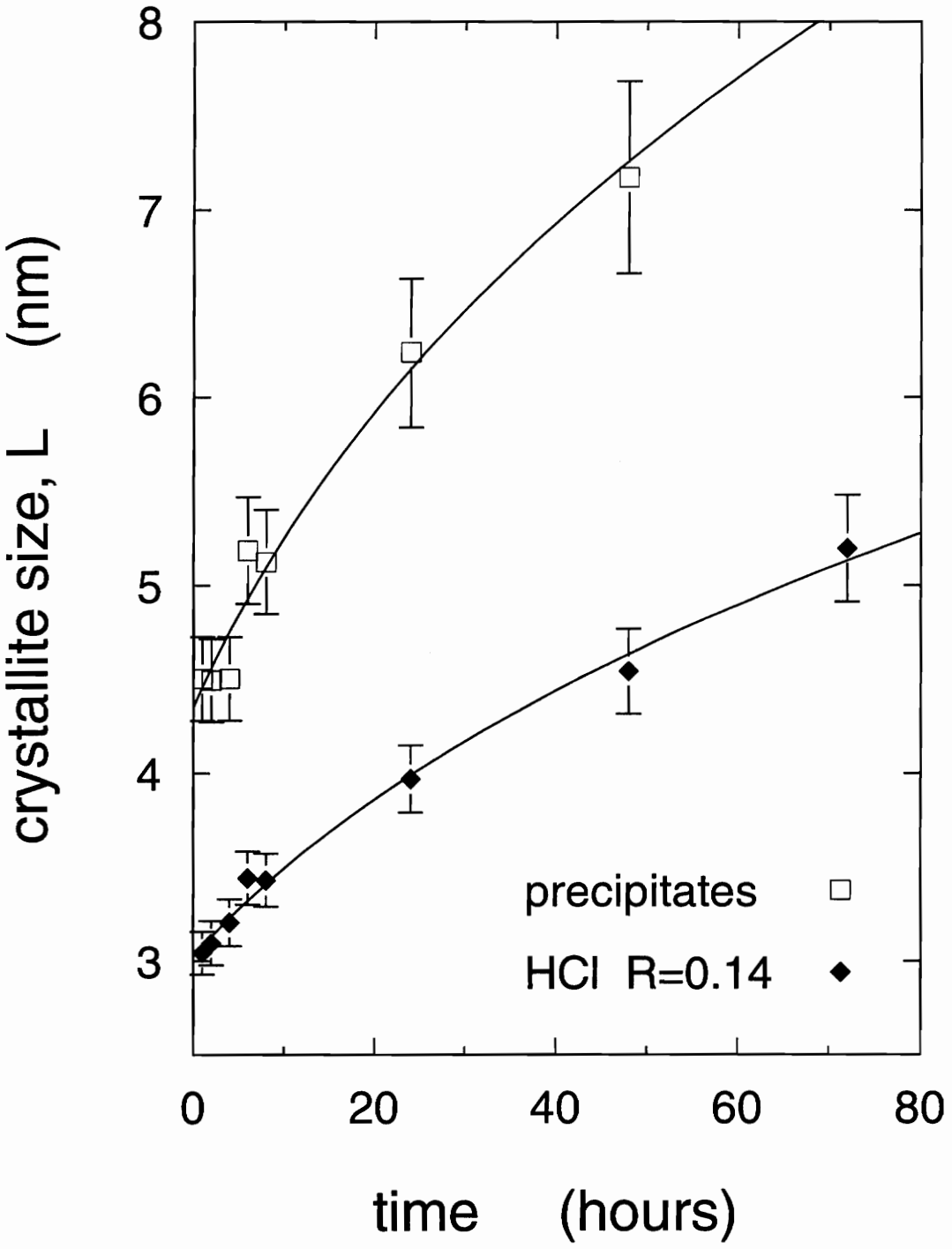

Fig. 3.13: Nanocrystal-size growth kinetics for the runs of Figs. 3.12c and 3.12e, estimated from the Raman and x-ray data by the method described in the text.

---

[1]B. E. Yoldas, Amer. Ceram. Soc. Bull. **54**, 286 (1975).

[2]B. E. Yoldas, Amer. Ceram. Soc. Bull. **54**, 289 (1975).

[3]B. E. Yoldas, J. Mater. Sci. **10**, 1856 (1975).

[4]B. E. Yoldas, J. Appl. Chem. Biotech. **23**, 803 (1973).

[5]C. J. Brinker and G. W. Scherer, Sol-Gel Science, (Academic Press, Boston, 1990), p. 599.

[6]Temperature is an important variable in the Yoldas process. If cool water is used, $Al(OH)_3$ predominates and forms mixed-phase precipitates (see Chapter 4).

[7]Reference 5, p. 371.

[8]Our simple deconvolution is a standard approximation which is strictly correct for Gaussians. A more sophisticated analysis for Lorentzians has been given by J. Gonzalez-Hernandez, G. H. Azarbayejani, R. Tsu, and F. H. Pollak, Appl. Phys. Lett. **47**, 1350 (1985). Since, for most of our samples, Γ_{expt} is substantially greater than Γ_{inst}, the instrumental correction is small and Γ is insensitive to the deconvolution procedure.

[9]A. C. Pierre and D. R. Uhlmann, Better Ceramics Through Chemistry, eds. C. J. Brinker, D. E. Clark, and D. R. Ulrich (Elsevier, North-Holland, New York, 1984), p 119.

[10]B. E. Warren, X-ray Diffraction (Addison-Wesley, Reading, Mass., 1969), p. 253 and p. 258; H. P. Klug and L. E. Alexander, X-ray Diffraction Procedures for Polycrystalline and Amorphous Materials, (John Wiley & Sons, New York, 1973), p. 687 and p. 635.

[11]C. E. Corbato, R. T. Tettenhorst, and G. G. Christoph, Clays and Clay Minerals

33, 71 (1985).

[12]Figure 2 was constructed using the atom positions of Corbato et al. (Ref. 11), with the aid of a crystal-structure graphics program written by M. Bukowinski and R. Downs.

[13]S. P. S. Porto and R. S. Krishnan, J. Chem. Phys. **47**, 1009 (1967).

[14]A. S. Barker, Phys. Rev. **132**, 1474 (1963).

[15]This sample, prepared at Alcoa Laboratories, was made by autoclaving aluminum metal in excess water. X-ray diffraction, performed at NASA Langley, confirmed that the material was well-crystallized boehmite.

[16]A. B. Kiss, G. Keresztury, and L. Farkas, Spectrochim. Acta A **36**, 653 (1980). Peak positions reported in this paper agree well with our results of Table I, with one notable exception (in addition to the NO_3^- modes discussed in the text). Kiss et al. place the dominant line at 369 cm^{-1} instead of 363 cm^{-1}. Since our result was repeatedly checked and is also consistent with the asymptotic limit of the family of gel samples, the 363 cm^{-1} value is the correct one.

[17]G. Mariotto, E. Cazzanelli, G. Carturan, R. Di Maggio, and P. Scardi, J. Solid State Chem. **86**, 263 (1990).

[18]T. Assih, A. Ayral, M. Abenoza, and J. Phalippou, J. Mater. Sci. **23**, 3326 (1988).

[19]D. E. Irish and A. R. Davis, Can. J. Chem. **46**, 943 (1968). D. E. Irish and G. E. Walrafen, J. Chem. Phys. **46**, 378 (1967). D. E. Irish, Ionic Interactions from Dilute Solutions to Fused Salts, edited by S. Petrucci (Academic Press, New York, 1971), p. 187.

[20]P. Scardi, J. Solid State Chem. **86**, 263 (1990).

[21]K. Wefers and C. Misra, Oxides and Hydroxides of Aluminum, Alcoa Technical Paper 19, revised (Alcoa Laboratories, Alcoa Center, 1987).

[22]R. Zallen, The Physics of Amorphous Solids (John Wiley & Sons, New York, 1983).

[23]H. Richter, Z. P. Wang, and L. Ley, Solid State Commun. **39**, 625 (1981).

[24]K. K. Tiong, P. M. Amirtharaj, F. H. Pollak, and D. E. Aspnes, Appl. Phys. Lett. **44**, 122 (1984); M. Holtz, R. Zallen, O. Brafman, and S. Matteson, Phys. Rev. B **37**, 4609 (1988).

[25]I. H. Campbell and P. M. Fauchet, Solid State Commun. **58**, 739 (1986).

[26]R. Zallen, J. Non-Crystalline Solids **141**, 227 (1992).

[27]T. Kanata, H. Murai, and K Kubota, J. Appl. Phys. **61**, 969 (1987).

[28]S. J. Yu, H. Asahi, S. Emura, H. Sumida, S. Gonda, and J Tanoue, J. Appl. Phys. **66**, 856 (1989).

[29]K. Nakamura, M. Fujitsuka, and M. Kitajima, Phys. Rev. B **41**, 12260 (1990).

[30]R. J. Nemanich, S. A. Solin, and R. M. Martin, Phys. Rev. B **23**, 6348 (1981).

[31]G. G. Christoph, C. E. Corbato, D. A. Hofmann, and R. T. Tettenhorst, Clays and Clay Minerals **27**, 81 (1979).

[32]Z. Iqbal and S. Veprek, J. Phys. C **15**, 377 (1982).

[33]M. Gargouri, B. Prevot, and C. Schwab, J. Appl. Phys. **62**, 3902 (1987).

[34]It is provocative that, for the cases examined, α is about equal to d/2, where d is the network dimensionality (e.g., 2 for graphite, 3 for silicon; see p. 89 of Ref. 22).

[35]I. M. Lifshitz and V. V. Slyozov, J. Phys. Chem. Solids **19**, 35 (1961), C. Wagner, Z. Elektrochem. **65,** 581 (1961), W. W. Mullins, J. Appl. Phys. **59**, 1341 (1986); N. Rivier, in Finite Systems: From Clusters to Crystals, edited by P. Jena, S. N. Khanna, and B. K. Rao (Kluwer, Dordrecht, 1992), p.189; P. W. Voorhees and M. E. Glicksman, Metall. Trans. A **15A**, 1081 (1984).

[36]A simple argument for the "parabolic law" is available for growth that is driven by crystallite curvature: growth rate $(d/dt)L^3$ is proportional to surface area (L^2) and to curvature (1/L), so that L(dL/dt) is constant and L^2 increases linearly with time.

CHAPTER FOUR

$Al(OH)_3$ CRYSTAL NUCLEATION AND GROWTH

4.1 Introduction

The Yoldas[1] process for making sol-gel alumina (see the previous chapter) proceeds by hydrolyzing aluminum secondary-butoxide (ASB) at temperatures at or above 80 C, followed by an acid peptization step. In this chapter, the crystal phases that are produced by the hydrolysis of ASB at temperatures less than 80 C, with no acid peptization, are analyzed. Three additional crystalline aluminum hydroxide [$Al(OH)_3$] polymorphs, bayerite, gibbsite, and nordstrandite, are produced,[2,3,4] in addition to the "high temperature" oxy-hydroxide [AlO(OH)] boehmite phase. Several materials processing parameters were varied in order to gain a consistent understanding of this deceptively simple system. In particular, the variation of reaction time, temperature, and the method of hydrolysis yields information about the nucleation and growth kinetics of the $Al(OH)_3$ hydroxide phases. I have found that Raman scattering can effectively detect all of the crystal phases present at early reaction times. This approach thus yields a quantitative analysis of the relative phase mix in this system, as a function of the materials processing parameters.

Crystal nucleation and crystal growth occur on two separate time scales for this system. Nucleation occurs at the earliest processing times, and is over in a time on the order of seconds. We have probed the nucleation process by using different initial water temperatures and methods of hydrolysis. Crystal growth occurs on time scales of the order of hours to several days, and was monitored as a

function of time and processing temperature. At very early reaction times, two fundamental chemical reactions take place; the classical sol-gel reactions of hydrolysis and condensation. These processes proceed very rapidly for this system (in times on the order of a few seconds), and we will find that the relative concentration of the $Al(OH)_3$ nuclei is determined by the hydrolysis conditions at the early processing times. Crystal growth proceeds by the reaction

$$AlO(OH) \Rightarrow solution \Rightarrow Al(OH)_3,$$

where the $Al(OH)_3$ crystal phases are growing on the initially formed $Al(OH)_3$ nuclei. All of the $Al(OH)_3$ phases grow at the same rate, which is strongly effected by temperature. The higher the temperature, the slower the crystal growth.

These materials have been difficult to study because the crystals formed are very small, particularly for bayerite and nordstrandite. In addition, their polymorphic nature, which have similar structural units, makes it difficult to produce pure single phase materials. The Raman spectra for these materials are not fully understood. Subtle but significant reinterpretations of the spectra, with respect to Raman combination band assignments, have been made.

Section 4.3 is an introduction to the crystal structures and Raman spectra of these materials. Sections 4.4, 4.5, and 4.6 cover the basic results that lead to an understanding of the crystal nucleation kinetics and the relative phase mix as a function of temperature. Crystal growth kinetics are discussed in Section 4.7, and section 4.8 gives additional supporting x-ray and infrared (IR) data. Section 4.9 summarizes the principal findings.

4.2 Experimental

Figure 4.1 is a flowchart of the materials synthesis process; details of this process, and of the Raman scattering and IR measurements, can be found in chapter two. The x-ray data was taken by Milton Ferguson of Norfolk State University.

4.3 Crystalline Nordstrandite, Bayerite, and Gibbsite, and Mixed-Crystal Phases

Nordstrandite, bayerite, and gibbsite, all $Al(OH)_3$ polymorphs, are structurally very similar. They are layered compounds, and the crystal phases are determined by the way the layers are stacked. Accordingly, the Raman spectra of these materials are very similar and they also have many peaks (15 to 20 peaks for each crystal phase). In this section, the basic crystal structural and Raman spectral features for these materials are discussed, particularly as they relate to crystal phase identification. A group-theoretical analysis of the vibrational IR and Raman spectra of these materials has not been performed, largely because there seem to be too many Raman peaks in the observed spectra. An interpretation of some of these peaks in terms of combination bands will be presented here, this helps to clarify the picture.

A synopsis of the structural aspects of the three $Al(OH)_3$ polymorphs, derived from "Oxides and Hydroxides of Aluminum",[5] follows. The basic structural unit is a hexagon. At each vertex of this hexagon is an AlO_6 octahedral unit. A layer is composed of these hexagons linked as in a hexagonal honeycomb. This layer is the fundamental unit. The way that these layers are stacked determines the resulting $Al(OH)_3$ phase, as shown in Fig. 4.2. Each layer has a

sandwich structure with a plane of aluminum ions enclosed by two planes of hydroxyl ions (labeled A and B in Fig. 4.2) that are shifted from each other along the layer. Within A and B, the hydroxyl ions form a triangular lattice (two-dimensional close packing). Bayerite has an -AB-AB-AB- packing, so that the c-axis repeat contains only one layer. Gibbsite has an -AB-BA-AB-BA- structure, so that the c-axis repeat contains two layers. In nordstrandite, two layers with a gibbsitelike sequence alternate with two layers having a bayeritelike sequence.[6] The c-axis repeat contains four layers for nordstrandite, which is the most structurally complex of the three polymorphs. Table 4.1 gives the structural parameters for bayerite, nordstrandite, and gibbsite.

Figure 4.3 is a Raman spectrum of a sol processed at 25 C for 48 hours. This material is about 60% bayerite and 40% microcrystalline boehmite [AlO(OH)]; the percentages, 60 and 40%, are based on weight loss measurements (see section 4.7). The boehmite phase shows up in all of the materials that we made. The most prominent Raman features of boehmite are bands at 360 and 496 cm^{-1}. The peaks in Fig. 4.3, less the boehmite bands, are due primarily to bayerite, and they can be broken down into three spectral regions: crystal, combination, and hydrogen regions. The peaks in the region below 600 cm^{-1} are assigned to crystal lattice fundamentals; these vibrations correspond to covalently bonded Al-O normal modes of the crystal. The strongest band in this region, at 545 cm^{-1}, is due to bayerite, and its intensity will be used, along with that of the 360 cm^{-1} boehmite band, for kinetic studies of bayerite crystal growth. The peaks in this region are not very useful for the determination of relative concentrations among the $Al(OH)_3$ phases, because they tend to overlap in mixed-phase systems.

Table 4.1 The structural properties for the $Al(OH)_3$ polymorphs, bayerite, nordstrandite, and gibbsite.[5]

phase	crystal system	space group	molecules per cell	unit axis length, nm a	b	c
bayerite	monoclinic	$P2_1/c$, C_{2h}^5	2	0.5062	0.8671	0.4713
nordstrandite	triclinic	P1, C_1^1	2	0.5114	0.5082	0.5127
gibbsite	monoclinic	$P2_1/c$, C_{2h}^5	4	0.8684	0.5078	0.9136

Table 4.2: Raman peak positions for the 25 C sample of Fig. 4.3.

Bayerite peaks (cm^{-1})	Combination frequencies (cm^{-1})
106	
240	
251	
298	
324	
359 (boehmite)	
389	
436	
525	
546	
730	298+324=722
771	388+388=776
818	436+389=825
868	546+324=870
	436+436=872
902	525+389=914
985	436+546=982
1008	525+389+106=1018

Table 4.3: The $Al(OH)_3$-polymorph origin of Raman lines seen in the dried precipitates. This table is compiled from Rodgers,[8] and Fig. 4.13c. Most peaks have three parents (all three $Al(OH)_3$ polymorphs), some have two, some have a single parent.

Fig. 4.13c	Bayerite	Nordstrandite	Gibbsite	notes
107	108			
120	118	116	115	
	140			
180			178	
	208			
228				
239	241	237	242	
251	250	252	255	
265				
285		282		
304	299	303	307	
314				
324	325		321	
360				boehmite
378		377	380	
389	393	386	396	
411			412	
			429	
436	437	437		
444	441	441	445	
496				boehmite
506			507	
541	546	541	539	
			568	double unit cell
598		588	600	

A second group of bayerite peaks lie between 600 cm^{-1} and 1100 cm^{-1}. Because of their relatively weak intensities (see Fig. 4.3) with respect to the lattice modes, and because their frequencies can be written as the sum of two or more lattice frequencies, they are interpreted here as combination bands. Table 4.2 lists the peak positions for the spectrum of Fig. 4.3. For the combination bands, it gives possible assignments as sums of lattice frequencies. The peaks in the combination region are broad and weak, and are not useful for the identification of the crystal phases. They appear to be influenced by lattice strain, because their relative intensities are not always consistent, and because the best crystal samples show a reduced intensity [see Fig. 4.4(c)].

The hydrogen bands in Fig. 4.3 lie between 3000 cm^{-1} and 3800 cm^{-1}. These bands correspond to O–H stretching modes, and are very intense. (We do not see peaks in the region between 2800 cm^{-1} and 3000 cm^{-1}, which would correspond to C–H stretching modes.) The three strongest peaks in this region correspond to bayerite, while the two weak bands at 3079 cm^{-1} and 3219 cm^{-1}, which show up as two small humps, are due to boehmite. The other peaks are caused by the presence of gibbsite and nordstrandite. The peaks in this region are useful for the identification and determination of the relative concentrations of the $Al(OH)_3$ polymorphs.

Figure 4.4 shows a detailed comparison of the Raman spectra of the crystalline $Al(OH)_3$ polymorphs, bayerite, nordstrandite, and gibbsite reported by Rodgers et. al. Table 4.3 is the corresponding peak-position table. The spectra are similar in their peak positions and relative intensities. The strongest peaks are at about 310 and 550 cm^{-1}. Gibbsite [Fig. 4.4(a)] can be identified by the doublet at 539 and 568 cm^{-1}; this doublet may be caused by its unit cell size, which is twice

as big as it is for bayerite and nordstrandite (see Table 4.1). Mixed phases of bayerite and nordstrandite, our primary interest, can be discerned by the presence of the 299 cm^{-1} line of bayerite [Fig. 4.4(b)] and the 303 cm^{-1} line of nordstrandite [Fig. 4.4(c)]; these lines produce an apparent doublet in mixed phases. Also included in Table 4.3 is a peak listing for the Raman spectrum shown in Fig. 4.13(c); this material is primarily nordstrandite, but it does contain some bayerite and a considerable amount of boehmite. It is interesting that there are a few peaks that cannot be explained by any of the three $Al(OH)_3$ polymorphs or boehmite, it may be that lattice strain has altered the selection rules for Raman scattering and that the presence of these additional lines should not be interpreted, at this time, as indicating the presence of a separate or new phase.

Figures 4.5[7] and 4.6[8] show the hydrogen (O-H stretching) region for the $Al(OH)_3$ polymorphs. The lines in this region do not generally overlap, except for the 3615 and 3618 cm^{-1} lines of gibbsite [Fig. 4.5(a)] and nordstrandite (Fig. 4.6), respectively. These lines are therefore useful for crystal phase identification and for understanding the relative phase mix. The essential features of the Raman spectra, and the crystalline structures, for the $Al(OH)_3$ phases have now been reviewed. The following sections discuss how the processing conditions effect the crystal phase mix.

4.4 Nordstrandite:bayerite:gibbsite phase mix does not change with time

One of the basic results of this chapter is that the $Al(OH)_3$ phase mix does not change with time. This observation, and the observations to be described in sections 4.5 and 4.6, will show that the $Al(OH)_3$ phase mix is determined largely by the initial rate of hydrolysis of the ASB, which strongly influences the crystal

nucleation kinetics. The results of this section show that the phase mix does not change for times greater than about one hour. This is a very convenient result, because time (beyond one hour) is then no longer a significant parameter, and samples prepared by different processing methods can then be compared without reference to time. Another interesting and important consequence, of the constant phase mix result, is that the growth rate of each of the $Al(OH)_3$ phases are identical (section 4.7 discusses the bayerite growth kinetics).

Figure 4.7 shows Raman spectra, in the hydrogen (O-H stretching) region, of materials that were processed at 25 C for 4, 24, and 96 hours. The spectra in this figure are essentially identical. This implies a constant nordstrandite:bayerite:gibbsite phase mix, because all of the $Al(OH)_3$ crystal forms have identifiable spectral features in this region. For the materials of Fig. 4.7, bayerite is the predominant phase, as the three strongest bands, at 3421, 3543 and 3654 cm^{-1} correspond to bayerite. The presence of gibbsite and nordstrandite are indicated by the gibbsite peaks at 3363 and 3620 cm^{-1}, and the nordstrandite peaks at 3564, and 3620 cm^{-1} (gibbsite and nordstrandite share the 3620 cm^{-1} peak frequency). X-ray and IR studies (Section 4.8) confirm that bayerite is the predominant phase in this system (ASB hydrolyzed at 25 C), and it is also generally accepted in the literature.[9]

Figure 4.8 shows Raman spectra, in the hydrogen region, of materials that were processed at 40 C for 24, 48, 72, and 96 hours. The spectra in this figure are essentially identical, which again implies a constant nordstrandite:bayerite:gibbsite phase mix. This same result applies to samples prepared at 60 C. Thus, regardless of processing temperature, the $Al(OH)_3$ phase mix is fixed for times later than about 1 hour (there is no reason to suspect that the phase mix changes before

one hour either). Comparing the 25 C materials of Fig. 4.7 to the 40 C materials of Fig. 4.8, we find that the relative peak heights have changed, and this is the subject of the next section.

4.5 Nordstrandite:bayerite:gibbsite phase mix changes with temperature

With the elimination of time as a structure-determining parameter, at least with respect to the crystalline $Al(OH)_3$ phase mix in the dried powder, we can now readily address the effect of temperature. We will find that the nordstrandite:bayerite ratio increases with increasing temperature in a nearly linear fashion, and that the gibbsite:bayerite ratio decreases with temperature. In addition, several previously unobserved or unexplained bands will be discussed. It is important to recall from the experimental section (section 4.2) that, in addition to higher aging temperatures, materials processing at higher temperatures also means that the initial hydrolysis of the ASB occurs at a corresponding higher temperature. The effect of the hydrolysis temperature on the crystal phase mix will be discussed in the next section; here we will discuss the convoluted effect of temperature with respect to both hydrolysis and aging. Low-frequency Raman spectra are included in this section.

Figure 4.9 shows Raman spectra, in the hydrogen region, for materials processed at 25, 40, and 60 C. Panel (a) gives the Raman spectrum for the 25 C material and all of the observed peaks are labeled by their peak frequency. Panel (b) labels the observed peaks by the following system: bayerite, nordstrandite, and gibbsite peaks are labeled as b, n, and g respectively; dark letters above peaks indicates that those peaks are widely accepted in the literature as being associated with that particular phase (e.g. the dark letter b above the 3421 cm^{-1} peak indicates that peak is normally associated with the bayerite

phase), peaks labeled by gray scale numbering have not been previously associated with the indicated phases and may not have been previously observed. This system of labeling will be used throughout this chapter.

The relative intensity (Fig. 4.9) of the nordstrandite bands (3489, 3564, and 3620 cm^{-1}), with respect to the bayerite bands (3421, 3543, and 3654 cm^{-1}), increases as a function of temperature [panels (a)-(c)]; this indicates that the relative concentration of nordstrandite, with respect to bayerite, increases with temperature. Since nordstrandite and gibbsite share the 3620 cm^{-1} band, this is indicated in panel (b) by labeling this peak with both an n and a g; this peak should not be used for determining the relative concentration of either nordstrandite of gibbsite, but may be used for the sum of the two phases. The analysis of the gibbsite bands (3363, 3431, 3524, and 3620 cm^{-1}) are not straightforward. The 3620 cm^{-1} band is shared with nordstrandite, and the 3431 cm^{-1} gibbsite band of Fig. 4.5(a) is not observed in Fig. 4.9; it may be hidden by the wings of the strong 3421 and 3438 cm^{-1} bands. This leaves the 3363 and 3524 cm^{-1} bands. The 25 C and 40 C materials [panels (a) and (b)] have these bands, but the 60 C material shows only the 3524 cm^{-1} band. In addition the relative intensity (relative to the 3421 cm^{-1} bayerite band) of the 3524 cm^{-1} band increases in the 60 C material with respect to the 40 C material. This suggests that the intensities of the 3363 and 3524 cm^{-1} bands are not always correlated, as they should be if they described the same phase. Therefore the 3524 cm^{-1} band is ascribed to the nordstrandite phase, and not the gibbsite phase, in the higher temperature materials.

The spectra in Fig. 4.9 are very complicated because of the many overlapping peaks. In addition, there are more peaks than expected. The hydrogen

spectrum of bayerite, in Fig. 4.5(b), contains only three peaks (at 3421, 3542, and 3651 cm^{-1}); in Fig. 4.9(b), there are three additional peaks indicated for bayerite (at 3451, 3472, and 3551 cm^{-1}). Likewise, the nordstrandite hydrogen spectrum (Fig. 4.6) has three peaks (at 3487, 3563, and 3618 cm^{-1}), and Fig. 4.9(b) shows three additional peaks indicated for nordstrandite (at 3346, 3398, and 3524 cm^{-1}). The crystal assignments, for the extra peaks, are based upon the analysis in the following paragraph. The cause of the extra Raman bands is unknown, but a possible source is either lattice strain or stacking faults in these layered materials [which can break down the selection rules for Raman scattering, and allow non-Raman-active modes to be observed].

The results of Fig. 4.9 have been made more quantitative in Fig. 4.10. In Fig. 4.10, the relative peak intensity of the Raman bands of Fig. 4.9 are plotted as a function of temperature. This was accomplished by a curve fitting procedure which assumes lorentzian peak shapes, the area of each of the Raman bands was then calculated from the fit parameters. The relative intensity of each peak was determined by dividing its peak area by the area of the strong 3421 cm^{-1} bayerite band. All peaks, in Fig. 4.10, that gave a constant relative intensity with respect to temperature (i.e., that scale with the strong bayerite band), were assigned to bayerite. The other peaks, that gave a nearly linear increase in intensity with temperature were assigned to nordstrandite. A single exception is the case of the weak 3551 cm^{-1} band, which always rides on the wing of the strong 3543 cm^{-1} bayerite band. The relative structure of the 3543 and 3551 cm^{-1} bands did not vary over the 25 to 60 C temperature range, and thus the 3551 cm^{-1} band is also ascribed to bayerite. These peak assignments are further supported by the data shown in Fig. 4.12 of the next section.

For completeness, Figure 4.11 shows the low frequency Raman spectrum for the materials whose high frequency spectrum is shown in Fig. 4.9. The peak labeled by n indicates the presence of nordstrandite (Fig. 4.13, in the next section, is more convincing in this regard). The peaks labeled by B are due to the presence of boehmite. The presence of the boehmite peaks, and their varying relative intensities, tends to clutter up the spectra in this region; but they are useful, particularly the 360 cm^{-1} peak, for $Al(OH)_3$ crystal growth studies (see section 4.7).

4.6 Nordstrandite:bayerite phase mix changes with hydrolysis method: Nucleation effects

So far we have seen that the nordstrandite:bayerite phase mix does not change with time and that the nordstrandite:bayerite phase mix increases linearly with temperature. In this section, the effect of a third variable (additional to time and temperature) will be discussed, the method of hydrolysis of the ASB. The previous section, which examined the effect of temperature on the nordstrandite:bayerite phase mix, indicates that a thermodynamic factor controls the ratio of these two crystal phases. In this section, we will show that the primary controlling factor is actually the crystal nucleation kinetics. Furthermore, the rate of hydrolysis of the ASB is very fast, under any conditions. It will be shown that this implies that the crystal phase mix is determined in the brief hydrolysis step.

Figure 4.12 is similar to Fig. 4.9; it shows the hydrogen-region Raman spectra of materials processed at 25, 40, and 60 C. However, while the materials of Fig. 4.9 were made by adding the water to the ASB, the materials of Fig. 4.12 were made by adding the ASB to the water via a syringe injection. Hydrolysis by

both procedures is very fast, being completed within a few seconds, but it is expected that the rate of hydrolysis is faster by the ASB-to-water syringe method of Fig 4.12.

Just as in the case of Fig. 4.9 (discussed in section 4.5), the nordstrandite:bayerite ratio increases with temperature. This is seen by examining the relative intensity of the 3657 cm^{-1} bayerite band with the 3564 cm^{-1} nordstrandite band. When Fig. 4.12 is compared with Fig. 4.9, we find that each material of Fig. 4.12 has a higher nordstrandite:bayerite ratio than the corresponding (processed at same temperature) material of Fig. 4.9. This difference, between the two sets of materials, must be attributed to the rate of hydrolysis. The faster the rate of hydrolysis, the larger the nordstrandite:bayerite ratio. This, now, also accounts for the effect of temperature on the phase-mix ratio. The higher the temperature, the faster the hydrolysis rate and, consequently, the larger the nordstrandite:bayerite ratio.

The Raman spectra shown in Fig. 4.13 are the corresponding low-frequency (lattice) spectra for the materials whose high-frequency (hydrogen region) spectra are shown in Fig. 4.12. The peaks near 300 cm^{-1} show that nordstrandite is the predominant phase in the 60 C material of Figure 4.13(c). Table 4.3 lists the peak frequencies for the 60 C material and reveals that all of the nordstrandite peaks are present. There are also some unexplained bands, in addition to the bands caused by the presence of boehmite, that cannot be directly associated with any of the $Al(OH)_3$ phases. Again, the breakdown of the Raman scattering selection rules, because of lattice strain or stacking faults, is a possible cause for the extra peaks.

4.7 Bayerite Growth Kinetics

In the previous sections, we saw that the relative concentration of the $Al(OH)_3$ phases were determined by the temperature and the method of hydrolysis. These parameters of the synthesis determined the initial nuclei formed and the nucleation kinetics. In this section, we report results of monitoring the growth kinetics of the nucleated $Al(OH)_3$ phases relative to the microcrystalline boehmite component, which has a constant concentration for all times. [Microcrystalline boehmite grows very slowly, if at all, at 25 and 40 C; it also has a well-defined signature peak in the Raman spectrum at 360 cm^{-1}.] We will do this by defining a bayerite:boehmite peak-height ratio, and plotting this ratio as a function of time.

Figure 4.14 displays a series of plots for a sol aged at 25 C for 1, 4, and 20 hours. After 1 hour, the Raman spectrum shows predominantly boehmite. As time progresses, the bayerite peaks grow, relative to the boehmite peaks. In order to quantitatively characterize this growth, a bayerite:boehmite ratio is defined as the height of the 545 cm^{-1} bayerite peak divided by the height of the 360 cm^{-1} boehmite peak. The peak heights are indicated by arrows in Fig. 4.14(c).

In Fig. 4.15(b) we have plotted the peak ratio as a function of time, for the 25 and 40 C sols. For the 25 C sol (filled circle), bayerite grows rapidly at early times (less than 8 hours), then slows and stops after about 24 hours. The growth for the 40 C sol is slow and linear for all times monitored (48 hours), but is expected to level off at a value similar to the 25 C sol. We did not monitor the growth of bayerite in the 60 C sol (which is mostly nordstrandite), as the growth was very slow. The rate of bayerite growth slows as the temperature increases. This should not be interpreted as being caused by a phase change (bayerite to

nordstrandite) because, as we saw in section 4.4, the $Al(OH)_3$ phases grow at the same rate.

We have also monitored the growth of bayerite by means of weight-loss measurements. This is possible because $Al(OH)_3$ [$2Al(OH)_3=Al_2O_3 \cdot 3H_2O$] and AlO(OH) [$2AlO(OH)=Al_2O_3 \cdot 1H_2O$] contain different amounts of bonded water, which is driven off after heating to 600 C.[10] The percent weight-losses of bayerite and boehmite is 35% and 15% respectively. Mixtures of bayerite and boehmite have percent weight losses between these values. Figure 4.15(a) shows, for the 25 C dried precipitates of Fig. 4.15(b), the percent weight loss as a function of time. The solid lines in Fig. 4.15 follow the same time-dependent form (described below) for bayerite growth. After long processing times, the percent weight loss corresponds to about 60% bayerite and 40% boehmite.

Table 4.4: Bayerite growth parameters for Fig. 4.15 via a fit to the first-order rate equation, $R = A_1 + A_2\{1-\exp[-k(t-\tau)]\}$, where k is the first-order rate constant, τ is a delay time, and R is either relative intensity or weight loss.

Figure	Temperature (°C)	Measurement	k ($hour^{-1}$)	τ (hour)
15(b)	25	rel. intensity	0.21	0.55
15(a)	25	weight loss	0.28	-0.16[a]
15(b)	40	rel. intensity	0.02	0.90

[a]Negative values indicate the presence of bayerite at very early reaction times. There is a time lag (τ less than 1 hour) before Raman detects the presence of bayerite.

We have fit the data of Fig. 4.15 with first-order growth kinetics:

$$R = A_1 + A_2\{1 - \exp[-k(t-\tau)]\}. \qquad (4.1)$$

Here R stands for relative peak intensity or percent weight loss, t is time, k is a first-order rate constant, and τ is an induction period. The results are summarized in Table 4.4. The rate constants determined for the 25 C sol by relative peak intensity and weight loss are comparable (0.21 $hour^{-1}$, and 0.28 $hour^{-1}$ respectively), providing evidence that both methods are measuring essentially the same thing. The rate constant for the 40 C sol is a factor of 10 smaller (0.02 $hour^{-1}$) than for the 25 C sol. Thus a small change in temperature (15 C) has a large effect on the rate of crystal growth. The induction period τ increases with increasing temperature. This may be interpreted as being the delay time (less than 1 hour at both 25 and 40 C) before Raman can detect the bayerite phase. Note that it takes x-ray techniques about 4 hours to detect bayerite.[11] The induction period for the 60 C sols can be several hours or days, depending on the method of hydrolysis. [All materials, for the kinetic studies shown here, were made by adding H_2O to the ASB.]

4.8 X-ray and Infrared Results

In this section, x-ray and infrared (IR) results are shown to verify the presence and assignment of the crystal phases to the materials described in the previous sections, and to give some additional perspective on the Raman scattering results. X-ray, IR, and Raman scattering readily identify the predominant crystalline $Al(OH)_3$ phases present, but each method has some difficulty with mixed phases or with imperfect crystals. Here we use all three methods simultaneously, on materials that contain different amounts of the $Al(OH)_3$ phases, to justify assignments of Raman and IR band frequencies to particular phases.

Figure 4.16 shows the x-ray spectra of 25 and 40 C materials for which the hydrolysis method was water addition to ASB. The known bayerite and nordstrandite x-ray lines are shown at the bottom of the figure. Bayerite has three strong lines at 8.5, 9, and 18 degrees (in 2-theta) and nordstrandite has only one strong peak at 8.5 degrees. Because of the strong overlap of the 8.5-degree bands, the presence of the bayerite and nordstrandite phases are distinguished by the relative intensities of the 8.5-degree common band and the 9- and 18- degree bayerite bands. This analysis shows that the 25 C material is predominantly bayerite, while the 40 C material has some nordstrandite. This x-ray result is consistent with the Raman results of section 4.5; at higher temperatures, the nordstrandite:bayerite ratio increases. The corresponding Raman spectra for these materials are those shown previously in Fig. 4.9

Figure 4.17(a) shows the x-ray spectrum of a 60 C material for which the hydrolysis method was ASB addition to water. Its corresponding Raman spectrum is shown in Fig. 4.12(c). Fig. 4.17(b) is an x-ray spectrum of crystalline boehmite. The known x-ray lines for these materials are indicated at the bottom of the figure. Comparing these spectra indicates that the 60 C material is predominantly a mixture of nordstrandite and microcrystalline boehmite [note the breadth of the boehmite lines in panel (a) with respect to the narrow boehmite lines in panel (b) and the narrow nordstrandite line in panel (a).]

Figure 4.18 shows IR results for 25 C, H_2O-to-ASB and 60 C, ASB-to-H_2O materials. The 25 C spectrum is primarily that of bayerite, as indicated by the previous Raman and x-ray results for 25 C materials. Characteristic IR bands for bayerite are at 3462, 3549, and 3657 cm^{-1}, and these peaks are labeled by a letter b according to the Raman peak labeling system (b, n, g, and B correspond to

bayerite, nordstrandite, gibbsite, and boehmite respectively). The bands at 3622 and 3549 cm^{-1} are characteristic gibbsite bands. While the 3622 cm^{-1} band is common to nordstrandite also, the 3549 cm^{-1} band is not. Therefore the 3622 cm^{-1} band is assigned to gibbsite in the top trace. A missing gibbsite band at 3468 cm^{-1} may be hidden by the relatively broad bayerite band at 3462 cm^{-1}. The 3374 cm^{-1} band has also been associated with the gibbsite phase, for two reasons. First, gibbsite is known to have a peak at 3381 cm^{-1} which red shifts down to 3358 cm^{-1} at low temperatures[12] (lattice strain can have a similar effect). Second, this peak is not seen in the nordstrandite IR spectrum (bottom trace) and all of the bayerite Raman bands are above 3420 cm^{-1}. The 3437 cm^{-1} band could be either an IR band associated with the 3438 cm^{-1} Raman band of bayerite, or an IR band associated with the 3431 cm^{-1} Raman band of gibbsite.

The lower spectrum in Fig. 4.18, observed for the 60 C, ASB-to-H_2O material, exhibits mainly bands attributable to nordstrandite. IR bands for nordstrandite are at 3622, 3563, 3494, 3421, and 3361 cm^{-1}. These values compare favorably with literature values for nordstrandite,[13] with the exception of a reported 3527 cm^{-1} band that we do not see. Additional very broad bands at 3089 and 3297 cm^{-1} are due to microcrystalline boehmite.

There are several interesting relationships between the Raman and IR spectra of the three $Al(OH)_3$ phases. A 3622 cm^{-1} band is common to gibbsite and nordstrandite in both the Raman and IR spectra. A 3361 cm^{-1} band is Raman-active in gibbsite and IR-active in nordstrandite. A 3421 cm^{-1} band is Raman-active bayerite and IR-active in nordstrandite. A 3524 cm^{-1} band is Raman-active in both nordstrandite and gibbsite. Also, bayerite and nordstrandite show three bands not normally observed in their Raman spectra.

These Raman, IR, and x-ray results are consistent with the x-ray work performed by Aldcroft et al.[14] At room temperature, the predominant phase is bayerite, with some gibbsite present; at 60 C, the predominant phase is nordstrandite, with some bayerite present.

4.9 Summary

Raman, infrared, and x-ray measurements were carried out for precipitates of solution grown materials, prepared by the hydrolysis of aluminum secondary butoxide, at temperatures of 25, 40, and 60 C. The precipitates consisted of three phases of $Al(OH)_3$ (bayerite, nordstrandite, and gibbsite) and an AlO(OH) phase (boehmite). We have determined the effect of the rate of hydrolysis and the solution processing temperature, on the crystal phase mix (the relative proportions of the $Al(OH)_3$ crystal phases). The phase mix depends on the temperature and the rate of hydrolysis, but not on time. This shows that the crystal nucleation kinetics, during hydrolysis, determines the phase mix. Also first order growth kinetics were monitored for bayerite. The initial rate of bayerite growth decreases with increasing temperature.

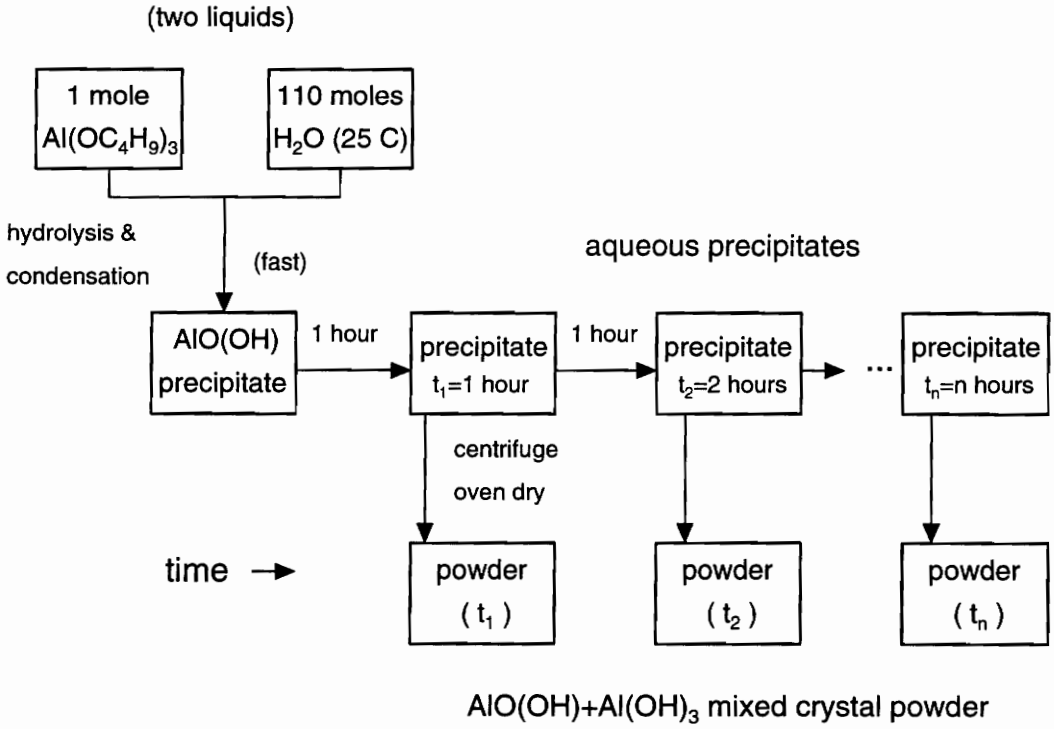

Fig. 4.1: Schematic of the materials synthesis procedure. Aluminum sec-butoxide is hydrolyzed to produce an aqueous precipitate, with an AlO(OH) stoichiometry. The solution is allowed to age. At selected time intervals, a sample is removed from the reaction vessel, centrifuged, and oven dried (110 C). Raman, infrared, and x-ray studies were done on solids prepared by using various, aging times (t_n), temperatures (25, 40, and 60 C), and hydrolysis methods.

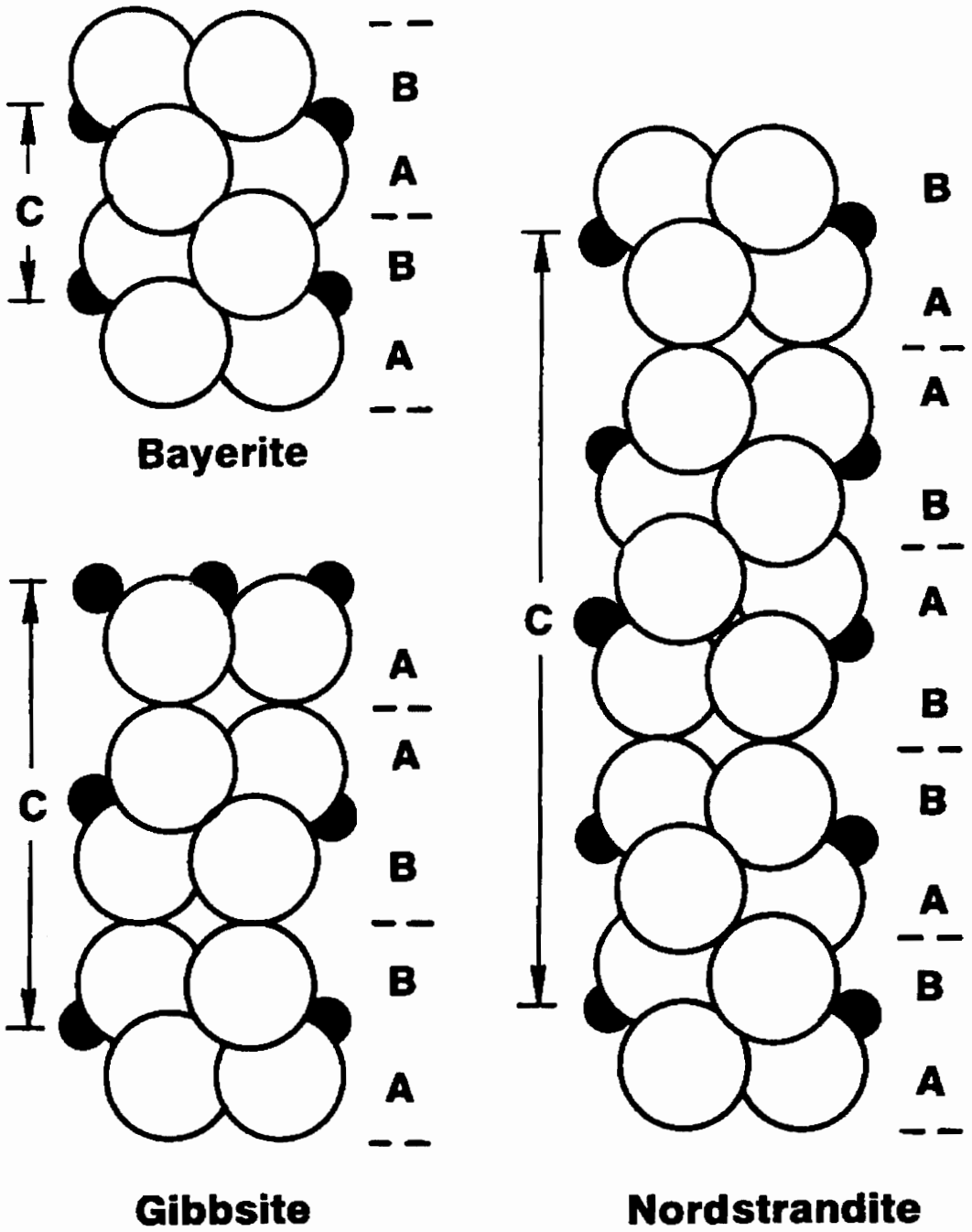

Fig. 4.2: Comparison of the $Al(OH)_3$ crystal phases, bayerite, nordstrandite and gibbsite. These materials have layered structures. This figure was reproduced from Wefers and Misra.[5]

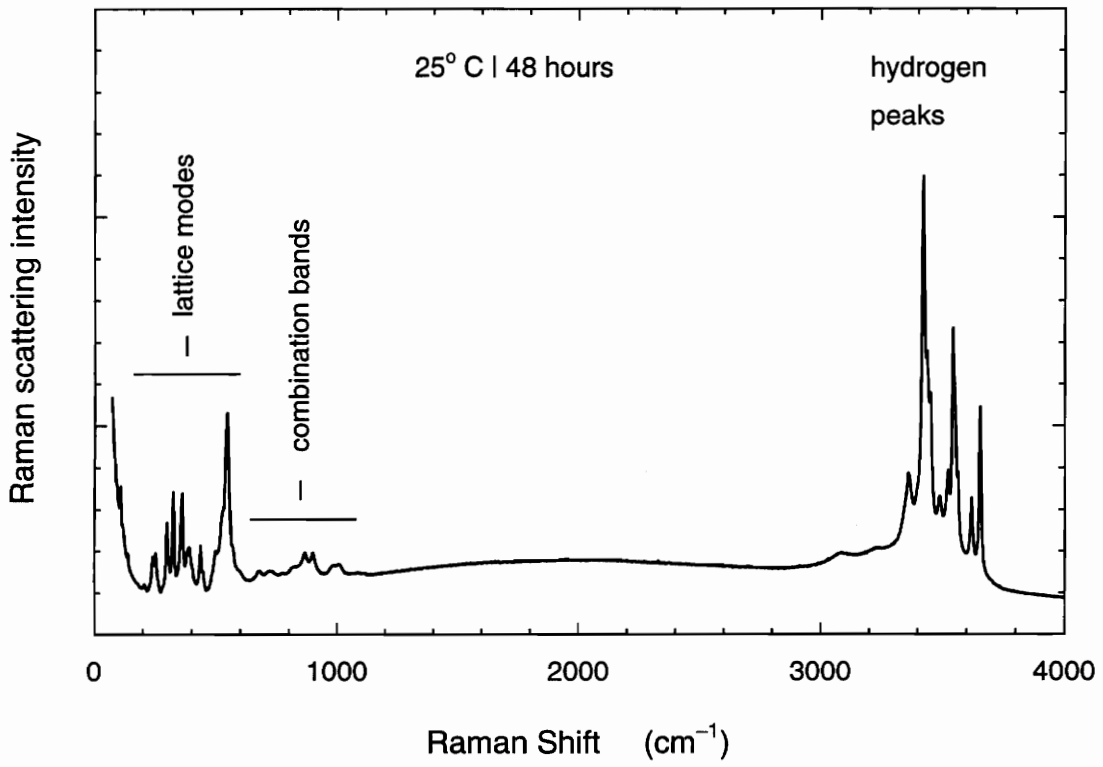

Fig. 4.3: Raman spectrum for a precipitate that was aged for 48 hours at 25 C. This spectrum was obtained with 514.5 nm excitation, and a 4.0 cm^{-1} bandwidth. Three distinct spectral regions are observed. The low frequency lattice band region between 100 and 600 cm^{-1}, the combination band region between 600 and 1200 cm^{-1}, and the high frequency hydrogen band region between 3000 and 3800 cm^{-1}. The combination band frequencies are integral linear combinations of the lattice mode frequencies (Table 4.1). This material is predominantly bayerite.

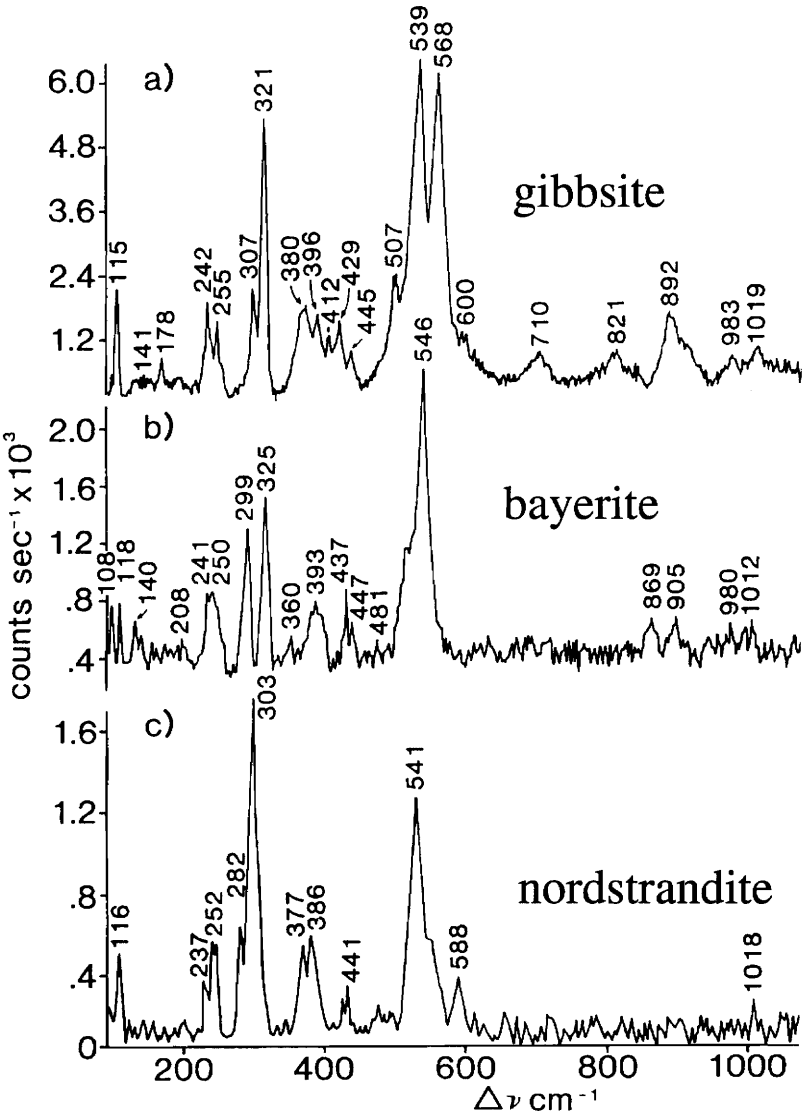

Fig. 4.4: Low frequency Raman spectra of nordstrandite, bayerite, and gibbsite from Rodgers.[8] The most intense bands are between 290 and 330 cm^{-1}, and between 530 and 570 cm^{-1}.

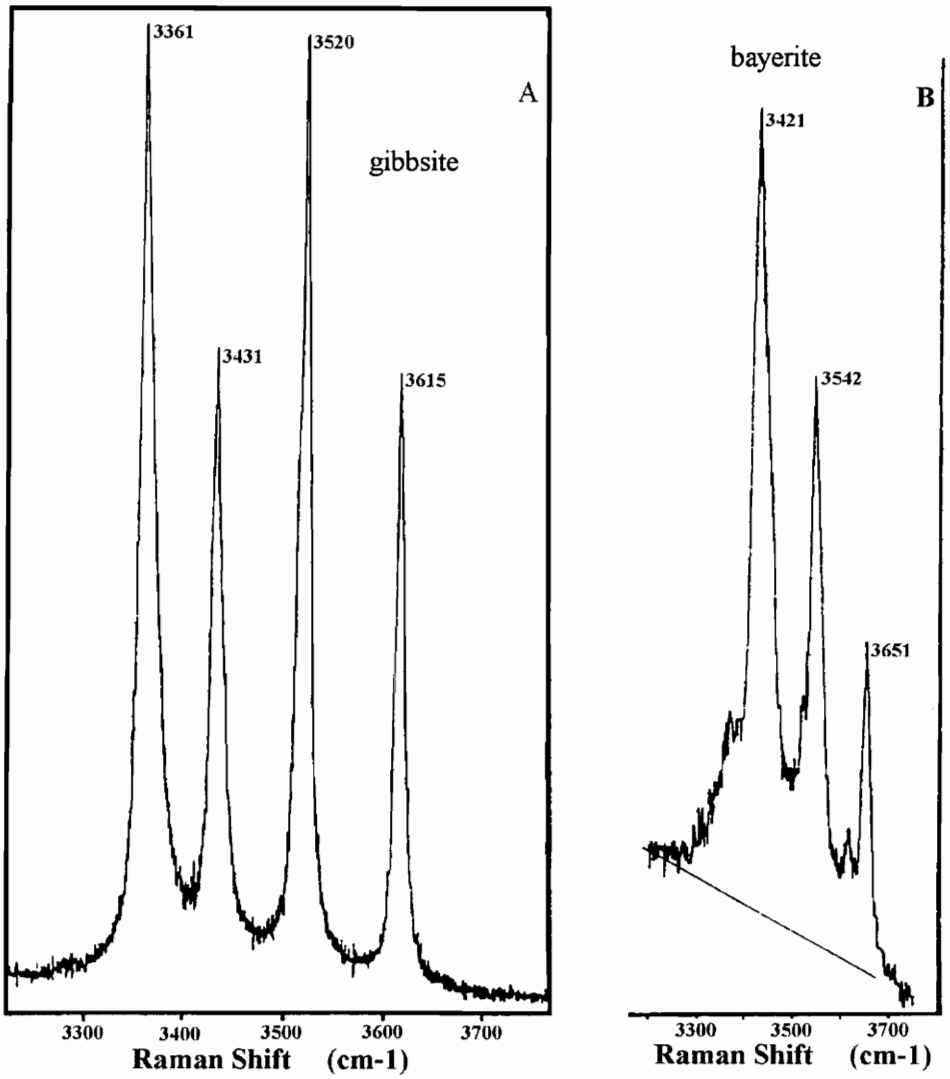

Fig. 4.5: Raman spectra for the high-frequency hydrogen region of gibbsite and bayerite from Huneke et al.[7] These bands are useful for phase identification of the $Al(OH)_3$ polymorphs.

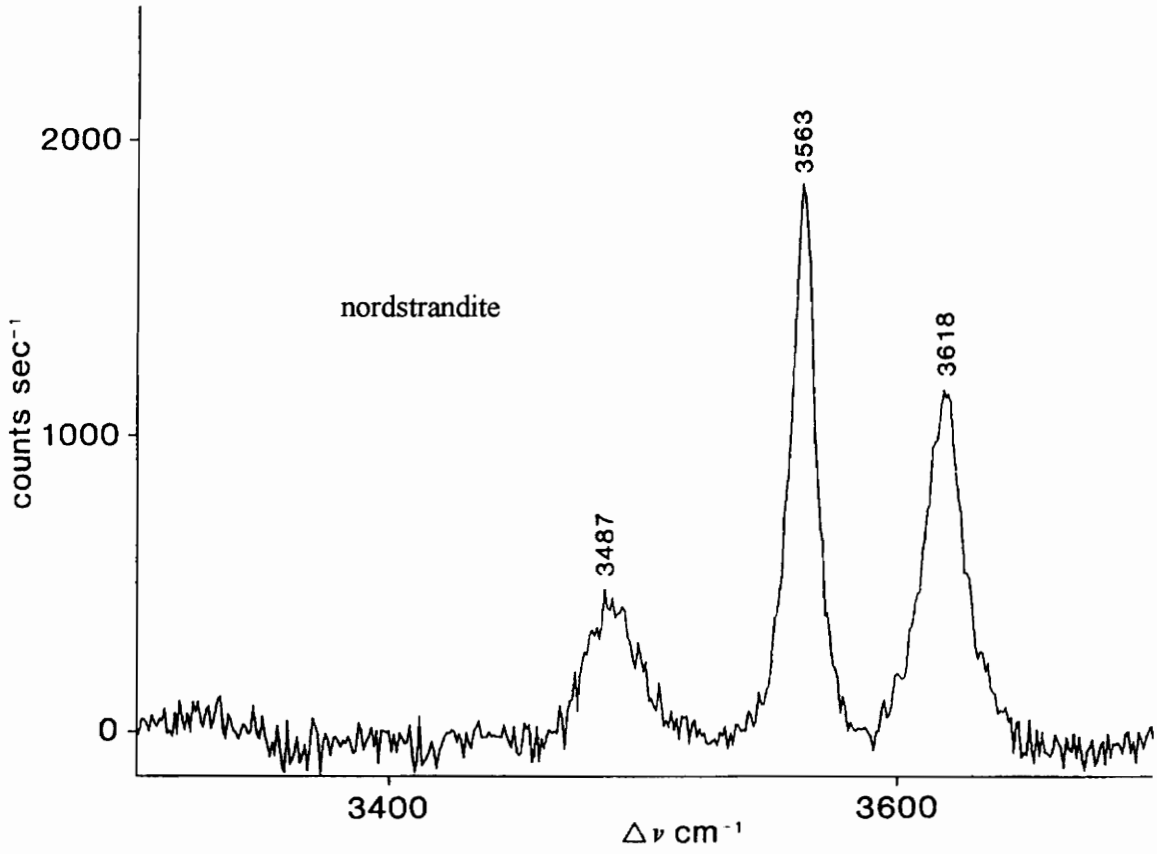

Fig. 4.6: Raman spectrum of the high-frequency hydrogen region of nordstrandite from Rodgers.[8] Compare these bands with those of bayerite and nordstrandite of Fig. 4.5. Nordstrandite and gibbsite both have a 3620 cm^{-1} band.

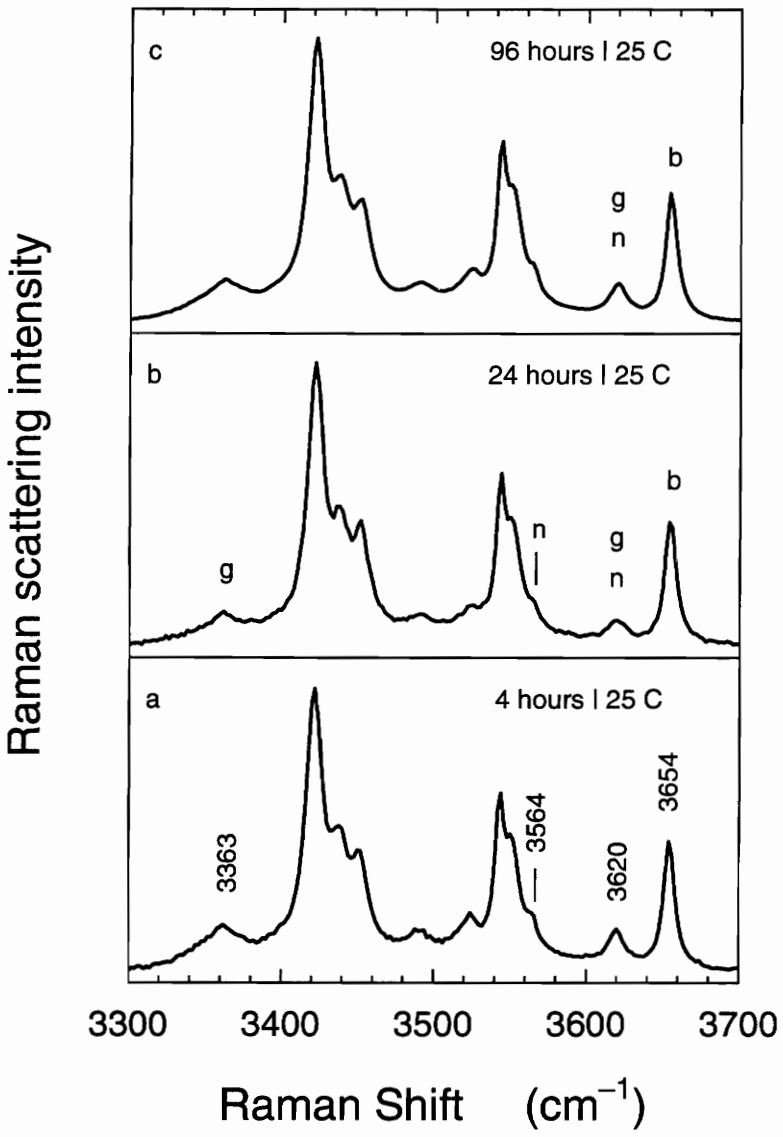

Fig. 4.7: Comparison of the Raman spectra of materials processed at 25 C for (a) 4 hours, (b) 24 hours, and (c) 96 hours. (These spectra, as well as those shown in the following figures, were obtained with 514.5 nm excitation and a 2 cm^{-1} incremental step size.) The letters n, b, and g locate bands caused by nordstrandite, bayerite, and gibbsite respectively. The relative intensities of the bands caused by these phases are constant. This shows that the relative concentrations of the $Al(OH)_3$ phases are not a function of time. Fig. 4.8 gives similar results for 40 C materials.

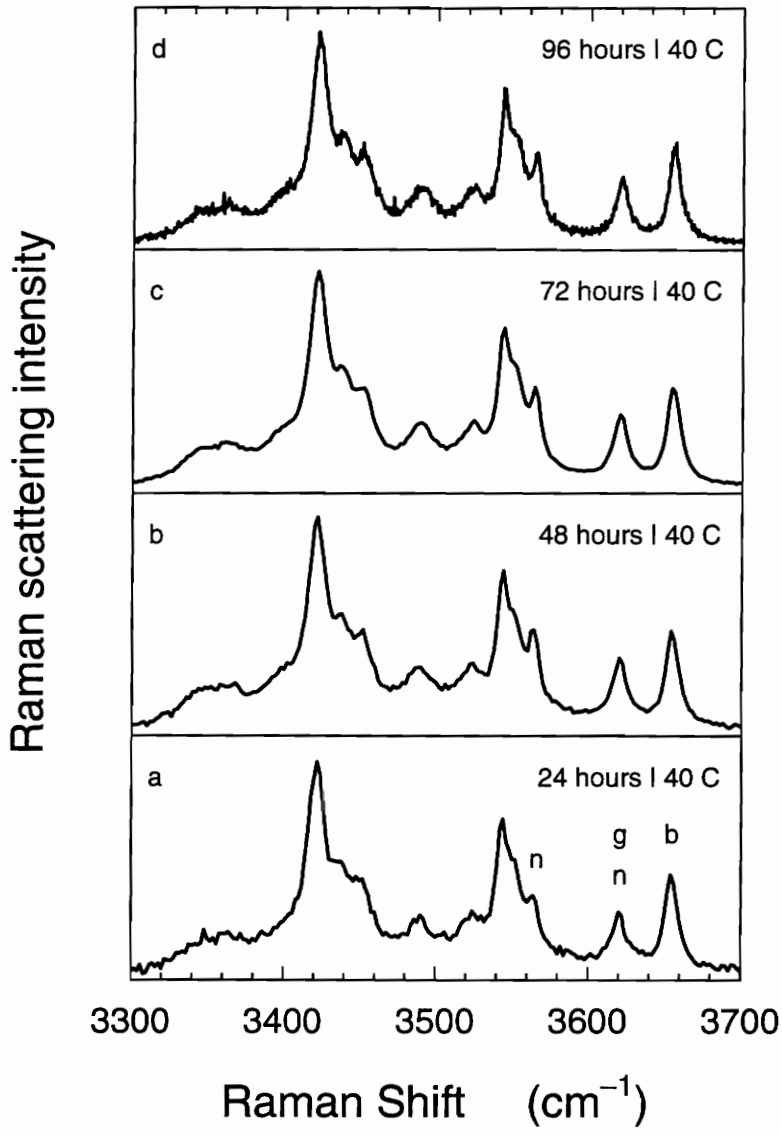

Fig. 4.8: Comparison of the Raman spectra of materials processed at 40 C for (a) 24 hours, (b) 48 hours, (c) 72 hours, and (d) 96 hours. The letters n, b, and g locate bands caused by nordstrandite, bayerite, and gibbsite respectively. The relative intensities of the bands caused by these phases are constant. This shows that the relative concentrations of the $Al(OH)_3$ phases are not a function of time. Fig. 4.7 gives similar results for 25 C materials.

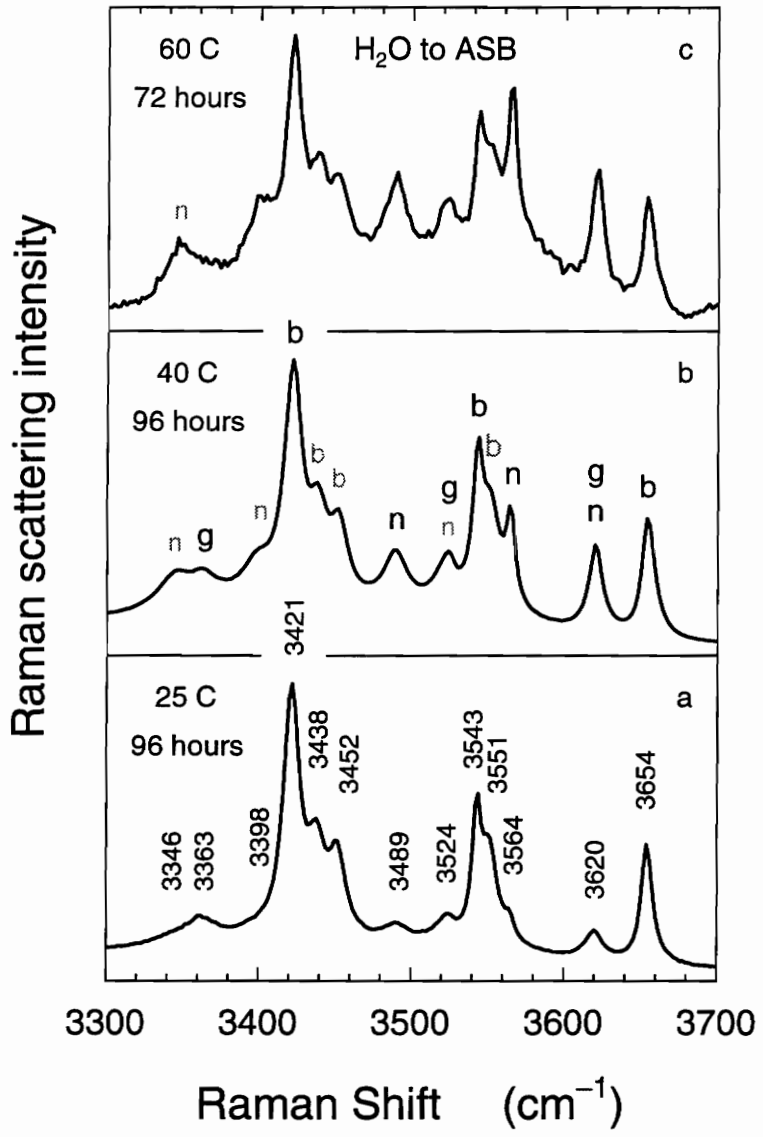

Fig. 4.9: Comparison of the hydrogen band Raman spectra of materials processed at (a) 25 C, (b) 40 C, and (c) 60 C. The precursors were mixed by adding the water to the aluminum sec-butoxide (ASB). The letters n, b, and g locate bands caused by nordstrandite, bayerite, and gibbsite respectively. Bands labeled by gray scale letters are not usually seen, or have not been previously assigned to the phases indicated by the letters (this will be discussed further in Fig. 4.10). The relative intensity of the bands caused by nordstrandite increase with respect to the bayerite bands, as a function of temperature. This shows that the concentration of nordstrandite increases with respect to bayerite, as a function of temperature.

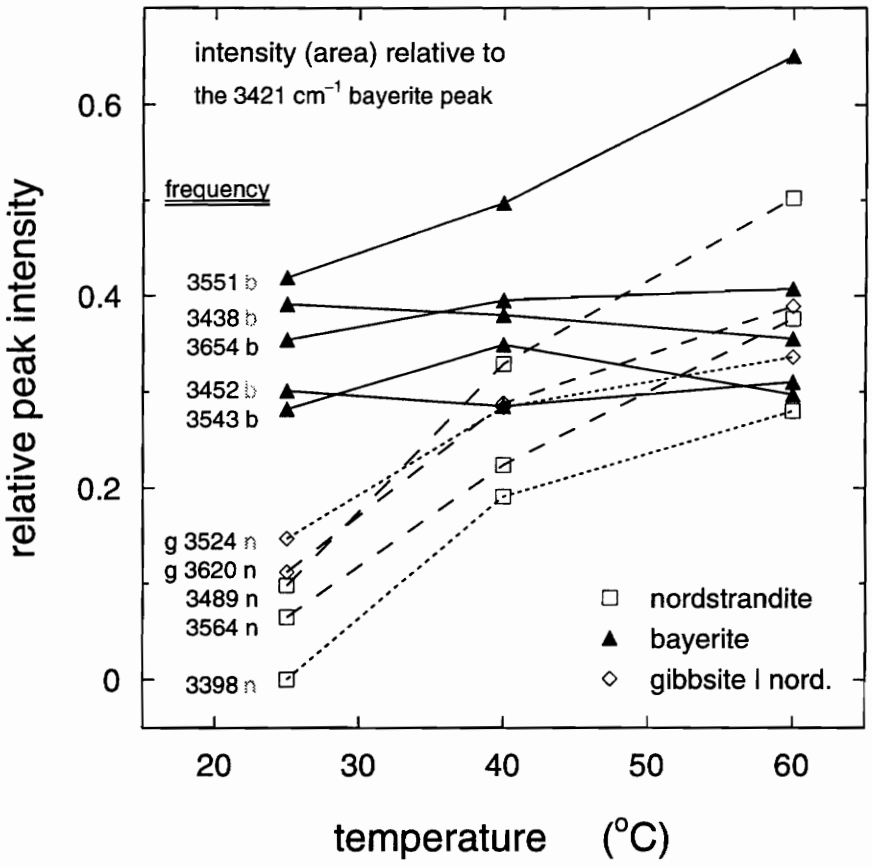

Fig. 4.10: The influence of temperature on the relative peak intensities of the Raman hydrogen bands. The relative intensity of each peak was determined by dividing its peak area by the area of the strong 3421 cm^{-1} bayerite band. The frequency of the corresponding band is indicated to the left of the 25 C data. The letters n, b, and g indicate frequencies, or bands, caused by nordstrandite, bayerite, and gibbsite respectively. Bands labeled by gray scale letters are not usually seen, or have not been previously assigned to the phases indicated by the letters. This analysis provides a basis for those assignments. The relative peak intensity of the nordstrandite bands increase with temperature. The relative intensities of the bayerite bands are constant, except for the 3551 cm^{-1} band.

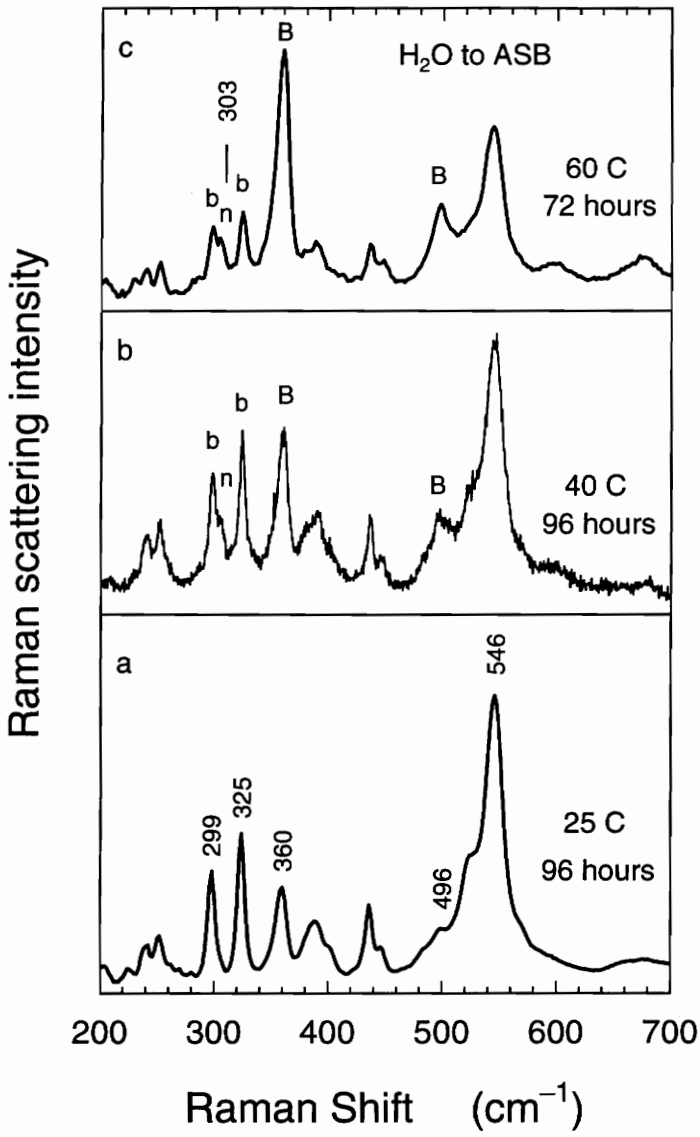

Fig. 4.11: Comparison of the low-frequency Raman spectra of materials that were processed at (a) 25 C, (b) 40 C, and (c) 60 C. The precursors were mixed by adding the water to the aluminum sec-butoxide (ASB). The letters n, b, g, and B, locate bands caused by nordstrandite, bayerite, gibbsite, and boehmite respectively (gibbsite is not observed in these spectra). The bands strongly overlap in this region. The nordstrandite band at 303 cm^{-1} increases relative to the bayerite band at 299 cm^{-1}, as a function of temperature. The relative intensity of the boehmite band at 360 cm^{-1} also increases as a function of temperature; this is misleading because the relative amounts of boehmite and the $Al(OH)_3$ phases are strongly time dependent.

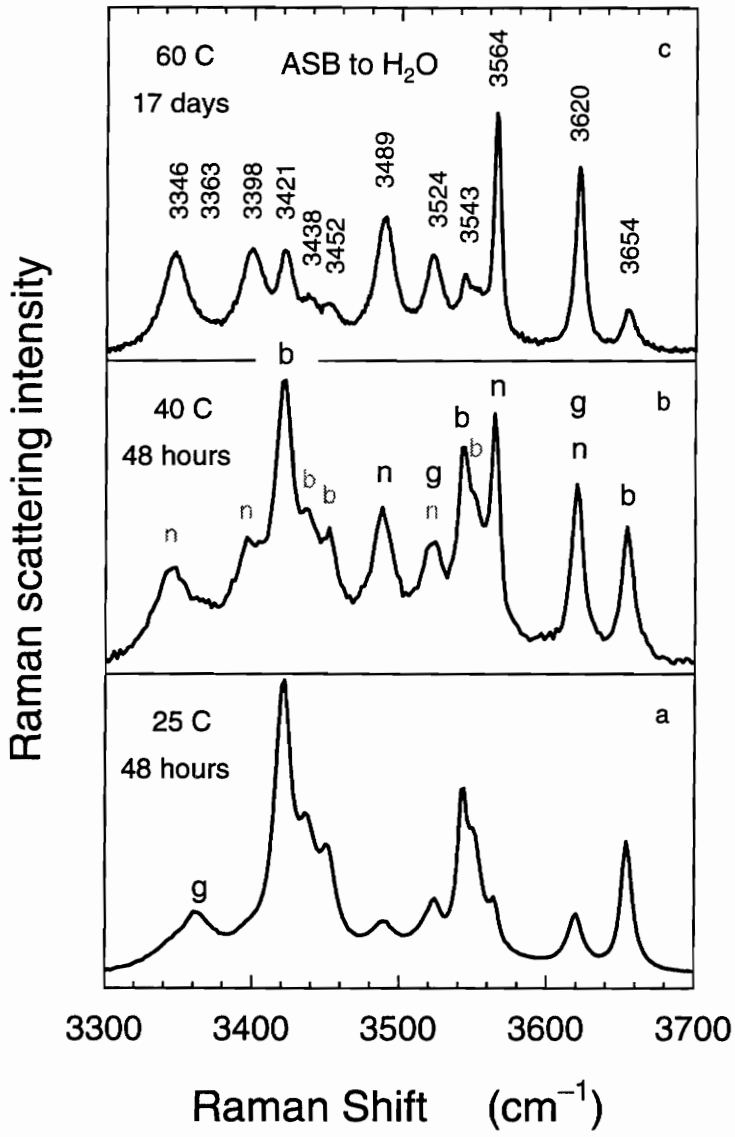

Fig. 4.12: Comparison of the hydrogen band Raman spectra of materials processed at (a) 25 C, (b) 40 C, and (c) 60 C. The precursors were mixed by adding the aluminum sec-butoxide (ASB) to the water by syringe. The letters n, b, and g locate bands caused by nordstrandite, bayerite, and gibbsite respectively. Bands labeled by gray scale letters are not usually seen, or have not been previously assigned to the phases indicated by the letters. The relative intensity of the bands caused by nordstrandite increase with respect to the bayerite bands, as a function of temperature. This result is the same as that obtained in Fig. 4.9. Comparing this figure with Fig. 4.9 shows that these materials have more nordstrandite relative to bayerite, at each temperature. The method of hydrolysis is the cause of this result as the hydrolysis method strongly effects the nucleation kinetics.

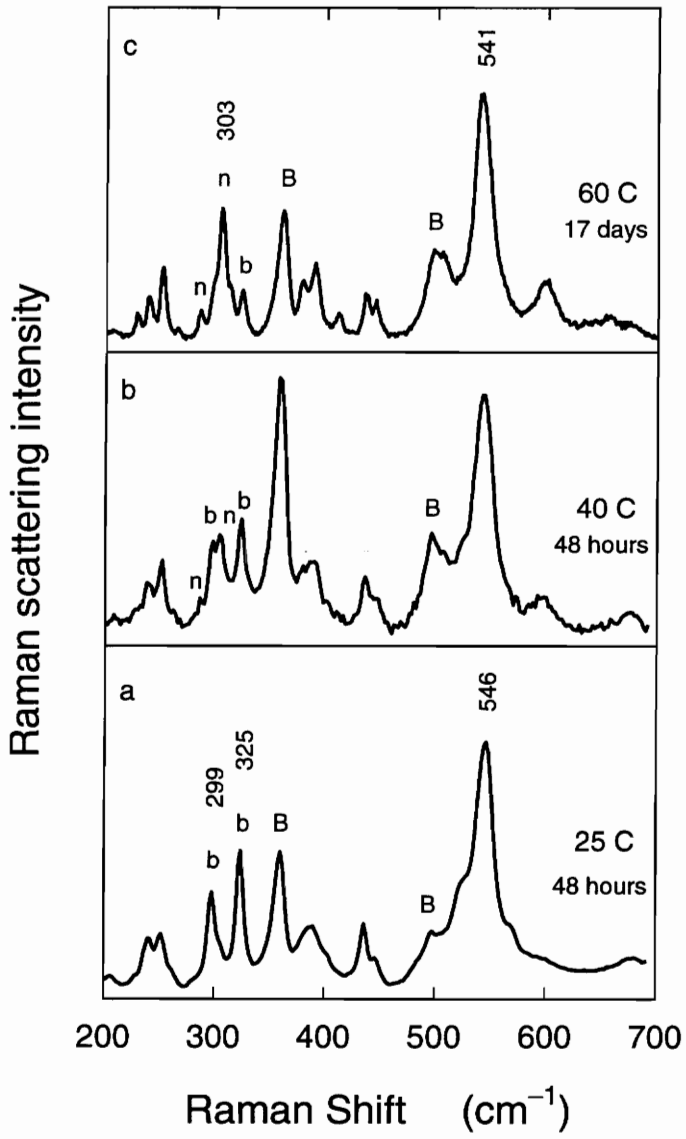

Fig. 4.13 Comparison of the low-frequency Raman spectra of materials processed at (a) 25 C, (b) 40 C, and (c) 60 C. The precursors were mixed by adding the aluminum sec-butoxide (ASB) to the water by syringe. The letters n, b, and g locate bands caused by nordstrandite, bayerite, and gibbsite respectively. Bands labeled by gray scale letters are not usually seen, or have not been previously assigned to the phases, in the indicated phases. The relative intensity of the bands caused by nordstrandite increases with respect to the bayerite bands, as a function of temperature. This result is the same as that obtained in Fig. 4.9. Comparing this figure with Fig. 4.9 shows that these materials have more nordstrandite relative to bayerite, at each temperature. The method of hydrolysis is the cause of this result, because the hydrolysis method strongly effects the nucleation kinetics.

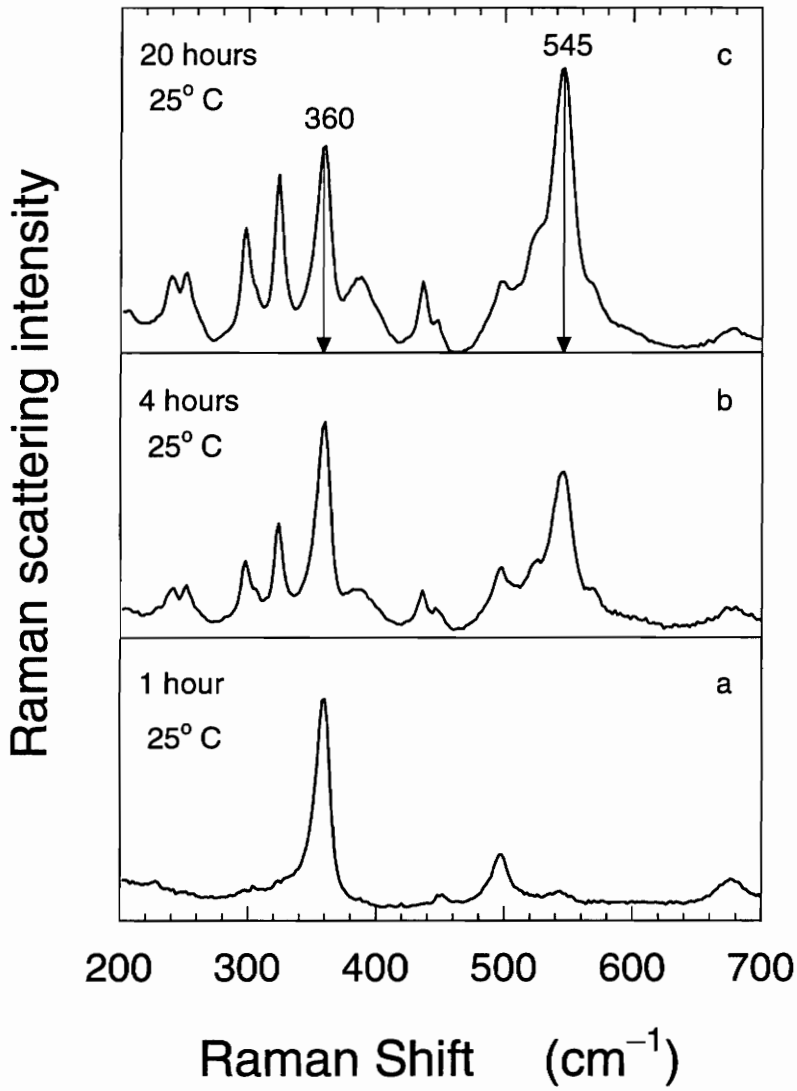

Fig. 4.14: Spectral evidence for bayerite growth. Shown are the low-frequency Raman spectra of materials processed at 25 C for (a) 1 hour, (b) 4 hours, and (c) 20 hours. The presence of boehmite is indicated by the band at 360 cm^{-1}, and the presence of bayerite is indicated by the 545 cm^{-1} band. The bayerite band increases relative to the boehmite band. The ratio of these peak heights is plotted as a function of time in Fig. 15(b).

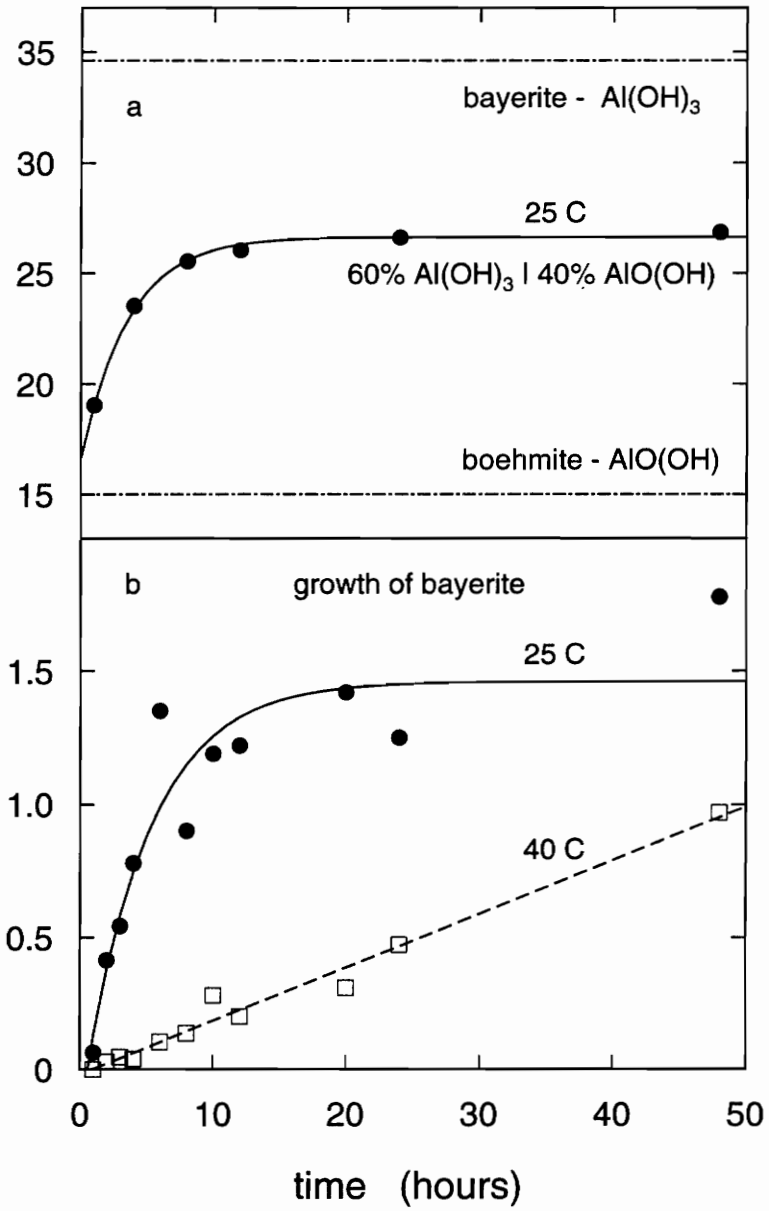

Fig. 15: The first order growth kinetics of bayerite. The top panel plots percent weight loss versus time for materials processed at 25 C. The percent weight loss was obtained from thermogravimetric analysis. The percent weight loss of bayerite and boehmite is 35% and 15% respectively. Mixtures of bayerite and boehmite have percent weight losses between these values. The bottom panel plots the bayerite(545 cm^{-1}):boehmite(360 cm^{-1}) peak height ratio versus time (see Fig. 14), for materials processed at 25 C and 40 C. The solid line is an analytical fit to the first order equation (eqn. 4.1) $R = A_1 + A_2\{1 - \exp[-k(t-\tau)]\}$. The results of the analytical fits, for the rate constant k and delay time τ, are given in Table 4.4.

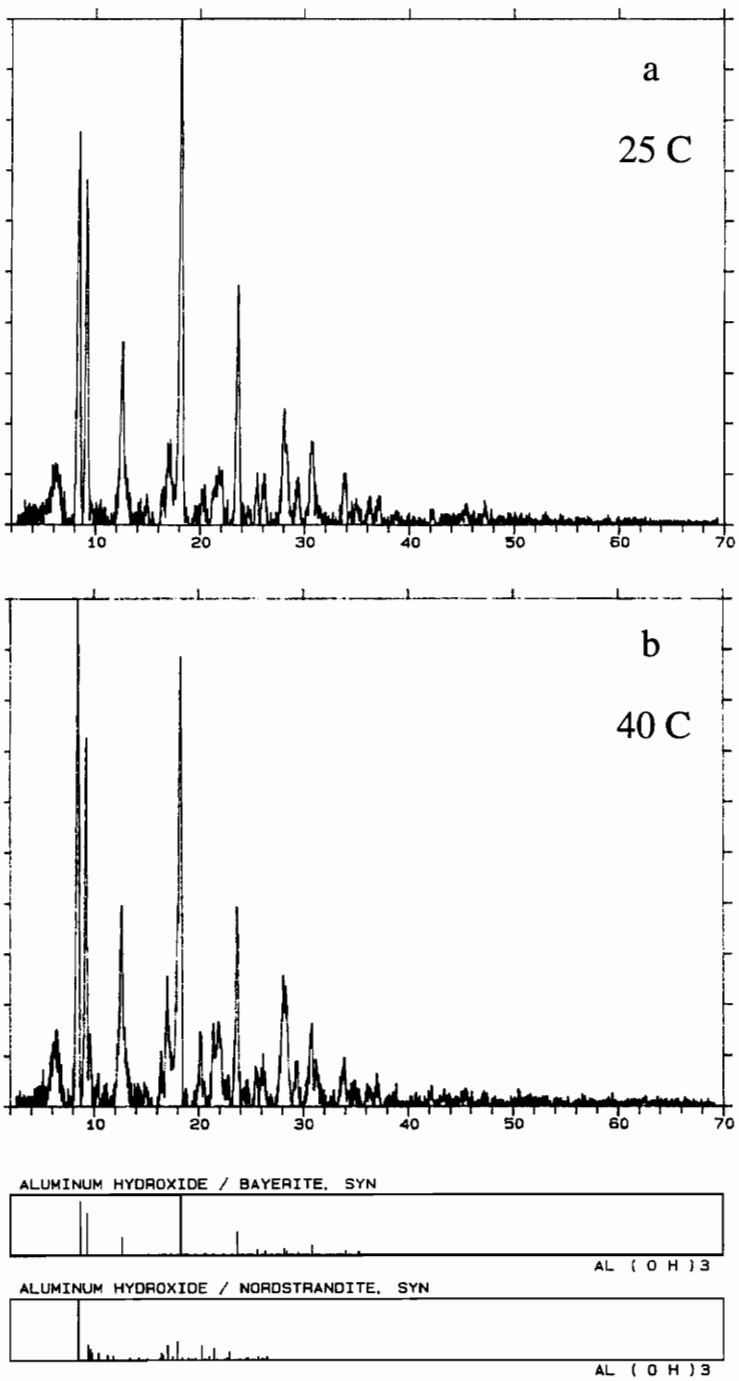

Fig. 16: X-ray analysis of materials processed at (a) 25 C and (b) 40 C. The bottom two panels are synthetic x-ray lines for bayerite and nordstrandite. This shows that the 25 C material is composed primarily of bayerite, and that the 40 C material is composed of a mixture of bayerite and nordstrandite. X-ray analysis was carried out by Milton Furgeson, using Mo radiation with a wavelength of 0.7093 Å.

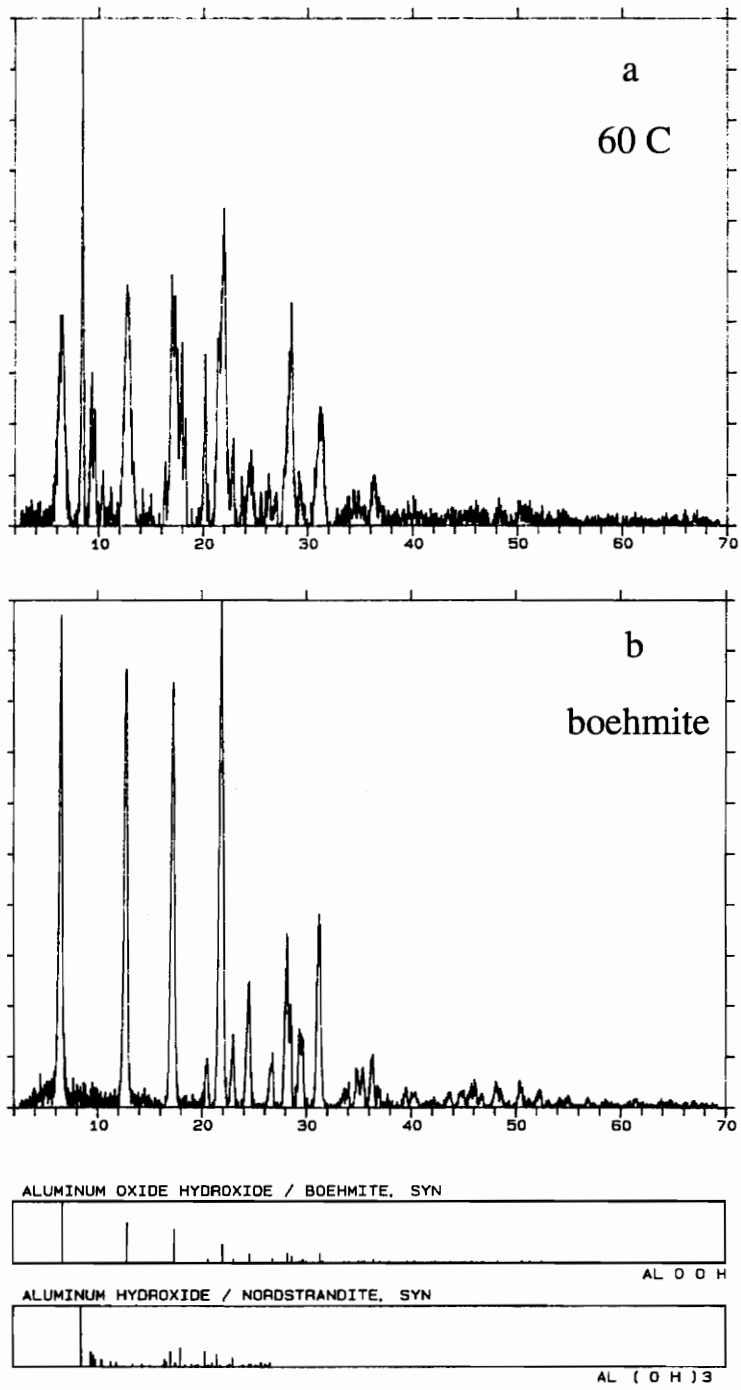

Fig. 17: X-ray data for (a) a material processed at 60 C and (b) a crystalline boehmite sample. The bottom panels are synthetic data for boehmite and nordstrandite. The 60 C material is a mixture of nordstrandite and boehmite. X-ray analysis was carried out by Milton Furgeson, using Mo radiation with a wavelength of 0.7093 Å.

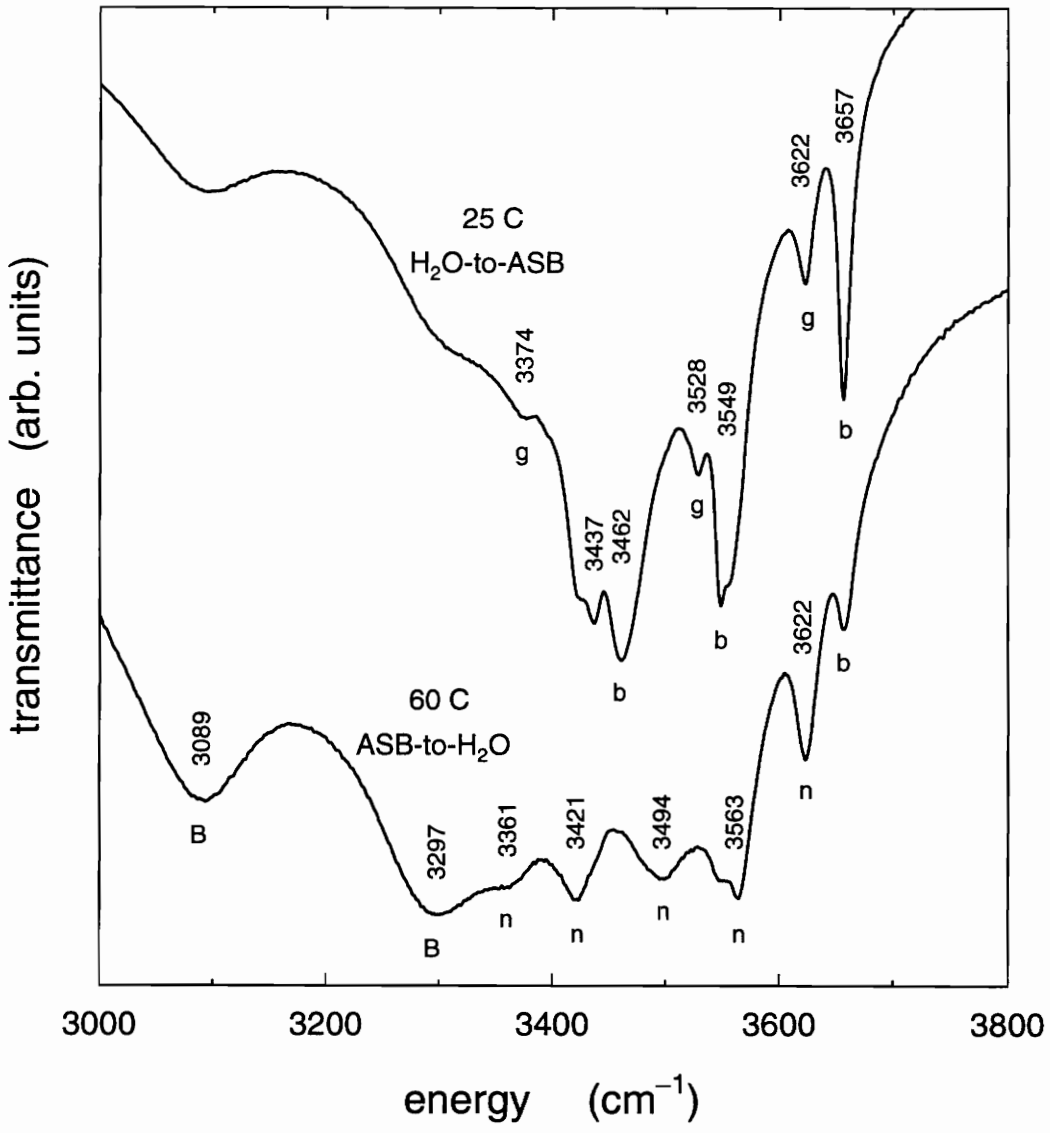

Fig. 4.18: Infrared data for 25 C [H_2O-to-ASB (aluminum sec-butoxide)] and 40 C (ASB-to H_2O) materials. The letters n, b, g, and B, locate bands caused by nordstrandite, bayerite, gibbsite, and boehmite respectively. The 25 C sample is composed primarily of bayerite, with some gibbsite and boehmite. The 40 C material is composed primarily of nordstrandite, with a significant amount of boehmite and some bayerite.

---

[1]B. E. Yoldas, Amer. Ceram. Soc. Bull. **54**, 286 (1975); B. E. Yoldas, Amer. Ceram. Soc. Bull. **54**, 289 (1975); B. E. Yoldas, J. Mater. Sci. **10**, 1856 (1975).

[2]B. E. Yoldas, J. Appl. Chem. Biotech. **23**, 803 (1973).

[3]D. Aldcroft, G. C. Bye, and C. A. Hughes, J. Appl. Chem. **19**, 167 (1969).

[4]G. C. Bye and J. G. Robinson, J. Appl. Chem. Biotech. **24**, 633 (1974).

[5]K. Wefers and C. Misra, Oxides and Hydroxides of Aluminum, Alcoa Technical Paper 19, revised (Alcoa Laboratories, Alcoa Center, 1987).

[6]K. Wefers and C. Misra, Oxides and Hydroxides of Aluminum, Alcoa Technical Paper 19, revised (Alcoa Laboratories, Alcoa Center, 1987); B. C. Lippens, Thesis, Tech. Univ. Delft (1961).

[7]J. T. Huneke, R. E. Cramer, R. Alvarez, and S. A. El-Swaify, Soil Sci. Soc. Am. J. **44**, 131 (1980).

[8]K. A. Rodgers, Mitt. Abt. Landesmuseum Joanneum **59**, 19 (1991).

[9]B. E. Yoldas, J. Appl. Chem. Biotech. **23**, 803 (1973); G. C. Bye and J. G. Robinson, J. Appl. Chem. Biotech. **24**, 633 (1974).

[10]B. E. Yoldas, J. Appl. Chem. Biotech. **23**, 803 (1973)

[11]G. C. Bye and J. G. Robinson, J. Appl. Chem. Biotech. **24**, 633 (1974)

[12]R. Freymann, J. J. Meuleman, and M. R. Lucas, C. R. Acad. Sc. Paris **286B**, 151 (1978).

[13]U. Hauschild, Z. Anorg. Allg. Chem. **324** 15 (1963).

[14]D. Aldcroft, G. C. Bye, and C. A. Hughes, J. Appl. Chem. **19**, 167 (1969).

CHAPTER FIVE

THE ZIRCONIA AND MAGNESIA SYSTEMS

5.1 Introduction

In this chapter, two different systems are discussed, the zirconia system and the magnesia system. The zirconia system is a sol-gel system that produces amorphous gels and precipitates; this system is very different from the alumina sol-gel system. For example, while water is the continuous phase in sol-gel alumina, n-propanol is the continuous phase in the zirconia system and atmospheric water is used for the hydrolysis reaction. The zirconia materials display a very broad low-frequency band (or an "amorphous band") in the Raman spectrum, similar to the amorphous bands observed for sol-gel silica.[1] This system is of scientific interest because relatively little is known about the structure and properties of non-Zachariazen[2], highly-ionic, amorphous solids.

The magnesia system is a spin-off of a magnesium carbonate sol-gel system. Phase changes due to heat treatments are our primary interest. Raman analysis of magnesium carbonate decomposition, as a function of temperature, has led to a method of monitoring both the magnesium carbonate and the ensuing magnesia produced, in the 400 to 600 C temperature range. This takes on significance when it is realized that magnesia, MgO, is not Raman active, because of its rocksalt structure. Instead of a Raman signal, a luminescence band produced by $MgO:Cr^{+++}$ is used to detect the presence of magnesia. A judicious choice of exciting laser line allows both the Raman bands of magnesium carbonate materials

and the luminescence bands of magnesia to show up in the "Raman spectrum" of the mixed crystal systems.

5.2 Experimental

5.2.1 Preparation of zirconia materials

Zirconia gels were prepared by the following method. Zirconium n-propoxide, as $Zr(OC_3H_7)_4 \cdot 2.8C_3H_7OH$ (stoichiometry as received from manufacturer), a liquid at room temperature, was mixed with a larger quantity of n-propanol, C_3H_7OH. The recipe was 10 ml of zirconium n-propoxide mixed with 100 ml of n-propanol. To this mixture was added approximately 1 ml of glacial acetic acid. The reaction vessel was then covered with aluminum foil perforated with several small holes; the purpose of the small holes in the foil was to allow atmospheric water to slowly hydrolyze the sol. A gel formed on the order of days. If, however, there were no holes in the aluminum foil, gelation did not occur. The relative humidity of the room air is therefore an important parameter. Various zirconia materials, based upon this method of preparation, are discussed in the text.

5.2.2 The magnesium carbonate materials.

The magnesite, hydromagnesite, and magnesia samples were obtained from commercial sources. Magnesite is $MgCO_3$, hydromagnesite is $4MgCO_3 \cdot Mg(OH)_2 \cdot 5H_2O$, and magnesia is MgO. Heat treatments were carried out in the following way. Samples were placed in a furnace (Lindberg box furnace model 51542, with a Platinel II thermocouple and model 59344 control console) and ramped to the "treatment temperature" at a rate of 5 °C per minute. They remained at the treatment temperature for two hours before being ramped back down to room temperature.

5.3 Precursors to the Sol-Gel Zirconia System

The methodology for making the clear amorphous zirconia gels is well defined but poorly understood. In order to understand the role of each of the precursor chemicals, it is necessary to determine the overall chemistry of the system. This section presents results of my Raman-scattering examination of the unreacted precursor materials. In the next section, the Raman spectra of several gels will be examined to determine which precursor is responsible for selected Raman spectral features. Because the Raman spectral features will have changed with respect to the original spectral features of the precursor, it is concluded that that precursor has indeed chemically reacted and is still part of the gel system.

Figure 5.1 shows the Raman spectra of the precursor materials, except for atmospheric water. Panel a shows the Raman spectrum of zirconium n-propoxide. Weight loss measurements show that this material is about 25% ZrO_2 by weight, and therefore has a stoichiometry of approximately $Zr(OC_3H_7)_4 \cdot 2.8C_3H_7OH$. A strong and very broad luminescence background was subtracted from this spectrum. The Raman spectrum of zirconium n-propoxide is very similar to, but can be differentiated from, n-propanol's spectrum, which is shown in panel b. Panel c shows the Raman spectrum of acetic acid. Acetic acid is a necessary additive for the production of a *clear* gel, and its role is of primary importance. Panel d shows the very simple spectrum of hydrogen peroxide; the band at 875 cm^{-1} is the HO–OH symmetric stretching mode.[3] Hydrogen peroxide is not part of the zirconia gel system, and its application to the gel reduces the gel to a white powder. Hydrogen peroxide was applied to the gels in order to try to remove organics from the system, which were suspected of producing a strong luminescence hindering the observation of the Raman spectrum of the gels.

Debsikdar[4,5] used hydrogen peroxide to rid his zirconia gel samples of organics in a similar system. It is found here that its effect has much more drastic, but interesting, consequences.

5.4 The Chemistry of the Zirconia Gels

Several amorphous zirconia materials, closely related to the zirconia gel, were examined by Raman scattering. The actual zirconia gels themselves were not studied directly because the gels are predominantly n-propanol, and this is the only component of the gel observed in the Raman spectrum. Efforts to reduce the n-propanol component included simple evaporation as well as the addition of hydrogen peroxide; each method has its merits and difficulties. The analysis of the amorphous zirconia materials yielded essential information of the chemistry of the system.

Figure 5.2 displays the Raman spectra of the amorphous zirconia materials. Panel a shows the spectrum of a xerogel produced by drying a zirconia gel sample. This xerogel is expected to be very similar to the gel as far as the nanostructure is concerned (structure on an atomic scale). Spectra for these materials are difficult to obtain. If they are too "wet", n-propanol dominates the spectrum, and if they are too "dry", the samples turn a reddish or yellowish color and luminescence dominates the spectrum.

Panel b of Fig. 5.2 shows the Raman spectrum of a xerogel that was treated with a hydrogen peroxide solution. The bands at 529, 617, 659, and 954, as well as the bands above 1300 cm^{-1}, all align very well with bands observed in panel a and are interpreted as being caused by the same source. Differences between panel a and panel b show up in a very broad band centered at 454 cm^{-1} and a much narrower band at 843 cm^{-1} (both in panel b), and the broad band centered at

426 cm^{-1} (in panel a). Also, the band at 529 cm^{-1} is less intense in panel b than in panel a.

The Raman spectrum shown in panel c of Fig. 5.2 is for a material made by adding a peroxide solution to zirconium n-propoxide directly, with no other additives present (such as acetic acid and n-propanol, which are used in the gel-making process and therefore are present in the materials of panels a and b). This material shows essentially only two bands, a broad band centered at 470 cm^{-1} and one centered at 843 cm^{-1}. These bands of panel c are very similar to corresponding bands contained in panel b, and are interpreted as corresponding to the same source.

Panel d shows the Raman spectrum of a material produced by adding only water to zirconium propoxide. This spectrum was difficult to obtain because of a high luminescence background and weak Raman intensity. Weak plasma lines from the krypton laser, indicated by the letter p, show up in this spectrum because of the long scanning time (18 hours). Nevertheless, a broad band is clearly observed, centered around 480 cm^{-1}, that is very similar to the bands observed in panels b and c. This broad band is interpreted as arising from the same material source in each case.

The assignments of the various bands will now be discussed. The bands at 529, 619, 661, 952, and above 1300 cm^{-1} are only observed in materials which contain some acetic acid. Therefore acetic acid is the source of these bands. Most of these bands are shifted from the bands seen, in Fig. 5.1c, in acetic acid itself. This reflects chemical effects on the COOH groups incorporated in the solids of Fig. 5.2. The role of the acetic acid can be viewed as providing a chemical modification of the precursor, zirconium propoxide,[6,7] which inhibits precipitation

of the sol. The Raman band at 843 cm^{-1} is only observed in materials processed with hydrogen peroxide, therefore peroxide is the source of this band. Finally, the very broad band centered at roughly 470 cm^{-1} is attributed to an amorphous zirconia structure, and will be discussed further in the following section. Note that n-propanol is not evident in any of these materials. Its presence might have been expected to show up in panel c of Fig. 5.2, and it is possible that the two extremely weak features near 1000 cm^{-1} in panel c may be due to n-propanol, but this is not clear. Thus the organic solvent does not seem to be present in significant quantity in any of these materials.

The prominent peroxide line present at 843 cm^{-1} in panels b and c of Fig. 5.2 is downshifted (by nearly 4%) from the HOOH line of Fig 5.1d, showing the influence of chemical bonding. Therefore, not only has the peroxide "wash" eliminated some of the trapped organic, it has also reacted chemically with the zirconium-propoxide/zirconia-sol. From the Raman scattering perspective, it has eliminated the troublesome luminescence background that both the zirconium-propoxide precursor and zirconia gels were plagued with. Samples treated with peroxide readily display the very broad amorphous band that is the subject of the next section.

5.5 Amorphous Zirconia

Scientific interest in amorphous zirconia derives in part from the fact that relatively little is known about the structure and properties of highly ionic amorphous solids. Unlike low-coordination covalently bonded network glasses such as SiO_2, which can be understood on the basis of Zachariasen-type continuous-random-network structures, there is no well-established model for the structure of high-coordination amorphous ionic oxides. (Models which are two-

sphere-size generalizations of the random-close-packing model used to describe simple amorphous metals might possibly be appropriate, but it is not clear how to incorporate the necessary chemical order into such models.)

Figure 5.3 is a comparison of the Raman spectrum of water [Fig. 5.3a] with an expanded version of the material of Fig. 5.2c (made by adding peroxide to zirconium propoxide). The band at 1650 cm^{-1}, as well as the broad band above 3000 cm^{-1}, are common to both spectra. This indicates the presence of water in this amorphous zirconia material, even though it is a powder. The sharp line at 843 cm^{-1} is the peroxide band, as discussed above. The band centered at 470 cm^{-1} is very broad (the full width at half maximum, FWHM, is 150 cm^{-1}), and this is characteristic of an amorphous material. There has been very little Raman work performed on amorphous forms of zirconia, perhaps due to luminescence problems. Keramidas and White[8] report a Raman spectrum of "amorphous ZrO_2" (made by precipitating $ZrOCl_2 \cdot 8H_2O$ with NH_3) which shows sharp lines of the tetragonal form superimposed on an ill-defined broad background that extends out to about 650 cm^{-1}. Fig. 5.3b may represent the first definitive observation of the Raman spectrum of amorphous zirconia, albeit a peroxide derivative.

5.6 Carbonate Phase Transitions Monitored by MgO:Cr^{+++} Luminescence

Magnesite, $MgCO_3$, and hydromagnesite, $4MgCO_3 \cdot Mg(OH)_2 \cdot 5H_2O$, are converted to magnesia, MgO, by heat treatment. I have monitored these thermally induced transformations by "Raman spectroscopy". Here "Raman spectroscopy" is in quotes because MgO, having the rocksalt structure, is not Raman active. This obstacle is overcome by taking advantage of a strong luminescent band in MgO, which is associated with a chromium impurity, Cr^{+++}, that is always present in

MgO.[9] A judicious choice of incident laser wavelength puts the strong luminescent band near a strong Raman feature of the starting material. The starting materials, magnesite and hydromagnesite, are carbonates, and their strong Raman features are CO_3^{--} symmetric-stretching modes that are located at 1095 and 1119 cm^{-1}, respectively. The luminescent band for MgO:Cr^{+++} is located at an absolute position of 14300 cm^{-1} (6993 Å wavelength); this position corresponds to a 1154 cm^{-1} "Raman shift" from the 15454 cm^{-1} (6471 Å) of the krypton laser.

Figure 5.4 shows spectra obtained for MgO powder using four different excitation wavelengths: 5145 Å of argon, and 5682 Å, 6471 Å, and 6764 Å of krypton. Although the numbers shown on the horizontal axis correspond to the wavenumber downshift for the particular case of the 6471 Å line (displaying the feature in question at an apparent shift of about 1150 cm^{-1}), all four spectra are plotted here against the actual scattered-light frequency ($\bar{\nu}_s$), so that the absolute frequency positions line up. The vertical line locates $\bar{\nu}_s$=14,300 cm^{-1} (λ_s=6993 Å), corresponding to a downshift relative to 6471 Å of about 1150 cm^{-1}. The results collected for MgO in this figure clearly reveal a series of luminescence bands, the most prominent being an unusually sharp band (unusually sharp for room-temperature luminescence) located near 14,300 cm^{-1}. (Luminescence bands do not shift with the position of the excitation frequency, i.e., "$\bar{\nu}_s$" is independent of $\bar{\nu}_L$, the behavior exhibited in Fig. 5.4).

Figure 5.5 presents results of monitoring the Raman scattering intensity of heat-treated magnesite, for thermal treatments from 200 to 600 C. Panel a shows only the CO_3^{--} symmetric-stretching mode of magnesite (1095 cm^{-1}). At 500 C (panel d), a new peak emerges which corresponds to the MgO:Cr^{+++}

luminescence band discussed above. This signals the conversion of magnesite to MgO. Complete conversion to MgO occurs somewhere between 500 and 600 C, for our two-hour heat-treatment time. (If the heat-treatment time was much longer than two hours, then complete conversion would occur below 500 C.) Figure 5.6 is a similar plot for hydromagnesite. Complete conversion occurs at a much lower temperature than for magnesite, somewhere between 300 and 400 C.

5.7 Summary

Two different systems were discussed, the zirconia system, and the magnesia system. Additives to the zirconia sol-gel system, acetic acid and hydrogen peroxide, chemically react with the zirconium. Raman spectra shows broad band structure, that is characteristic of amorphous materials, for the zirconia samples.

A technique for monitoring the conversion of magnesium carbonate to magnesia, as a function of heat treatment (temperature), is presented. This is done by monitoring the relative intensity of the Raman signature of the carbonate symmetric-stretch of magnesite, and the luminescent signature of the chromium impurity of magnesia.

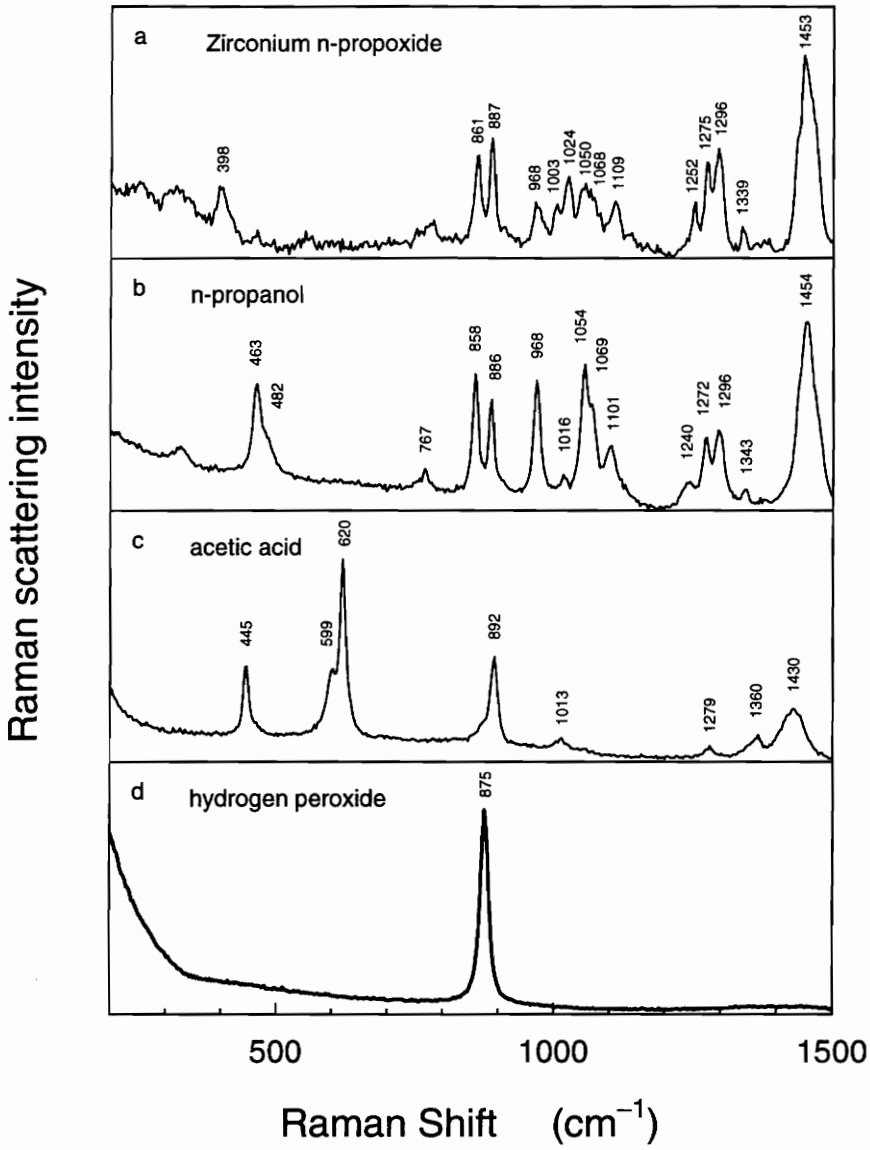

Fig. 5.1: Raman spectra of the precursors and additives of the zirconia sol-gel system. The krypton 647.1 nm laser line was the excitation source. Panel a is the Raman spectrum for zirconium n-propoxide with an approximate stoichiometry of $Zr(OC_3H_7)_4 \cdot 3C_3H_7OH$, as received from source manufacturer (a linear background was subtracted out). Panels b, c, and d, are Raman spectra for n-propanol, acetic acid, and hydrogen peroxide respectively.

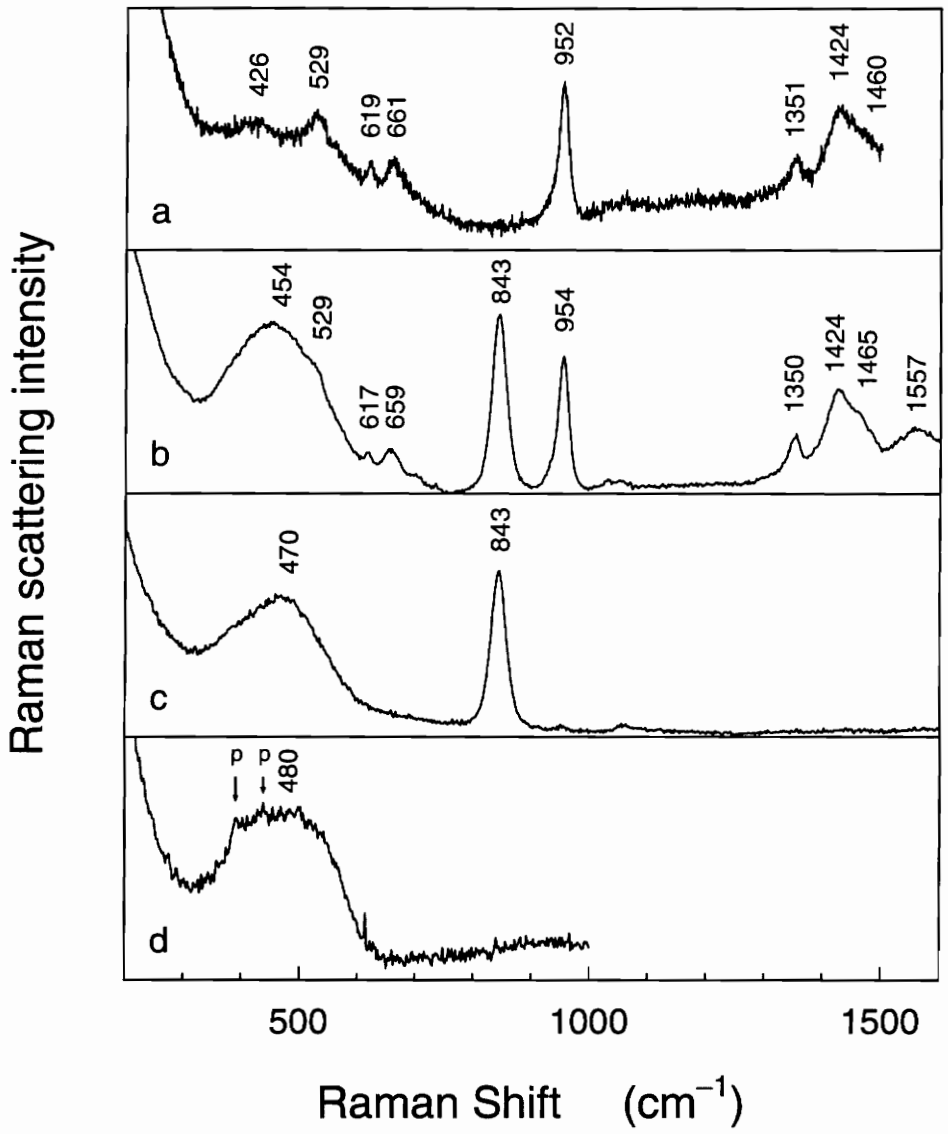

Fig. 5.2: Comparison of the Raman spectra for (a) a zirconia xerogel (obtained with argon 514.5 nm excitation), (b) a zirconia xerogel that was chemically treated with hydrogen peroxide to produce a white powder (obtained with argon 488.0 nm excitation), (c) hydrogen peroxide treated zirconium propoxide, which yielded a white powder, i.e., the sol-gel process was skipped (argon 514.5 nm excitation), and (d) hydrolyzed zirconium propoxide, a powder (krypton 647.1 nm excitation).

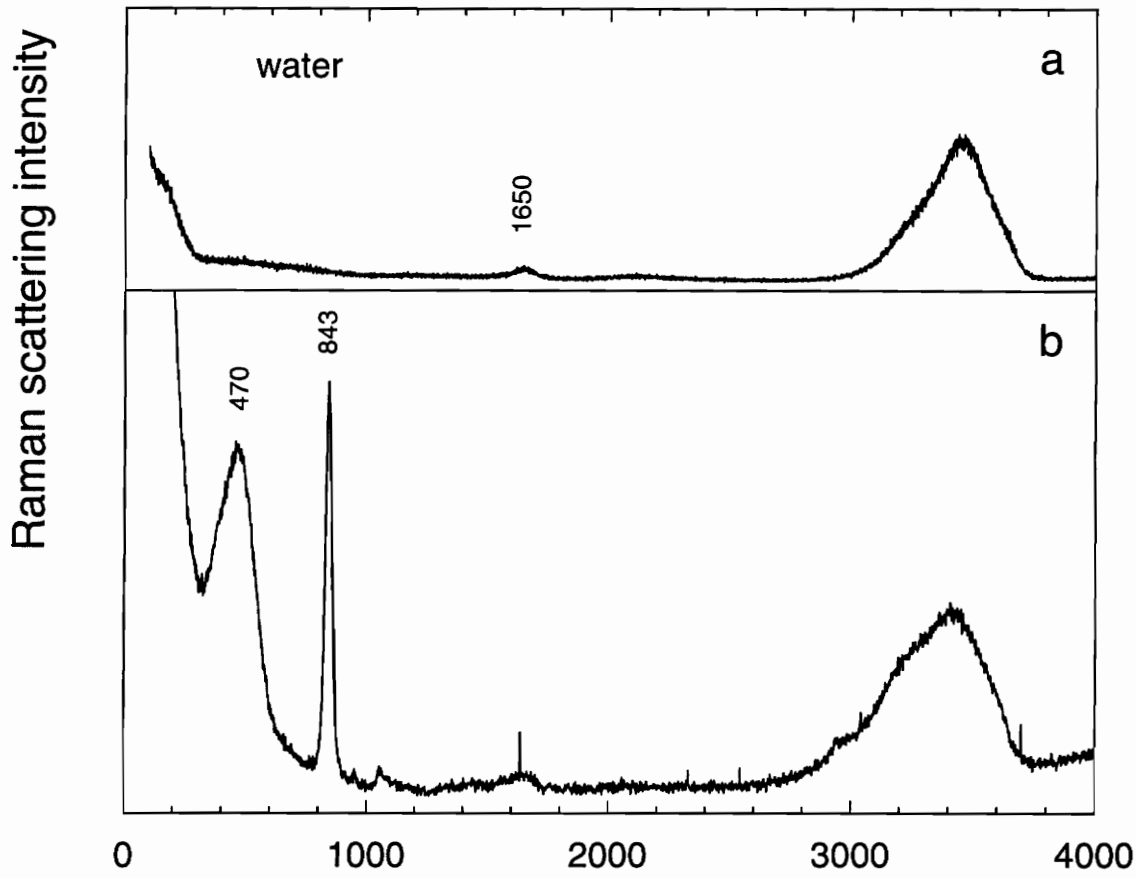

Fig. 5.3: Comparison of the Raman spectrum of (a) water and (b) hydrogen peroxide treated zirconium propoxide in the form of a white powder. Panel b is an expanded version of Fig. 5.2c.

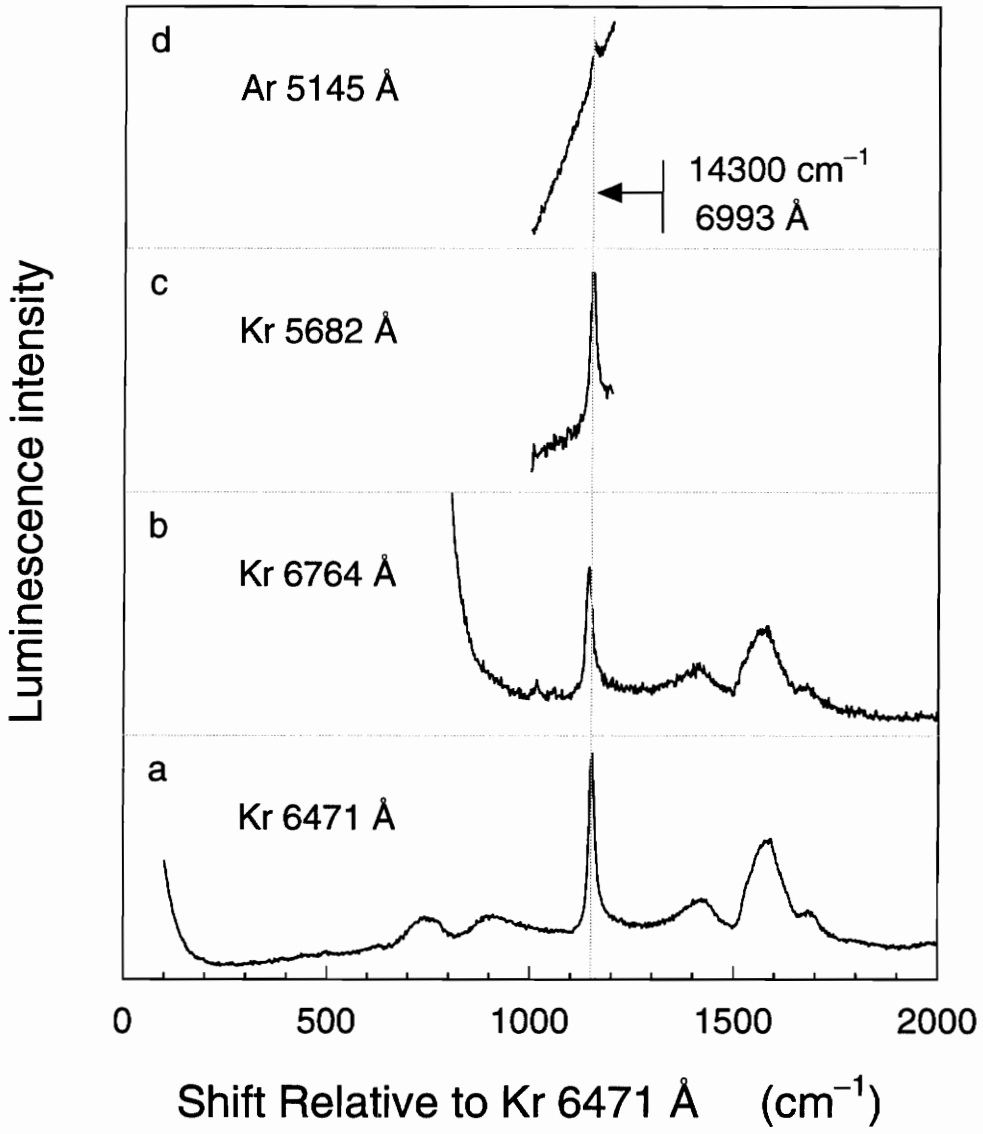

Fig. 5.4: Luminescence spectra of chromium doped magnesium carbonate, $MgCO_3:Cr^{+++}$, as a function of the incident laser wavelength.

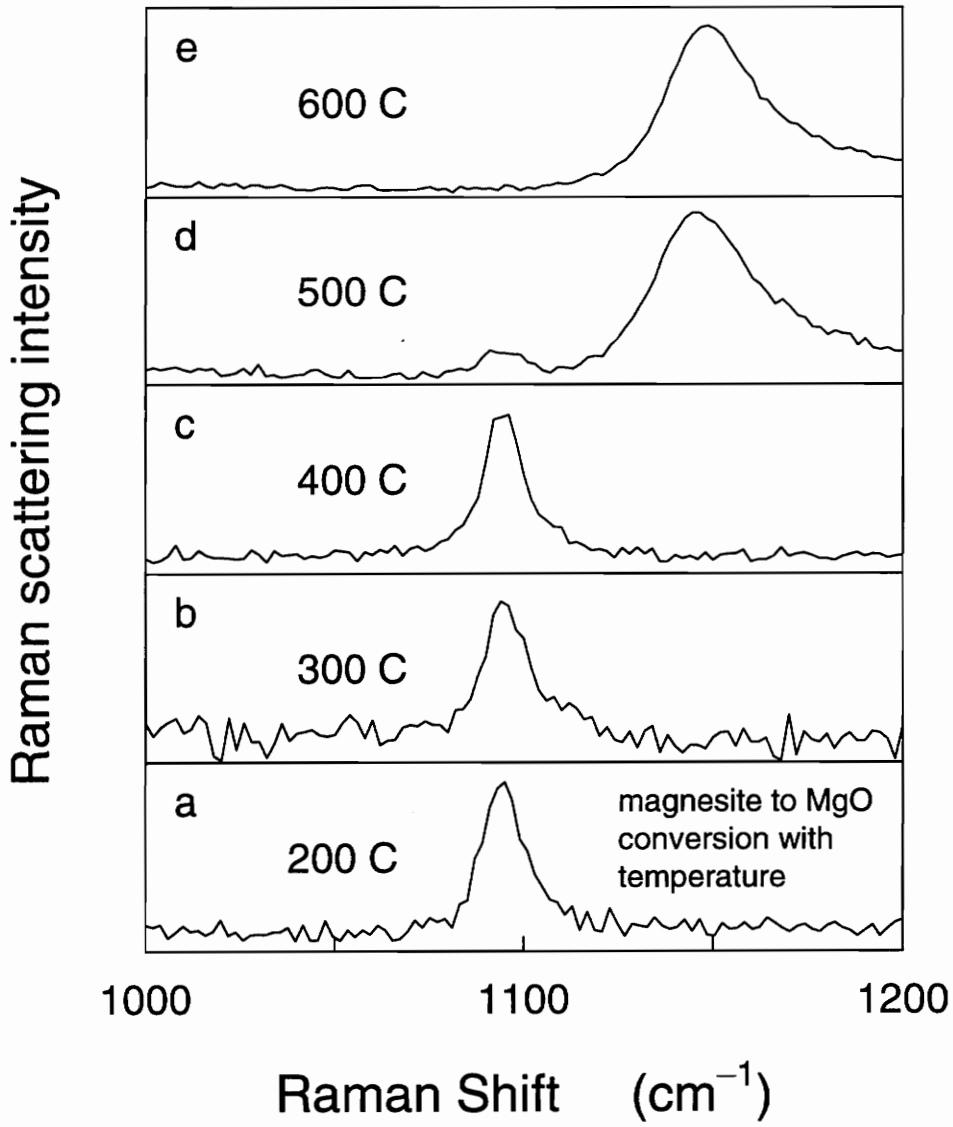

Fig. 5.5: Conversion of magnesite ($MgCO_3$) to magnesia (MgO) as a function of processing temperature.

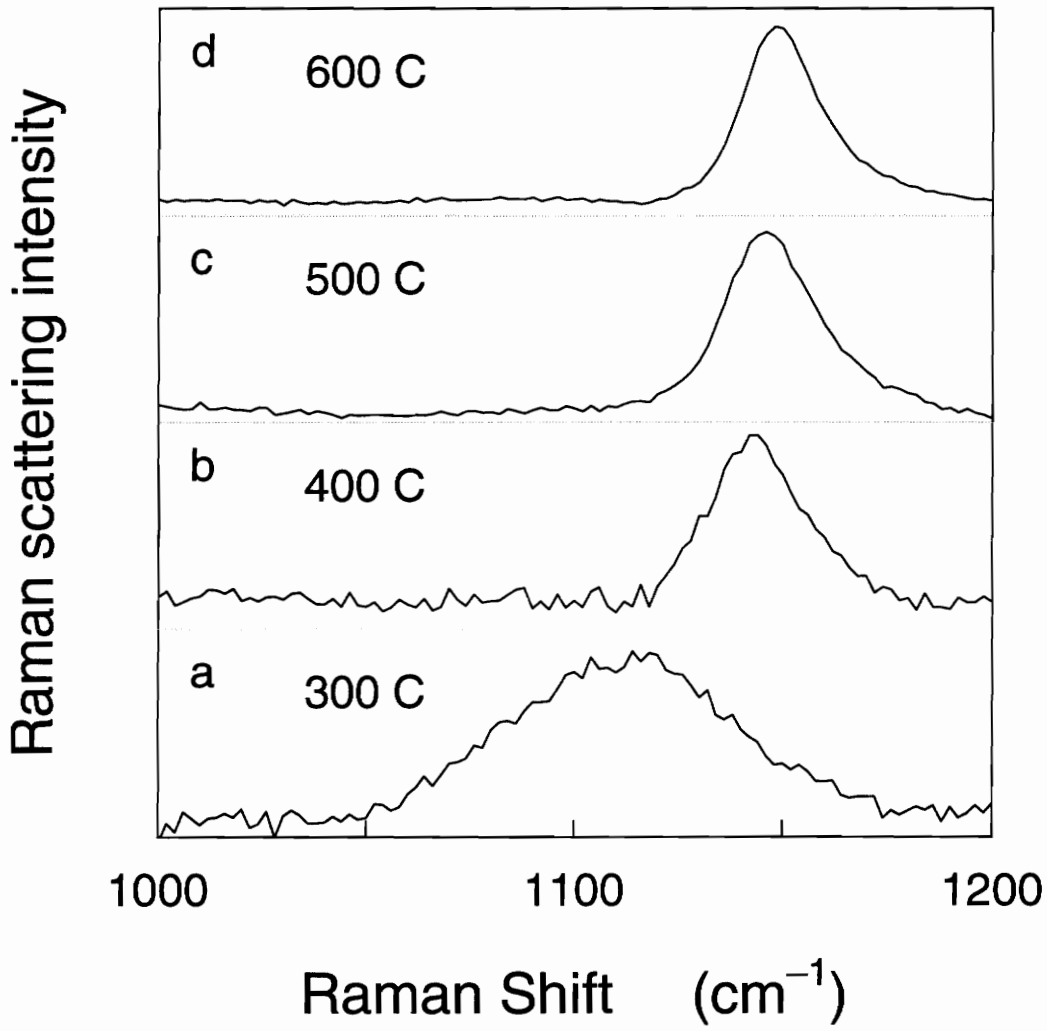

Fig. 5.6: Conversion of hydromagnesite to magnesia as a function of processing temperature.

---

[1]A. E. Geissberger and F. L. Galeener, Phys. Rev. B **28**, 3266 (1983).

[2]W. H. Zachariasen, J. Am. Chem. Soc. **54**, 3841 (1932).

[3]P. A. Budinger, J. R. Mooney, J. G. Grasselli, P. S. Fay, and A. T. Guttman, Anal. Chem. **53**, 884 (1981).

[4]J. C. Debsikdar, J. Non-Crystalline Solids **87**, 231 (1986).

[5]J. C. Debsikdar, J. Non-Crystalline Solids **87**, 343 (1986).

[6]C. J. Brinker and G. W. Scherer, Sol-Gel Science, (Academic Press, Boston, 1990), p. 52.

[7]A. Larbot, J. A. Alary, C. Guizard, L. Cot, and J. Gillot, J. Non Crystalline Solids **104**, (1988). Larbot et al. monitored the acetic acid/zirconium n-propoxide reaction by gas chromatography.

[8]V. G. Keramidas and W. B. White, J. American Ceramic Society **57**, 22 (1974).

[9]M. A. Hooper and D. W. James, Trans. Faraday Soc. **65**, 2016 (1969).

CHAPTER SIX

SUMMARY AND FUTURE DIRECTIONS

Four sol-gel systems were investigated, primarily by laser spectroscopy, on several series of materials prepared by systematically varying the synthesis procedures. In chapter 3, finite-size effects were observed in both the Raman and x-ray spectra of the sol-gel alumina system. These spectroscopic effects enabled the monitoring of oxyhydroxide AlO(OH) crystallite growth kinetics in the nanocrystal regime (particle-size diameters on the order of a few nanometers), as a function of time spent in the sol phase. Chapter 4 gave results on a closely related system, the trihydroxide $Al(OH)_3$ polymorph system. Here it is shown that crystal nucleation kinetics are responsible for the $Al(OH)_3$ phase mix. Hydroxide/oxyhydroxide phase-mix kinetics were also studied; this ratio increases with time. Two systems were discussed in Chapter 5. Raman spectra of the zirconia materials revealed a broad-band structure that was interpreted as the signature of an amorphous phase of zirconia. Raman and luminescent spectra (both obtained on the Raman spectrometer) were used to monitor the conversion of magnesium-carbonate-based materials to magnesium oxide, as a function of temperature. A more detailed summary, for each of these sol-gel systems, can be found at the end of the corresponding chapter cited above.

There are a couple of byproducts of this research which are worth noting. In previous work reported for AlO(OH), Raman lines were attributed to this crystal which I have shown to be impostors; they arise from nitric acid, which was used in the preparation of those particular samples. This finding was described in chapter three, section three, and it has now entered the literature as an aside in our Phys. Rev. paper on sol-gel alumina. Also, the results on AlO(OH) were of special

interest to Prof. Art Ruoff of Cornell, one of the key players in the high-pressure quest for metallic hydrogen. Prof. Ruoff had asserted that "metalliclike" optical absorption attributed (by his competitors) to solid hydrogen might have arisen from Al particles formed by the chemical reaction of H_2 with Al_2O_3 (sapphire is present, as the pressure gauge, in the high-pressure experiments). If such a reaction occurred, AlO(OH) would also be produced and its Raman lines would show up. Our definitive Raman results for AlO(OH) did not, in fact, support Prof. Ruoff's speculation. (On the other hand, the alleged evidence for hydrogen "metallization", reported by his competitors, has also turned out to be wrong.)

These complex and fascinating systems lend themselves to further study. In the sol-gel alumina system (chapter 3), nanocrystal-growth rate constants were found for systems that utilized an inorganic acid peptization step and a 95 C processing temperature. The use of an organic acid, such as acetic acid, and/or the addition of extraneous electrolytes, such as NaCl, may give information pertaining to the role of the anions in this system. Processing at higher temperatures, in a pressure vessel, would give the temperature dependence of the crystal growth rate constant. In other words, the kinetics of this nanocrystalline, high surface area material, warrants further study.

The sensitivity of the vibrational spectra (Raman, infrared) of boehmite and nanocrystalline boehmite to external stress, such as pressure, could give interesting results. Boehmite has a layered structure and structural phase transitions take place at around 200 C at ambient pressure. Pressure would selectively influence primarily the hydrogen-bonding interlayer interactions. It would be of interest to see what effect pressure has on the dominant Raman line that was exploited so heavily in the results of chapter three. Pressure might also reveal new phases

having different layer stackings. In addition, boehmite is a "low-temperature" crystal [as compared to, say, corundum (Al_2O_3)], which forms only very small crystals (usually less than about micron size). As such, it is rather unusual and scientifically interesting. A detailed dynamical calculation of its vibrational modes and frequencies could be a valuable contribution, especially with the availability now of the Raman results contained in chapter three of this dissertation.

The $Al(OH)_3$ polymorph system of chapter four is really a spin-off of the sol-gel system of chapter three. Two key processing parameters, acid peptization (which was eliminated) and processing temperature (which was lowered), were changed. The number of processing variables that can be changed in this system, as well as in all of the sol-gel systems, is very large. Results concerning the effect of acid peptization could be interesting, particularly as it relates to the relative $Al(OH)_3$ phase mix, which can be determined by analyzing the hydrogen-stretching region of the Raman spectrum.

The zirconia sol-gel system of chapter 5, as described in this dissertation, has not been extensively studied in the literature. The optically clear and dilute nature, for both the zirconia sol and gel, of the materials produced in this system, should lend itself to particle growth kinetic studies by small-angle x-ray scattering and perhaps by dynamical light scattering.

In general, modification of the processing parameters effects the kinetics of sol-gel systems. An understanding of the kinetics, and of the primary variables that control the kinetics, is not only a scientific contribution but is also essential for materials reproducibility and is therefore of technological value. Most of the materials synthesized in these systems are far too complicated to understand by study of one material alone. I have found that a systematic study, based upon a

well-designed variation of the process parameters, is an effective method of investigating these materials.

VITA

Calvin James Doss was born on September 24, 1958 in Des Moines, Iowa. He earned a Bachelor of Science degree in Mathematics in March 1984, a Masters of Science degree in Physics in December 1987, and a Ph.D. in Materials Physics in March 1994, from Virginia Tech.